INAUGURAL–DISSERTATION
zur
Erlangung der Doktorwürde
der
Naturwissenschaftlich–Mathematischen
Gesamtfakultät
der
Ruprecht–Karls–Universität
Heidelberg

vorgelegt von
M. Eng. Yong Hu
aus Sichuan, China

Tag der mündlichen Prüfung: 04.12.2015

Modeling and Simulation of Turbulent Non-Reacting and Reacting Spray Flows

Gutachter: Prof. Dr. Eva Gutheil
apl. Prof. Dr. Hans-Robert Volpp

Abstract

Due to the growing concern on the issues of global warming, climate change, and energy shortage, more rigorous requirements are imposed on the energy conversion process of combustion. Due to the relative safety and convenience in transportation and storage, liquid fuels are commonly used in many practical combustion systems such as diesel engines, gas turbines and industrial furnaces. In these combustion devices, turbulent spray flows are involved. The character of spray dispersion, evaporation, mixing and combustion of fuel droplets strongly determines the performance of these systems with respect to the combustion efficiency, stability, and emissions. Therefore, an improved understanding of turbulent spray combustion and the development of predictive models are needed for a better design of more efficient combustion systems.

The present work focuses on the development of a computational methodology based on the transported joint probability density function (PDF) method for the modeling and simulation of two-phase turbulent spray flows without and with chemical reactions. In the non-reacting situation, the dependent variables of the joint PDF include the gas velocity and the mixture fraction. For the simulation of reacting spray flows, a three-variate joint PDF transport equation is derived and modeled in order to account for the pre-vaporization effects and partially premixed regime in turbulent spray flames. The dependent variables include the gas phase mixture fraction, the reaction progress variable and gas enthalpy. Detailed combustion chemistry is considered through an extended spray flamelet model by including a reaction progress variable in addition to the classical formulation.

The dilute spray is simulated using a Lagrangian discrete parcel method for the description of droplet motion, heating and evaporation. The infinite conductivity model with consideration of non-equilibrium effects based on the Langmuir-Knudsen law is considered. The spray evolution and flame structures in the frame of the polydisperse reacting spray flows are investigated. Numerical results are compared with experimental data provided by Prof. Masri at the University of Sydney, Australia, and the test cases include three different turbulent non-reacting acetone spray flows in air and turbulent spray flames with the liquid fuel ethanol.

For the acetone spray flows, computational results generally show good agreement with experimental data in terms of the droplet size and mean velocity distribution, as well as the liquid volume flux. The results show that the inflow liquid mass loading hardly affects the droplet diameter distribution, whereas the inlet turbulence level has a pronounced effect. The tendency of droplet accumulation near the jet centerline is found with a somewhat overprediction of liquid volume flux at downstream locations. A more sophisticated turbulence model is expected to eliminate this discrepancy. More-

over, the local joint PDF of the gas velocity and the mixture fraction is analyzed. A linear correlation of the gas velocity and the mixture fraction exists close to the nozzle exit outside the main spray jet, and no regions are found where statistical independence prevails.

For the simulation of spray flames, computations with the newly developed spray flamelet/progress variable approach and with the previous standard spray flamelet formulation are carried out and compared with the experiments by Prof. Masri at the University of Sydney. A good agreement between the computations with the new formulation and the experiments for gas temperature and droplet size and velocity is achieved. The major spray and combustion properties are correctly captured using this new formulation, which is compared with an unphysically attached flame near the nozzle exit predicted by the previous model.

A partially premixed combustion prevails in this piloted turbulent spray flame. Due to the prevaporization of the ethanol droplets near the nozzle exit, a lean premixed gas mixture is found at the inner side of spray jet. Moving downstream, the lean-sided diffusion flame is promoted towards the inner fuel-rich side by heating up the inner premixed core that is controlled by the droplet evaporation. Additionally, it is observed that in the far-field region, the diffusion flame becomes the dominant combustion mode.

In summary, an efficient computational model based on the transported joint PDF method is developed to two-phase turbulent spray flows. The combined transported joint PDF and a newly proposed spray flamelet/progress variable approach shows an improved performance in the prediction of complex turbulent spray flames, and new insights on the local flame structure influenced by evaporating sprays are obtained.

Keywords: Dilute spray, Polydispersity, Spray combustion, Detailed chemistry, Turbulent flame, Transported joint PDF method, Spray flamelet, Reaction progress variable

Zusammenfassung

Aufgrund der wachsenden Besorgnis über die globale Erwärmung, den Klimawandel und die Energieknappheit werden ständig strengere Anforderungen an den Energieumwandlungsprozess durch Verbrennung gestellt. Aufgrund der relativ sicheren und einfachen Transport- und Lagerungsmöglichkeiten werden flüssige Brennstoffe in Verbrennungssystemen wie Dieselmotoren, Gasturbinen und Industrieöfen eingesetzt. Die Verbrennung erfolgt typischerweise unter turbulenten Bedingungen. Die Leistung dieser Systeme im Hinblick auf Verbrennungseffizienz, Stabilität und Emissionen wird stark durch den Charakter der Dispersion, Verdampfung, Vermischung und Verbrennung des Kraftstoffsprays bestimmt. Daher werden ein besseres Verständnis der turbulenten Sprayverbrennung und die Entwicklung von Modellen für ein bessere effizientere Verbrennungssysteme benötigt.

In der vorliegenden Arbeit wird eine Berechnungsmethode entwickelt, die auf der transportierten multivariaten Wahrscheinlichkeitsdichtefunktion (probability density function - PDF) zur Modellierung und Simulation von turbulenten Sprayströmungen ohne und mit chemischen Reaktionen basiert. Im nichtreagierenden Fall umfassen die abhängigen Variablen der multivariaten PDF die Gasgeschwindigkeit und den Mischungsbruch. Für die Simulation von turbulenten reagierenden Sprayströmungen wird eine dreiparametrige PDF-Transportgleichung hergeleitet und modelliert, um die teilweise vorgemischten Bereiche in turbulenten Sprayflammen zu berücksichtigen. Die abhängigen Variablen beinhalten den Mischungsbruch in der Gasphase, die Reaktionsfortschrittsvariable und die Enthalpie der Gasphase. Detaillierte Verbrennungschemie wird mithilfe eines erweiterten Sprayflammenmodells berücksichtigt, indem eine neue Reaktionsfortschrittsvariable neben der klassischen Formulierung integriert wird.

Die Bewegung, Erhitzung und Verdampfung der Tröpfchen des dünnen Sprays werden in Lagrangescher Betrachtungsweise beschrieben. Die Annahme schneller Wärmeleitung innerhalb des Tröpfchens wird unter Berücksichtigung von Nichtgleichgewichtseffekten basierend auf dem Langmuir-Knudsen-Gesetz berücksichtigt. Die Simulationsergebnisse werden mit Versuchsergebnissen von Prof. Masri, Universität Sydney, Australien, verglichen. Die Testfälle beinhalten drei verschiedene turbulente, nichtreagierende Strömungen von Acetonsprays sowie turbulente Sprayflammen aus dem flüssigen Kraftstoff Ethanol.

Für die Acetonsprays zeigen die Simulationsergebnisse generell eine gute Übereinstimmung mit den Versuchsergebnissen in Bezug auf die Tröpfchengröße, die mittlere Geschwindigkeitsverteilung sowie den Flüssigkeitsvolumenfluss. Die Ergebnisse zeigen, dass die flüssige Massenbeladung kaum Einfluss auf die Verteilung des Tröpfchendurchmessers hat, während die Turbulenzintensität einen starken Effekt hat. In der Mitte

des Spraystrahls findet sich eine Akkumulation der Tröpfchen, und der Volumenstrom fernab der Einspritzung ist etwas überbestimmt. Es wird erwartet, dass ein anspruchsvolleres Turbulenzmodell diese Diskrepanz beseitigt. Darüberhinaus wird die lokale, gebundene PDF der Gasgeschwindigkeit und des Mischungsbruchs analysiert. Eine lineare Korrelation der Gasgeschwindigkeit und des Mischungsbruchs existiert in der Nähe des Düsenaustritts außerhalb des Hauptspraystrahls. Es wurden keine Bereiche gefunden, in denen statistische Unabhängigkeit vorliegt.

Für die Simulation der Sprayflammen werden Berechnungen mit dem neu entwickelten Ansatz einer Reaktionsfortschrittsvariable für Sprayflammen sowie mit dem Standardmodell durchgeführt und mit den Versuchsergebnissen von Prof. Masri, Universität Sydney, verglichen. Eine gute Übereinstimmung zwischen den Berechnungen mit dem neuen Modell und den Experimenten für die Gastemperatur, Tropfengröße und -geschwindigkeit wurde erreicht. Die Haupteigenschaften des Sprays und der Verbrennung werden korrekt durch die neue Formulierung wiedergegeben.

In dieser pilotierten turbulenten Sprayflamme liegt eine teilweise vorgemischte Verbrennung vor. Aufgrund der Verdampfung der Ethanoltröpfchen durch die Pilotflamme nahe des Düsenausgangs liegt ein mageres Gasgemisch auf der Innenseite des Spraystrahls vor. Stromabwärts wird die magere Diffusionsflamme in Richtung der inneren, kraftstoffreichen Seite durch Aufheizen des inneren Kerns gelenkt, welcher von der Tröpfchenverdampfung dominiert wird. In Regionen fern der Düse liegt eine reine Diffusionsflamme vor.

Zusammenfassend wurde ein effizientes Berechnungsmodell auf Basis der transportierten multivariaten PDF Methode für turbulente Sprayströmungen entwickelt. Die transportierte multivariate PDF kombiniert mit einer neu vorgeschlagenen Reaktionsfortschrittsvariablen für Sprayflammen zeigt eine Verbesserung bei der Vorhersage komplexer turbulenter Sprayflammen, und es können neue Erkenntnisse über die lokale Flammenstruktur, welche durch verdampfende Sprays beeinflusst wird, erhalten werden.

Schlagworte: Dünnes Spray, Polydispersität, Sprayverbrennung, Detaillierte Chemie, Turbulente Flammen, Transportierte PDF Methode, Spray flamelet, Reaktionsfortschrittsvariable

Contents

List of Figures

List of Tables

1. Introduction

Combustion is a commonly used process for power generation, and it is widely found in many energy systems. With the growth of new economies, the demand for energy, supporting the daily life of human societies, is rising rapidly, and it is met by using the conventional processes of combustion or the new energy sources such as nuclear power, wind and solar, etc. [1]. Even though the new energy sources have gained significant development in recent years with the continuing technological evolution of their applications, combustion, which is mainly fueled with the traditional fossil fuels such as coal, natural gas and petroleum (see Fig. 1.1), remains the main source, meeting the world's energy needs [1].

Essentially, combustion is a high-temperature chemical process in which the fuel reacts rapidly with oxygen, releasing heat. Usually, the fuel can be in solid, liquid or gaseous form, and among them, due to the relative safety and convenience in transportation and storage, liquid fuels consitute the primary source [2]. As shown in Fig. 1.2, the liquid fuels contributed 34% of the world total energy consumption in 2010. Although this number will slightly decrease in the next four decades, liquid fuels still dominate the global energy consumption [3].

The growing global energy demand also puts a pressing requirement to increase energy supply from other sources. Biofuels are the energy sources that have received increasingly attention and undergone a fast development in the last few decades [4].

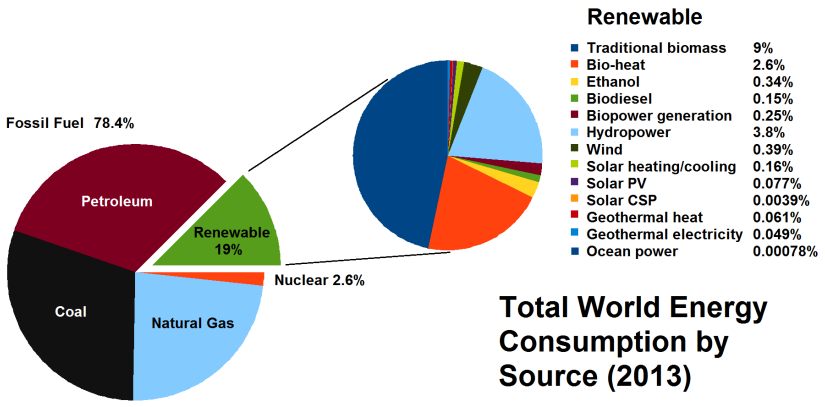

Figure 1.1: Total world energy consumption by source 2013 [1].

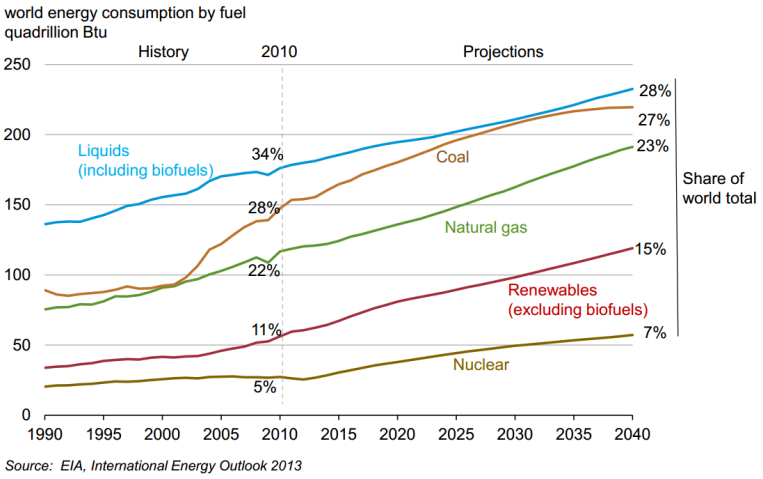

Figure 1.2: World energy consumption outlook by fuel [3].

They are viewed as an attractive and sustainable alternative to fossil fuels. According to the report of the International Energy Agency (IEA) [5], biofuels are expected to meet more than a quarter of world demand for transport fuels by 2050. Different from the fossil fuels that are mainly produced through the geological processes working on the remains of the decomposition of plants and animals, biofuels are obtained from organic materials through contemporary biological processes [5–7]. Thus, biofuels offer advantages: they are renewable and sustainable, and they burn more environmentally-friendly than the traditional fossil fuels [4, 7]. Generally, there are two main types of biofuels [5, 8, 9]. One is ethanol, which is an alcohol made by fermentation and distillation from sucrose-producing plants such as sugarcane, sugarbeet or cereals. Also, new feedstock for ethanol production is being developed such as the cellulosic biomass. Another important biofuel is biodiesel, which is produced from vegetable oils and animal fats using a chemical process of trans-esterification. As indicated in Renewables Global Status Report for 2015 [10], in the foreseeable future, ethanol production will continue to grow as the most important source for biofuel supply.

The combustion process makes use of exothermic reactions to convert the chemical energy of the fuel to thermal energy of the products, which is eventually utilized in a variety of power applications, whereas some undesired pollutant emissions, such as NO_x, CO_2, and soot, are normally produced [11–14]. In recent years, the issues of global warming, climate change, and energy shortage are increasingly gained concern worldwide [4, 7]. On the one hand, this leads to exploring new forms of renewable and clean energy sources, or development of fuel additives to increase fuel efficiency such as the acetone, which is believed to aid in the vaporization of the gasoline or diesel [15]. On the other hand, more demanding requirements of clean and efficient

means of converting the combustion energy are imposed on the combustion systems. This need, therefore, motivates researchers to get a thorough understanding of the underlying physical mechanisms of combustion processes and improve the design approaches. Development of more sophisticated models and predictive computational tools would represent a significant step to promote the ability of more efficient and robust design, and optimization of energy systems [11, 13, 14, 16, 17].

Liquid-fueled combustion basically involves a turbulent evaporating spray flow. In most technical applications, the liquid fuel, typically carried by a turbulent gas flow, is first injected and atomized into droplets featuring a wide range of size and velocity distributions, and they penetrate into the ambient gaseous environment in which oxidizer (commonly air) or a mixture of hot combustion gas and air is observed. This type of two-phase flow is often characterized by the complex interactions between different underlying physico-chemical processes, making it one of the most challenging areas in science and engineering [18]. When chemical reactions are involved in these spray flows, another level of complexity is added, and more general fields of spray dynamics, mass and heat transport, aerothermodynamics and chemical kinetics should be concerned.

The important and well-known combustion devices in practise, that involve disperse liquid-fuel sprays, include, for instance, internal combustion engines and gas turbines that are used in liquid-fuel powered vehicles or aircraft, as well as industrial furnaces. Gas turbines [12] represent one of the most widely used power generation technologies, which can fulfill different high requirements from a wide spectrum of applications. As indicated by their name, gas turbines work mainly based on the compressed hot gases, and the energy is added by turbulent combustion of spray fuel occurring in the combustion chamber. As a high efficient and flexible power supplier, gas turbines-based systems are expected to continuously play an important role in the near future. Reciprocating diesel engines [13], as one type of internal combustion engines, are a well-known technology extensively used in transportation systems, like automobiles, trucks or marine propulsion, where, however, the combustion occurs intermittently and expanding combustion exhaust gases push a piston, instead of the blades used in gas turbines, to output mechanical energy.

In the spray-combustion applications mentioned above, the presence of evaporating droplets increases the complexities compared with those found in pure gas combustion, and the behavior of sprays plays a major role in determining the combustion performance and the energy-conversion efficiency [19, 20]. In general, with an initial momentum, liquid fuel is injected firstly into the combustion chamber in the form of a turbulent spray. Then the disperse fuel-droplets undergo a sequence of processes, i.e., droplet breakup, collision and coalescence, evaporation and turbulent dispersion, as well as chemical reactions between fuel vapor and air [20]. These various physical and

chemical processes involved here can interact with each other in different ways. In addition, the spray atomization and breakup could result in a broad range of droplet size distribution and the polydispersity of sprays. The polydispersed droplets influence gas turbulence due to momentum exchange and the vapor fuel added with the evaporation processes, which are decisive for the combustion properties. Vice versa, the heat release and local scalar change, due to combustion, will in turn influence the mass and heat transfer between phases and the rate of droplet evaporation. Thermal expansion can also affect the turbulent dispersion of droplets. Additionally, depending on the local droplet distribution, the mixing phenomena, and the combution chamber and spray geometries [19, 21–24], mixed combustion regimes can be observed, where evaporation-dominated, premixed, nonpremixed or partially premixed combustion may coexit and interact, which poses a tremendous challenge for the mathematical modeling.

Given these important applications of spray combustion and its complexities with multiphase couplings and multi-combustion regime involved, the development and verification of high-fidelity computational models that fit to the description of complex turbulent two-phase reacting flows become necessary. The focus of this work is to establish a computational methodology based on a transported probability density function (PDF) modeling approach for the simulation of turbulent evaporating sprays without and with chemical reactions. Transported PDF method has been developed for several decades, and it has shown the powerful capability for the modeling of various complex turbulent flows [22, 25, 26]. With the transported PDF method, the stochastic nature of turbulence is fully taken into account by solving the transport equation of the joint PDF of the considered fluid variables such as velocity, composition, and enthalpy. Thus, compared with the conventional methods, transported PDF method provides much more information, and the turbulence fluctuations of considered variables are completely represented. Due to this complete description, the important processes, including the convective transport, body force, mean pressure gradient and chemical reaction source terms, can be treated in an exact way [25]. For the turbulent spray flows, the spray source terms appear in closed forms and can be incorporated into the gas phase calculation at the particle level [27]. Therefore, transported PDF method shows as a promising way for the efficient modeling and simulation of nonreacting and reacting turbulent spray flows.

Specifically, in this thesis, for the nonreacting situation, the transport equation for the one-point one-time Eulerian joint PDF of the gas velocity and mixture fraction is solved with consideration of additional terms accounting for the interaction of the gas and the spray evaporation. For the simulation of reacting spray flows, a three-variate joint PDF transport equation is derived and modeled for the description of the pre-vaporization effects and partially premixed regime in turbulent spray flames.

The dependent variables include the gas phase mixture fraction, the reaction progress variable and enthalpy. Moreover, detailed combustion chemistry is considered with a spray flamelet model extended by use of the chemical reaction progress variable. For the model validation, numerical results are discussed and analyzed in comparison with experiments conducted by A. Masri and co-workers at the University of Sydney, Australia [28].

In the following chapter, the numerical simulations of turbulent two-phase flows and available turbulent combustion models that have been developed for spray flame are reviewed, and in chapter 3, the governing equations together with the physical models for both gas and liquid phase are introduced. The transported PDF equation is derived and formulated for both turbulent non-reacting and reacting spray flows. A new spray flamelet formulation is proposed and described. Chapter 4 gives a description of the numerical scheme applied in the present work. In chapter 5, the experimental setup described by Gounder et al. [28] and numerical results are discussed. The test cases include three different turbulent polydisperse acetone spray flows and a turbulent piloted ethanol spray flame. Finally, a summary and outlook are given in chapter 6.

2. State of the Art

2.1 Modeling of Turbulent Spray Flows

The numerical modeling of turbulent spray flows has been developed for decades and has received growing attention, with the progress of computer technology. A comprehensive description of the basic governing equations, relevant computational methods, and modeling assumptions used in spray flows was given in recent reviews [22, 29]. In turbulent spray flows, constructing high-fidelity numerical models for both the carrier gas phase and the disperse liquid phase is crucial to have an accurate representation of spray characteristics.

Numerical simulation is a powerful technical tool to provide insight into the phenomena of interest, based on the numerical interpretation of the corresponding basic governing equations. The dynamics of continuous gas phase are taken into account by a set of governing equations, and several different strategies for solving these equations are used in current Computational Fluid Dynamics (CFD) computations [30], which include direct numerical simulations (DNS), large eddy simulations (LES), and Reynolds-averaged Navier-Stokes (RANS) equation models.

In DNS simulations, all relevant time and length scales in the flow-field are resolved directly, and thus, the Navier-Stokes equations are solved with no need of any modeling. This leads to a rigorous requirement of the computational grid size, and, even for a flow of moderate Reynolds number, an enormous amount of grid points are needed in 3D DNS, in a quantity proportional to $\mathrm{Re}^{9/4}$ [30]. This expensive computational cost in DNS makes its use infeasible in the computation of practical systems for the current computer resources, while DNS result represents a single realization of a short-duration flow and contains very detailed informations on the flow field, thus it is useful in fundamental physics understanding and model development for turbulence or spray processes [30]. DNS of spray flows has been reported in some studies [23, 31–35], but due to high computational cost, more often, the model assumptions for simplying the description of disperse phase are used.

Compared with DNS, LES uses the filtering operation to solve the governing equations, where only the dynamics of large turbulent structures is explicitly resolved, and processes, occurring in the scales smaller than the cut-off filter width, are modeled. In

this way, the computational cost is reduced, while the subgrid-scale (SGS) models are still needed to capture the effects of sub-filter small-scale structures, and the sub-grid fluctuations can be interpreted as conditional statistics with respect to the resolved large scales. In LES of spray flows, the SGS models for detailed description of subgrid droplet dispersion, evaporation and SGS correlations between different processes or phases are important for accurate simulations of spray combustion [29, 36, 37]. Some detailed review studies on LES are given in Refs. [36, 38, 39]

In Reynolds-averaged Navier-Stokes (RANS) computation, the Reynolds-Averaged governing equations for the turbulent mean-flow properties and corrections are solved, and the unclosed terms, the Reynolds stress and turbulent scalar fluxes in the equations, are modeled [40]. Compared with LES, RANS gives values averaged over the whole turbulence spectrum, and thus the modeling requirements of accounting for unresolved flow characteristics are higher. Due to its low computational cost and flexibility for wide applications in many complex practical combustion systems, RANS remains to be the main method in CFD of engineering applications. In the present work, RANS based modeling approach is used. The corresponding formulation of basic conservation equations and models in two-phase spray flows would be described in the next chapter.

The above described computational approaches for the continuous gas phase are normally performed in the Eulerian framework; the governing equations are discretized on the grid nodes, where the flow characteristics (density, velocity, energy, and species) are resolved. In two-phase spray flows, however for the disperse liquid phase, there are usually two main solution strategies: the Eulerian method [41, 42], in which, based on a random field description, the dispersed liquid phase is also treated as continuum and spray characteristics are declared at the same grid nodes of the gas phase; the Lagrangian method [43, 44], where the spray is characterized by a large number of computational droplets, and then the Lagrangian particle tracking approach is used to obtain statistical properties of the liquid phase. Therefore, the modeling approach available for the whole two-phase spray flow systems, including both disperse liquid phase and carrier gas phase, can be classified into two categories: Eulerian-Lagrangian (EL) method and Eulerian-Eulerian (EE) method.

Generally, EL approach shows some significant advantages over the EE method. the EL approach can accurately represent the complex spray dynamics with low computational cost compared with EE method, where additional closure problems arise when Eulerian average is applied to the disperse phase and represent a big modeling challenge [45, 46]. Studies [47] show that the Lagrangian approach reveals more flame structures under the evaporation effects, when considering the spray as locally mono-disperse. Fox [36] pointed out that, compared with the macroscopic model of EE method, EL represents a mesoscopic model, and contains more information of

spray flows and less closure problems, although in EL method some modeling issues related to particle tracking, control of statistical errors and data exchange between two reference frames, are still involved. The focus of present work will be the Eulerian-Lagrangian (EL) modeling approach, and the detailed description of the Lagrangian spray evolution will be given in the next chapter.

In chemically reacting two-phase spray flows, chemical reaction introduces additional scales, and their coupling with the evaporating droplets leads to significant complexities, especially the fluid flow is usually turbulent. For the simulation of the reacting turbulent spray flows, an adequate numerical approach has to be provided for the closure of the mean chemical reaction rate under the influence of interactions with turbulence and sprays. Many models, previously developed for the gas flames, have also been applied in spray flames. In the following section, the turbulent combustion models that have been extended for spray combustion are presented, and more detailed descriptions of turbulent combustion modeling can be found in other work [40, 46, 48, 49].

2.2 Turbulent Spray Combustion Models

In this section, a review of the turbulent combustion models that have been studied for the description of two-phase spray combustion is given.

2.2.1 Bray-Moss-Libby Model

The Bray-Moss-Libby (BML) model was first proposed in 1977 [50] for the modeling of turbulent premixed combustion, and it has been further improved in many studies [51–53]. Basically, this model can be viewed as an application of the classical flamelet concept in turbulent premixed combustion [54], where instead of the mixture fraction, a reaction progress variable, c is used for the characterization of flame structures, and is defined in this model as a normalized temperature [54]

$$c = \frac{T - T_{\mathrm{u}}}{T_{\mathrm{b}} - T_{\mathrm{u}}}, \tag{2.1}$$

with the reference temperatures, T_{u} and T_{b} for the unburnt and burnt mixtures. Based on a phenomenological analysis of premixed flame structures, the PDF $P(c; \mathbf{x}, t)$ of progress variable c in a turbulent flow is determined as a sum of the probability of finding the unburnt, burnt and burning gas mixtures, which are respectively denoted as the first, second and third terms on the right hand side of Eq. (2.2) as [40]

$$P(c; \mathbf{x}, t) = \alpha(\mathbf{x}, t)\delta(c) + \beta(\mathbf{x}, t)\delta(1 - c) + \gamma(\mathbf{x}, t) f(c; \mathbf{x}, t), \tag{2.2}$$

where $\alpha(\mathbf{x},t)$, $\beta(\mathbf{x},t)$, and $\gamma(\mathbf{x},t)$ represent the probability of having unburnt, burnt and burning gas mixtures at location $(\mathbf{x},t)$, respectively. $\delta(c)$ and $\delta(1-c)$ are two Dirac-delta functions associated with the probability for the unburnt ($c=0$) and the burnt ($c=1$) gas, respectively. $f(c;\mathbf{x},t)$ is the distribution of c located in the reaction zone ($0<c<1$). Under the assumption that the reaction zone is infinitely thin [54], corresponding to $\gamma \ll 1$, the bimodal PDF of c is obtained and Eq. (2.2) is reduced to [40]

$$P(c;\mathbf{x},t) = \alpha(\mathbf{x},t)\delta(c) + \beta(\mathbf{x},t)\delta(1-c), \tag{2.3}$$

which indicates that c is introduced with only two possible value, i.e. 1 for burnt and 0 for unburnt gas. In the simulations of turbulent premixed combustion, using density-weighted averaging, the transport equation of the mean reaction progress variable is solved as [48, 54]

$$\frac{\partial(\langle\rho\rangle\widetilde{c})}{\partial t} + \frac{\partial(\langle\rho\rangle\widetilde{U}_i\widetilde{c})}{\partial x_i} = -\frac{\partial}{\partial x_i}\Big(\langle\rho\rangle\widetilde{u_i''c''}\Big) + \langle\dot{\omega}_c\rangle. \tag{2.4}$$

In this equation, $\langle\rho\rangle$ is the mean gas density, $\widetilde{U}_i$ the mean gas velocity and $\tilde{\dot{\omega}}_c$ the mean specific reaction rate of c, which, under the BML modeling, can be closed with the following expression [55, 56]

$$\langle\dot{\omega}_c\rangle = \rho_u S_L^0 I_0 g_0 \frac{\widetilde{c}(1-\widetilde{c})}{\hat{L}}, \tag{2.5}$$

where ρ_u is the density of the unburnt mixture. S_L^0 denotes the laminar burning velocity of the unstretched flame and I_0 is the stretch factor. g_0 is a coefficient and $\hat{L}$ is the flame wrinkling length scale. There are also other different closure approaches based on for example the flame surface density for the mean chemical reaction rate, which can be referred to Ref. [49].

The BML model was initially developed for the gas premixed flame calculations, and it was used by Chrigui [57, 58] in the simulation of turbulent spray flames, where the formulation of BML model described above for gaseous flame is adopted. However, when the interactions between reaction zone and evaporating sprays are concerned, the use of turbulent burning velocity including two-phase coupling effects would be necessary [22].

2.2.2 Conditional Moment Closure

The conditional moment closure (CMC) was first developed by Klimenko [59] and Bilger [60]. The basic idea behind this method is that, if the fluctuations of gas composition are mainly determined by the fluctuation of one common variable, the

conditional moment can be used to evaluate the mean chemical reaction rate; the terms involving fluctuations can be neglected and this is also called first-order CMC. The instantaneous species mass fraction Y_α is defined by [59]

$$Y_\alpha(\mathbf{x},t) = Q_\alpha(\xi,\mathbf{x},t) + Y''_\alpha(\mathbf{x},t), \tag{2.6}$$

Y''_α is the conditional fluctuation of species mass fraction which satisfies $\langle Y''_\alpha|\zeta\rangle = 0$ [59]. After averaging the obove equation (2.6) conditioned on $\xi = \zeta$, the conditional moment of the species mass fraction is then given as [59]

$$Q_\alpha(\zeta,\mathbf{x},t) = \langle Y_\alpha(\mathbf{x},t)|\zeta\rangle = \langle Q_\alpha(\xi,\mathbf{x},t)|\zeta\rangle. \tag{2.7}$$

where ξ is the mixture fraction, and ζ is the corresponding variable in sample space. Inserting the equation (2.6) into the instantaneous governing equation of the species mass fraction, and applying the conditional averaging to the resulting equation, the transport equation of the conditional mean Q_α is obtained [59]

$$\begin{aligned}\langle\rho|\zeta\rangle\frac{\partial Q_\alpha}{\partial t} + \langle\rho|\zeta\rangle\langle U_i|\zeta\rangle\frac{\partial Q_\alpha}{\partial x_i} &= \langle\rho|\zeta\rangle\langle\chi|\zeta\rangle\frac{\partial^2 Q_\alpha}{\partial\zeta^2} \\ &+ \langle\rho|\zeta\rangle\langle\dot\omega_\alpha|\zeta\rangle + e_Q + e_{Y''},\end{aligned} \tag{2.8}$$

with

$$e_Q = \Big\langle \mathrm{div}(\rho D\nabla Q_\alpha) + \rho D\nabla\xi\cdot\nabla\frac{\partial Q_\alpha}{\partial\zeta}|\xi=\zeta\Big\rangle \tag{2.9}$$

$$e_{Y''} = -\Big\langle \rho\frac{\partial Y''_\alpha}{\partial t} + \rho D\cdot Y''_\alpha - \mathrm{div}(\rho D\nabla Y''_\alpha)|\xi=\zeta\Big\rangle. \tag{2.10}$$

Here, e_Q represents the effects of molecular diffusion, and $e_{Y''}$ denotes the transport by the conditional fluctuations. In the high Reynolds number limit, the term e_Q can be neglected [59], and the term $e_{Y''}$ is usually modeled with the relation [59]

$$e_{Y''}P(\zeta) = -\frac{\partial}{\partial x_i}\big(\rho\langle u_i''Y''_\alpha|\zeta\rangle P(\zeta)\big), \tag{2.11}$$

where $P(\zeta)$ is the probability density function of ζ.

In equation (2.8), U_i is the gas velocity, and χ is the scalar dissipation rate of the mixture fraction. $\dot\omega_\alpha$ is the source term of chemical species due to chemical reactions. Solving Eq. (2.8) still needs the closure of the conditional mean velocity $\langle U_i|\zeta\rangle$ and scalar dissipation rate $\langle\chi|\zeta\rangle$. Various modeling approaches for these two terms can be found in Refs. [25, 61–65]. For the CMC simulation of spray combustion, the extended formulation, considering the interactions of the gas and spray evaporation, is proposed

by Mortensen and Bilger as [66]

$$\begin{aligned}\frac{\partial Q_\alpha}{\partial t}+\langle U_i|\zeta\rangle\frac{\partial Q_\alpha}{\partial x_i} &= -\frac{1}{\bar\rho\widetilde{P}(\zeta)}\frac{\partial(\bar\rho\widetilde{P}(\zeta)\langle u_i''Y_\alpha''|\zeta\rangle)}{\partial x_i}+\langle\chi|\zeta\rangle\frac{\partial^2 Q_\alpha}{\partial\zeta^2}\\ &+ \langle\dot\omega_\alpha|\zeta\rangle+\left[\delta_{l\alpha}-Q_\alpha-(1-\zeta)\frac{\partial Q_\alpha}{\partial\zeta}\right]\langle\Pi|\zeta\rangle \qquad (2.12)\\ &- \frac{1}{\bar\rho\widetilde{P}(\zeta)}\frac{\partial}{\partial\zeta}[(1-\zeta)\bar\rho\widetilde{P}(\zeta)\langle Y_\alpha''\Pi''\mid\zeta\rangle].\end{aligned}$$

In this equation, $\langle\Pi|\zeta\rangle$ is the conditional evaporation rate, and it satisfies the relation $\Pi=\langle\Pi|\zeta\rangle+\Pi''$. Then the influence of liquid phase on the carrier gas is represented by the last two terms on the right hand side of equation (2.12).

The extended CMC formulation (Eq. (2.12)) has been successfully applied in two-phase flow simulations [67–69], including studies of spray autoignition [67, 68] or combustion processes in diesel engines with fuel post-injections [69]. However, due to the computational costs, a reduced chemical mechanism or modified one-step chemistry is usually adopted in the CMC simulations [67–69], which makes it improper for the prediction of the processes sensitive to the detailed chemistry, such as pollutant formation, local extinction and ignition [20, 70].

2.2.3 Flamelet Models

The flamelet model was developed based on the concept that a turbulent flame can be viewed as an ensemble of stretched laminar flamelets [71], and for each flamelet structure, the major heat release is considered to occur in a thin reaction zone around the stoichiometric surface [72]. For the non-premixed flame, the structure of flamelets can be described by a set of flamelet equations in the mixture fraction space as [17]

$$\rho\frac{\partial Y_\alpha}{\partial\tau}=\rho\frac{\chi}{2}\frac{\partial^2 Y_\alpha}{\partial\xi^2}+\dot\omega_\alpha, \qquad (2.13)$$

where Lewis number of unity and Fick's diffusion law have been assumed, and Y_α is the mass fraction of species α, $\dot\omega_\alpha$ the specific chemical reaction rate, and ξ is the mixture fraction. In the turbulent flow, the flamelets are stretched and strained by flow and turbulence, which is reflected by the scalar dissipation rate, χ, defined as the gradient of the mixture fraction [17]

$$\chi=2D\left(\frac{\partial\xi}{\partial x_i}\right)^2. \qquad (2.14)$$

The flamelet theory considers the turbulent flame essentially as constructed from an ensemble of thin stretched laminar flames; the intense chemical reactions take place in a thin layer, and the local flame surface is assumed to be flat. This is valid for reacting flows where chemical reactions are faster than the turbulent mixing. The regimes for

analyzing the situations where flamelet assumption is valid have been discussed by Borghi [73] and Peters [17, 74], respectively, for premixed and nonpremixed flames.

The laminar flamelet model is a very attractive approach for the inclusion of detailed chemistry in turbulent flame calculations. According to Eq. (2.13), different flamelet structures can be pre-generated by prescribing a series of specific values of χ, which can be used then to calculate and tabulate the gas species and temperature as a function of the mixture fraction and scalar dissipation rate. A flamelet library is obtained so that it can be used for later turbulent flame calculations.

As described by Eq. (2.13), the flamelet model has been mathematically formulated in the mixture fraction space, and the mass fraction of species evolves due to the molecular diffusion and chemical reactions shown as the first and second terms on the right hand side of the equation. In the spray flames, however, the effects of additional spray evaporation should have to be accounted for. Recently, Olguin and Gutheil [75] derived a flamelet equation considering the inter-phase exchange effects, which can be written as

$$\rho\frac{\partial Y_\alpha}{\partial \tau} = \rho\frac{\chi}{2}\frac{\partial^2 Y_\alpha}{\partial \xi^2} + \dot{\omega}_\alpha + S_\mathrm{v}(\xi - 1)\frac{\partial Y_\alpha}{\partial \xi} + S_\mathrm{v}(\delta_{l\alpha}S_\mathrm{v} - Y_\alpha), \tag{2.15}$$

with $\delta_{l\alpha}$ equals unity for the evaporating species and zero otherwise. Here, compared with Eq. (2.13), the last two terms on the right hand side are additional terms and reflect the dependence of flame structures on the spray evaporation source term, S_v. To solve this spray flamelet equation, the spray source terms conditioned on the mixture fraction have to be determined [76, 77] with some ad-hoc analysis, e.g. DNS studies.

Alternatively, a spray flamelet model based on the pre-calculation of laminar spray flame in a counterflow configuration has been proposed and used in the turbulent spray flame computations [78, 79]. This counterflow configuration shows several advantages such as the well-defined flow field and specifically the capability to include the spray evaporation effects directly in the flamelet calculations [79–81]. In this model, the physical coordinate system is first used to solve the governing equations for the opposed diffusion spray flames [81], and then the resulting flame structures are projected into the mixture fraction space for flamelet library generation.

Compared with the CMC model, the computational cost of the simulations is dramatically reduced by employing the flamelet models, where the detailed information of the flame structure is incorporated in the modeling by using the pre-generated flamelet library, instead of solving the transport equations of species mass fractions in both mixture fraction and physical spaces (see Eq. 2.12) as in the CMC model. Thus, the detailed chemical reaction mechanism and transport properties can be included in the flamelet modeling.

The spray flamelet model will be adopted in the present study for the turbulent

spray flame calculation, and more focus will lie on the extension of this model to account for the pre-vaporization effects and multiple combustion regimes.

2.2.4 Transported Probability Density Function Approach

The theory and application of probability density function (PDF) method for the turbulent flows has been studied for several decades. Lundgren first derived and solved a modeled transport equation for the joint PDF of gas velocity [82], and later Dopazo and O' Brien [83] for the joint PDF of compositions. The transported PDF method became very popular since Pope's work [25], where the discrete particle methods have been introduced to solve the modeled PDF transport equations. For the joint composition PDF, this model provides a complete statistical description of the turbulent flow by using a gas mass density function $F(\Psi; \mathbf{x}, t)$ [26]

$$F(\Psi; \mathbf{x}, t) = \rho(\Psi)\langle f^*(\Psi; \mathbf{x}, t)\rangle, \tag{2.16}$$

which is given in terms of the one-point one-time Eulerian fine-grained joint scalar PDF $f^*(\Psi; \mathbf{x}, t)$ [30]

$$f^*(\Psi; \mathbf{x}, t) = \delta(\Phi(\mathbf{x}, t) - \Psi) \equiv \prod_{\alpha=1}^{N_s} \delta(\Phi_\alpha(\mathbf{x}, t) - \Psi_\alpha), \tag{2.17}$$

where δ is the Dirac-delta function. Φ is the vector of the characteristic gas variables of interest, and Ψ corresponds to the sample space. $f^*(\Psi; \mathbf{x}, t)$ represents one single realization of the events $\{\Phi(\mathbf{x}, t) = \Psi\}$ at position $\mathbf{x}$ and time t.

In general, the main advantage of PDF methods is that, for the reacting flows, the nonlinear chemical source terms appear in closed form and thus, arbitrarily complex and non-linear chemical reactions can be treated in an exact way [25]. If the transported PDF of gas velocity is considered, the turbulent convective transport is in closed form [25]. Additionally, if more than one single dependent variable of the PDF is concerned, this method also shows the advantage pertaining to its capability of studying the correlation of different dependent variables in the turbulent flow field [84, 85]. PDF method has shown to be a powerful numerical approach for the modeling of a variety of combustion processes, e.g. local extinction, auto-ignition as well as pollution emissions [70, 86–89]. At the same time, a wide range of combustion modes including non-premixed and premixed combustion [90, 91] with various types of flame stabilization mechanisms, i.e. swirl-stabilized [92], pilot-stabilzed [86, 93] and bluff body stabilized [94] flames, are accounted for in this method.

The application of PDF methods to spray flows is very attractive. It provides a suitable approach to couple the spray processes to the turbulent fluid flow, since it allows for the consideration of the turbulent fluctuations of the fluid properties, and the

local PDF can be well represented in the presence of evaporating droplets [95], which is of crucial importance in reacting spray flows. The general form of the transport equation of the gas mass density function that includes the interphase exchange effects can be written as [78]

$$\frac{\partial F}{\partial t}+\frac{\partial(\langle U_i|\Psi\rangle F)}{\partial x_i}-\left\langle\frac{S_\mathrm{v}}{\rho}\middle|\Psi\right\rangle F=-\sum_{\alpha=1}^{N_\alpha}\frac{\partial}{\partial\Psi_\alpha}\left(\left\langle\frac{\mathrm{D}\Phi_\alpha}{\mathrm{D}t}\middle|\Psi\right\rangle F\right). \tag{2.18}$$

Here, U_i is the flow velocity. S_v denotes the spray evaporation effect on the gas density of ρ. $\langle\Phi|\Psi\rangle$ represents the conditional expectation of variable Φ with respect to Ψ. N_α is the number of characteristic gas variables Φ_α. The work about the application of transported PDF method in two-phase turbulent spray flows calculation can be found in Refs. [84, 87, 96–98].

In summary, the turbulent combustion models that have been extended to the simulation of reacting spray flows are introduced. Each model is initially proposed for the pure gas flames and is developed based on either statistical or geometrical analysis for the flame structures [40]. Therefore, different models embrace different predictive abilities and are suitable for capturing specific flame characteristics. Application of different models in the same simulation for the complex turbulent flames has been reported in recent years, especially a combined formulation of transported PDF methods and flamelet models [22, 84, 97, 99, 100], which leads to a desired combination of the strengths of each modeling approach, and the transported PDF methods provide the local statistics that flamelet model needs for its application in turbulent spray combustion simulation. Ge and Gutheil [78, 84] developed an approach for the computation of turbulent spray flame using a coupled transported PDF and spray flamelet method, where the dependent variables of the gas phase PDF include the mixture fraction and the gas enthalpy. This formulation has been successfully applied to the numerical simulation of spray flames that can be considered as mixing-controlled, but it may not work in more complex spray flames, showing especially both premixed and nonpremixed or partially premixed regimes.

In the present work, the combined formulation of the transported PDF method and spray flamelet model will be studied, and model development for mixed combustion regimes will be carried out in the comparison with experimental data of the complex turbulent ethanol/air spray flames, provided by Prof. Masri at the University of Sydney, Australia [101].

In the next chapter, the mathematical formulation of the models used as well as the corresponding numerical solution scheme are described.

3. Mathematical Models

The mathematical modeling of spray combustion concerns a two-phase flow problem, where spray droplets are carried by the continuous gas phase. Two-way interactions between gas and liquid phase take place through interphase exchange of mass, momentum and energy in a wide range of time and length scales. When chemical reactions are considered, the resulting heat release and density change further complexes the problem. In the next section, the basic equations and models for both gas and liquid phase are described.

3.1 Gas Phase

The governing equations of gas phase in the two-phase turbulent spray flows are described in this section, along with the corresponding thermodynamic properties and closure methods.

3.1.1 Governing Equations

For a chemically reacting spray flow, the instantaneous governing equations of the gas-phase for mass, momentum, energy and species mass fraction can be written as [102]

- Mass:

$$\frac{\partial \rho}{\partial t} + \frac{\partial (\rho U_i)}{\partial x_i} = S_{\mathrm{v}}, \tag{3.1}$$

- Momentum:

$$\frac{\partial (\rho U_j)}{\partial t} + \frac{\partial (\rho U_i U_j)}{\partial x_i} = -\frac{\partial p}{\partial x_j} + \frac{\partial \tau_{ij}}{\partial x_i} + \rho g_j + S_{\mathrm{m},j}, \tag{3.2}$$

- Energy:

$$\frac{\partial (\rho h)}{\partial t} + \frac{\partial (\rho U_i h)}{\partial x_i} = -\frac{\partial J_i^h}{\partial x_i} + \frac{\partial p}{\partial t} + \frac{\partial (\tau_{ij} U_i)}{\partial x_j} + S_{\mathrm{e}}, \tag{3.3}$$

- Mass fractions of chemical species:

$$\frac{\partial (\rho Y_\alpha)}{\partial t} + \frac{\partial (\rho U_i Y_\alpha)}{\partial x_i} = -\frac{\partial J_i^\alpha}{\partial x_i} + \dot{\omega}_\alpha + S_{\mathrm{v},\alpha}. \tag{3.4}$$

Here, ρ is the density of the gas mixture. U_j is the velocity of the carrier gas in the j-direction, and g_j the gravitational acceleration. p and h denote the static pressure and the total enthalpy, respectively. The scalars Y_α with $\alpha = 1, 2, ..., N_s$ represent the mass fractions of chemical species. τ_{ij}, J_i^h and J_i^α are the viscous stress tensor and molecular transport fluxes of enthalpy and species, respectively. $\dot{\omega}_\alpha$ denotes the specific chemical reaction rate of species α. S_v, $S_{\mathrm{m},j}$, S_e and $S_{\mathrm{v},\alpha} = \delta_{l\alpha} S_\mathrm{v}$ are source terms representing the influence of evaporating droplets on mass, momentum and energy of gas phase, and δ is the Dirac-delta function with [80]

$$\delta_{ij} = \begin{cases} 0 & \text{if } i \neq j \\ 1 & \text{if } i = j \ . \end{cases}$$

The viscous stress tensor τ_{ij} is defined by [30, 40, 80, 102]

$$\tau_{ij} = -\frac{2}{3}\mu \frac{\partial U_k}{\partial x_k}\delta_{ij} + \mu\left(\frac{\partial U_i}{\partial x_j} + \frac{\partial U_j}{\partial x_i}\right), \tag{3.5}$$

and, considering the negligible magnitude of the Dufour and Soret effects [102], the species mass flux J_i^α and the energy flux J_i^h are defined using the multicomponent forms of Fick's diffusion law and Fourier's conduction law, respectively, and they take the form [40, 102]

$$J_i^\alpha = -\rho D_\alpha \frac{\partial Y_\alpha}{\partial x_i}, \quad J_i^h = -\frac{\lambda}{C_p}\frac{\partial h}{\partial x_i}, \tag{3.6}$$

where D_α is the molecular diffusion coefficient of species α, λ is the thermal diffusivity, and C_p is the specific heat capacity at constant pressure. μ is the dynamic gas viscosity, and the kinematic viscosity ν is given as $\nu = \mu/\rho$.

Additionally, the second and third term on the right-hand side of Eq. (3.3) represent the compressibility effect and energy transfer due to viscous dissipation, and they are neglected in the low Mach number limit [102].

Due to the wide range of time and length scales involved in turbulent reacting flows, solving the complete governing equations Eqs. (3.1)-(3.4) directly in a full three-dimensional simulation will present an unaffordable computational cost. Thus, for most complex industrial combustion applications, the mean quantities become the ones of greatest practical interest.

In variable-density flows, Favre averaging shows advantage in simplifying the averaged governing equations, and the modeling of correlations related to the density fluctations is avoided [40, 103]. The Favre average of any turbulent flow quantities Φ is defined as [40, 103]

$$\widetilde{\Phi} = \frac{\langle \rho \Phi \rangle}{\langle \rho \rangle}, \tag{3.7}$$

and in this case, the instantaneous value Φ can be decomposed into its mean $\widetilde{\Phi}$ and fluctuating component, Φ'' as [40, 103]

$$\Phi = \widetilde{\Phi} + \Phi''. \tag{3.8}$$

After averaging the equations Eqs. (3.1)-(3.4), the Favre averaged governing equations yield [26, 40]

$$\frac{\partial\langle\rho\rangle}{\partial t} + \frac{\partial(\langle\rho\rangle\widetilde{U}_i)}{\partial x_i} = \langle S_\mathrm{v}\rangle \tag{3.9}$$

$$\frac{\partial(\langle\rho\rangle\widetilde{U}_j)}{\partial t} + \frac{\partial(\langle\rho\rangle\widetilde{U}_i\widetilde{U}_j)}{\partial x_i} = -\frac{\partial\langle p\rangle}{\partial x_j} + \frac{\partial}{\partial x_i}\Big(\langle\tau_{ij}\rangle - \langle\rho\rangle\widetilde{u_i''u_j''}\Big) + \langle\rho\rangle g_j + \langle S_{\mathrm{m},j}\rangle \tag{3.10}$$

$$\frac{\partial(\langle\rho\rangle\widetilde{h})}{\partial t} + \frac{\partial(\langle\rho\rangle\widetilde{U}_i\widetilde{h})}{\partial x_i} = -\frac{\partial}{\partial x_i}\Big(\langle J_i^h\rangle + \langle\rho\rangle\widetilde{u_i''h''}\Big) + \langle S_\mathrm{e}\rangle \tag{3.11}$$

$$\frac{\partial(\langle\rho\rangle\widetilde{Y}_\alpha)}{\partial t} + \frac{\partial(\langle\rho\rangle\widetilde{U}_i\widetilde{Y}_\alpha)}{\partial x_i} = -\frac{\partial}{\partial x_i}\Big(\langle J_i^\alpha\rangle + \langle\rho\rangle\widetilde{u_i''Y_\alpha''}\Big) + \langle\dot{\omega}_\alpha\rangle + \langle S_{\mathrm{v},\alpha}\rangle. \tag{3.12}$$

In the above equations, on the right hand side, the terms, representing the correlations between different quantities fluctuations, i.e. $\widetilde{u_i''u_j''}$, $\widetilde{u_i''h''}$ and $\widetilde{u_i''Y_\alpha''}$, denote the Reynolds stress, enthalpy, and species turbulent fluxes, respectively. They all are unclosed and need modeling, which will be further described in section (3.1.3).

3.1.2 Thermodynamic Properties

In addition to the governing equations introduced in last section, the full description of the gas phase is completed by the equation of state of an ideal gas [49]

$$p = \rho\bar{R}T, \tag{3.13}$$

and

$$\bar{R} = R/W, \tag{3.14}$$

where R is the universal gas constant with the approximate value of 8.314 J/(mol K). T is the gas temperature, W is the mean molecular weight of the gas mixture, given by

$$W = \sum_{\alpha=1}^{N_s} X_\alpha W_\alpha \quad \text{or} \quad W = \left[\sum_{\alpha=1}^{N_s} \frac{Y_\alpha}{W_\alpha}\right]^{-1}, \tag{3.15}$$

and the relation between the mass fraction Y_α and mole fraction X_α can be formulated as

$$Y_\alpha = \frac{W_\alpha}{W} X_\alpha, \tag{3.16}$$

where W_α is the molecular weight of species α.

In Eq. (3.3), the energy considered is the total enthalpy, h, which is the combination of sensible enthalpy, mass formation enthalpy, and kinetic energy, which can be given for a multi-component system as [49]

$$h = \sum_{\alpha=1}^{N_s} h_\alpha Y_\alpha + \frac{1}{2} U_i U_i, \tag{3.17}$$

and

$$h_\alpha = \int_{T_o}^{T} C_{p\alpha}(T')dT' + \Delta h^o_{f,\alpha}.$$

In the last equation, the first term at the right-hand side is the sensible enthalpy and the second term $\Delta h^o_{f,\alpha}$ is the mass formation enthalpy of species α at reference temperature $T_\mathrm{o} = 298.15K$. The sensible enthalpy at this reference temperature is set to zero. $C_{p\alpha}(T)$ is the specific heat capacity at constant pressure, and its temperature dependence is represented by NASA polynomials [104]

$$C_{p\alpha}(T) = R \sum_{n=1}^{5} a_{n,\alpha} T^{n-1}. \tag{3.18}$$

For the evaluation of viscosity μ and thermal conductivity λ of the mixture, the semi-empirical formulation is used [105, 106]

$$\mu = \frac{1}{2}\Big[\sum_{\alpha=1}^{N_s} X_\alpha \mu_\alpha + \Big(\sum_{\alpha=1}^{N_s} X_\alpha/\mu_\alpha\Big)^{-1}\Big] \tag{3.19}$$

$$\lambda = \frac{1}{2}\Big[\sum_{\alpha=1}^{N_s} X_\alpha \lambda_\alpha + \Big(\sum_{\alpha=1}^{N_s} X_\alpha/\lambda_\alpha\Big)^{-1}\Big], \tag{3.20}$$

the mixture diffusion coefficient of species α is computed as [107]

$$D_{\alpha,m} = \frac{1 - Y_\alpha}{\sum_{\beta\neq\alpha}^{N_s} X_\beta / D_{\beta\alpha}}. \tag{3.21}$$

In Eqs. (3.19), (3.20) and (3.21), the viscosity (μ_α), thermal conductivity (λ_α) for pure species, and the binary diffusion coefficients $D_{\beta\alpha}$ are approximated using polynomial fits [108]

$$\ln(\mu_\alpha) = \sum_{n=1}^{4} a_{n,\alpha} (\ln T)^{n-1} \tag{3.22}$$

$$\ln(\lambda_\alpha) = \sum_{n=1}^{4} b_{n,\alpha} (\ln T)^{n-1}, \tag{3.23}$$

and

$$\ln(D_{\beta\alpha}) = \sum_{n=1}^{4} d_{n,\beta\alpha}(\ln T)^{n-1}, \tag{3.24}$$

where the coefficients $a_{n,\alpha}$, $b_{n,\alpha}$ and $d_{n,\beta\alpha}$ are given in a tabulated form [108].

3.1.3 Turbulence Models

In Eqs. (3.10)- (3.12), the turbulent Reynolds stress as well as the turbulent fluxes of species and enthalpy are still unclosed, and turbulence models are needed. According to the turbulent eddy viscosity hypothesis made by Boussinesq [109], the Reynolds stress can be modeled with an eddy viscosity as [30, 48]

$$-\widetilde{u_i'' u_j''} = -\frac{2}{3}\nu_t \frac{\partial \widetilde{U}_k}{\partial x_k}\delta_{ij} + \nu_t\left(\frac{\partial \widetilde{U}_i}{\partial x_j} + \frac{\partial \widetilde{U}_j}{\partial x_i}\right). \tag{3.25}$$

This formulation is similar to equation (3.5) of the viscosity stress tensor τ_{ij}. Here, ν_t denotes the turbulent kinematic viscosity and the turbulent dynamic viscosity is $\mu_t = \langle\rho\rangle\nu_t$.

In the Boussinesq eddy-viscosity hypothesis, the turbulent eddies are conceived to act like molecules, and collide and exchange momentum. The molecular viscosity is linked to the average velocity and mean free path of the molecules. In this sense, ν_t is usually assumed to be proportional to the product of the characteristic length scale l_0 and the velocity scale u_0 of eddies in largest size range [30]

$$\nu_t \propto u_0 l_0, \tag{3.26}$$

and the large eddies characteristic length scale l_0 and velocity scale u_0 can be described with the relations [48]

$$u_0 \propto k^{1/2}, \quad l_0 \propto k^{3/2}/\epsilon, \tag{3.27}$$

which then results in [48]

$$\nu_{\mathrm{t}} = C_\mu \frac{k^2}{\epsilon}, \tag{3.28}$$

where C_μ is a model constant with standard value of 0.09 [48].

In the present work, a two-equation turbulence model, i.e. $k-\epsilon$ model is adopted to evaluate the turbulent eddy viscosity. In this model, the transport equations for both turbulent kinetic energy k and its dissipation rate ϵ are solved. The k and ϵ are defined as [30]

$$k = \frac{1}{2}\sum_{k=1}^{3} \widetilde{u_k'' u_k''}, \tag{3.29}$$

and

$$\epsilon = \overline{\nu \frac{\partial u_i''}{\partial x_j} \frac{\partial u_i''}{\partial x_j}}, \tag{3.30}$$

assuming isotropy of turbulence. Making use of the instantaneous equation (3.2) and the equation for the mean velocity Eq. (3.10), and after closure models are employed for the terms representing correlations between different variable's fluctuations, the corresponding transport equations for k and ϵ, taking into account the spray evaporation effect, can be derived and written as [110]

$$\frac{\partial(\langle\rho\rangle k)}{\partial t} + \frac{\partial(\langle\rho\rangle \widetilde{U}_j k)}{\partial x_j} - \frac{\partial}{\partial x_j}\left(\Gamma_k \frac{\partial k}{\partial x_j}\right) = G_k - \langle\rho\rangle\epsilon + \langle S_k\rangle \tag{3.31}$$

$$\frac{\partial(\langle\rho\rangle \epsilon)}{\partial t} + \frac{\partial(\langle\rho\rangle \widetilde{U}_j \epsilon)}{\partial x_j} \quad - \quad \frac{\partial}{\partial x_j}\left(\Gamma_\epsilon \frac{\partial \epsilon}{\partial x_j}\right) = (C_{\epsilon 1} G_k - C_{\epsilon 2}\langle\rho\rangle\epsilon)\frac{\epsilon}{k} + \langle S_\epsilon\rangle, \tag{3.32}$$

where the production term, G_k of k is given as [48, 110]

$$G_k = \mu_t \left\{ \left(\frac{\partial \widetilde{U}_j}{\partial x_i} + \frac{\partial \widetilde{U}_i}{\partial x_j}\right) - \frac{2}{3}\left(\frac{\partial \widetilde{U}_k}{\partial x_k}\right)\delta_{ij} \right\} \frac{\partial \widetilde{U}_i}{\partial x_j}. \tag{3.33}$$

In equations (3.31) and (3.32), S_k and S_ϵ represent the droplet effects on the turbulent kinetic energy and its dissipation rate, respectively, and the model constants used here are $C_{\epsilon 1} = 1.44$ and $C_{\epsilon 2} = 1.92$ [110]. Γ_ϕ is the exchange coefficient for any considered variable ϕ, and is defined as $\Gamma_\phi = \mu/\sigma_\Phi + \mu_\mathrm{t}/\sigma_{\Phi,\mathrm{t}}$, where σ_Φ and $\sigma_{\Phi,\mathrm{t}}$ denote the laminar and turbulent Prandtl or Schmidt number, respectively.

The gradient-diffusion assumption [30, 48] is then usually applied to determine the turbulent scalar fluxes in Eqs. (3.11) and (3.12)

$$\widetilde{u_i'' h''} = -\frac{\nu_\mathrm{t}}{\mathrm{Sc_t}} \frac{\partial \widetilde{h}}{\partial x_i}, \quad \widetilde{u_i'' Y_\alpha''} = -\frac{\nu_\mathrm{t}}{\mathrm{Sc_t}} \frac{\partial \widetilde{Y}_\alpha}{\partial x_i}. \tag{3.34}$$

After applying Eqs. (3.25) and (3.34) to Eqs. (3.10) - (3.12), the closed equation set for gas flow yields

$$\begin{aligned} \frac{\partial(\langle\rho\rangle \widetilde{U}_j)}{\partial t} + \frac{\partial(\langle\rho\rangle \widetilde{U}_i \widetilde{U}_j)}{\partial x_i} = & - \frac{\partial\langle p\rangle}{\partial x_j} + \frac{\partial}{\partial x_i}\left[\mu_t\left(\frac{\partial \widetilde{U}_j}{\partial x_i} + \frac{\partial \widetilde{U}_i}{\partial x_j} - \frac{2}{3}\frac{\partial \widetilde{U}_k}{\partial x_k}\delta_{ij}\right)\right] \\ & + \langle\rho\rangle g_j + \langle S_{\mathrm{m},j}\rangle \end{aligned} \tag{3.35}$$

$$\frac{\partial(\langle\rho\rangle \widetilde{h})}{\partial t} + \frac{\partial(\langle\rho\rangle \widetilde{U}_i \widetilde{h})}{\partial x_i} = \frac{\partial}{\partial x_i}\left(\Gamma_\mathrm{h} \frac{\partial \widetilde{h}}{\partial x_i}\right) + \langle S_\mathrm{e}\rangle \tag{3.36}$$

$$\frac{\partial(\langle\rho\rangle\widetilde{Y}_\alpha)}{\partial t}+\frac{\partial(\langle\rho\rangle\widetilde{U}_i\widetilde{Y}_\alpha)}{\partial x_i}=\frac{\partial}{\partial x_i}\big(\Gamma_{\mathrm{M}}\frac{\partial\widetilde{Y}_\alpha}{\partial x_i}\big)+\langle\dot{\omega}_\alpha\rangle+\langle S_{\mathrm{v},\alpha}\rangle. \tag{3.37}$$

The $k-\epsilon$ model is the most widely used turbulence model for its simple form and easy applications. For turbulent flows with swirl or large curvature, this model shows some deficiencies [48]. More sophisticated second-order closure models, like Reynolds Stress Models (RSM) or Algebraic Stress Model (ASM) [48] are preferred in that case. The detailed description about the RSM or ASM may be found in the references [30, 48]. In the present work, the extended $k-\epsilon$ model with extra terms accounting for spray effects [110], is applied and discussed in the simulations of two-phase jet flows and flames.

3.2 Combustion Chemistry

In a chemically reacting flow, chemical reactions and the associated heat release complex the flow and change the thermodynamic as well as the transport properties of the gas mixture, like the mass density, viscosity, and diffusivity, etc. In the reacting spray flows, the local gas properties of the flow are also important for the rate of mass and heat transfer between the gas and the liquid phases, and thus, they determine the process of fuel supply due to evaporation. Therefore, the proper inclusion of the chemical reaction mechanisms in the numerical simulations is required.

3.2.1 Chemical Source Terms

The chemical source terms $\dot{\omega}_\alpha$ represent the mass reaction rate of species α in a system consisting of N_r elementary reactions. The j-th reaction involving different species M_α may be written as [46, 49, 111]

$$\sum_{\alpha=1}^{N_s}\nu'_{\alpha j}M_\alpha\overset{k_{fj}}{\underset{k_{bj}}{\rightleftharpoons}}\sum_{\alpha=1}^{N_s}\nu''_{\alpha j}M_\alpha,\qquad j=1,2,...,N_r, \tag{3.38}$$

and the mass conservation is implied by

$$\sum_{\alpha=1}^{N_s}\nu'_{\alpha j}W_\alpha=\sum_{\alpha=1}^{N_s}\nu''_{\alpha j}W_\alpha,\qquad j=1,2,...,N_r, \tag{3.39}$$

here W_α is the molecular weight of species α. $\nu'_{\alpha j}$ and $\nu''_{\alpha j}$ denote the stoichiometric coefficients of species α as reactant or product in j-th reaction, respectively. k_{fj} and k_{bj} are the forward and backward reaction rates, respectively.

The specific chemical reaction rate of species α can then be calculated as [49, 111]

$$\dot{\omega}_\alpha=W_\alpha\sum_{j=1}^{N_r}\nu_{\alpha j}\dot{\omega}_j=W_\alpha\sum_{j=1}^{N_r}\nu_{\alpha j}(\dot{\omega}_{fj}-\dot{\omega}_{bj}),\qquad \alpha=1,2,...,N_s, \tag{3.40}$$

with

$$\nu_{\alpha j} = \nu''_{\alpha j} - \nu'_{\alpha j}, \tag{3.41}$$

where $\nu_{\alpha j}$ is the net stoichiometric coefficient, and the forward $\dot{\omega}_{fj}$ and backward $\dot{\omega}_{bj}$ reaction rates of an elementary reaction j are given by [49, 111]

$$\dot{\omega}_{fj} = k_{fj} \prod_{\alpha=1}^{N_s} \left(\frac{\rho Y_\alpha}{W_\alpha} \right)^{\nu'_{\alpha j}}, \quad \dot{\omega}_{bj} = k_{bj} \prod_{\alpha=1}^{N_s} \left(\frac{\rho Y_\alpha}{W_\alpha} \right)^{\nu''_{\alpha j}}. \tag{3.42}$$

Here, k_{fj} and k_{bj} are temperature dependent and can be expressed by the modified Arrhenius equation as [49, 102, 111]

$$k_j = A_j T^{\beta_j} \exp\left(- \frac{E_{aj}}{RT} \right), \tag{3.43}$$

where E_{aj} is the activation energy. $A_j T^{\beta_j}$ represents the collision frequency and the temperature exponential term is associated with the effect of internal molecular orientation, where the exponent β_j lies between 0 and 1 [102].

3.2.2 Reduced Chemistry

The local gas properties are usually characterized by a set of scalar variables ϕ, including the mass fraction of all species and the gas enthalpy (or temperature)

$$\phi = \{Y_1, Y_2, ..., Y_{N_s}, h\}. \tag{3.44}$$

In a practical combustion system, the number of chemical species involved can be enormous, of the order of 50 to 7,000 depending on the type of fuel [16]. In addition to such a large size, the detailed mechanism is also characterized by the wide range of time scales associated with different species and elementary reactions, which, most often, results in severe chemical stiffness in the numerical simulations [112]. Hence, the large size and chemical stiffness usually make it intractable to include detailed reaction mechanisms in the simulation of real combustion systems. However, these details are of vital importance for proper prediction of, for instance, the pollutant formation, local extinction and ignition in combustion applications [20, 70]. In this context, a reduced chemistry description is required for decreasing computational cost while preserving the relevant characteristics of chemical mechanisms.

The various reduction approaches developed can be categorized as follows. Skeletal reduction is often implemented as the first step for the reduction of the detailed mechanism through the elimination of the unimportant species and reactions [113]. Directed relation graph (DRG) [113, 114] represents one of these methods, and it is shown to be capable of quickly bringing down the large detailed kinetics to much smaller sizes

that can be further reduced by other methods. For the detailed mechanism of methyl decanoate, the number of species can be reduced from 3036 to 125 with around 20% of reduction error [112]. DRG employs a species coupling analysis based on a relation graph, which illustrates the relations through which the species are coupled. By checking the connection of species in this constructed graph, the species that are weakly coupled to the major species can be detected and defined as the unimportant species.

Time-scale analysis is another type of mechanism reduction approach that includes the classical quasi-steady state approximation or partial equilibrium approximations [115], as well as more systematic method, i.e. intrinsic low dimensional manifold (ILDM) [116, 117] and computational singular perturbation (CSP) [118, 119] that are based on Jacobian analysis. The fast chemical processes, induced by either fast depleting species or fast reversible reactions, lead to the exhausted fast modes and consequently, to the algebraic equations characterizing the steady-state subspace. By doing this, the number of the thermo-chemical variables solved by the differential transport equations is reduced.

Sensitivity analysis is another popular reduction method [11]. In this method, the sensitivity of the reaction rate of species with respect to the rate coefficients of elementary reactions is first analyzed by the defined sensitivity coefficients, and in this way, the elementary reactions that are rate-limiting are identified [11]. Then, the information obtained by this method can be used to eliminate unimportant reactions.

3.2.3 Gas Flamelet Models

The flamelet models that have been proposed firstly by Peters [17] for the gas nonpremixed flames represents another type of dimension reduction method [26]. In this model, the detailed thermochemical states ϕ in Eq. (3.44), characterizing the flame structure, can be parameterized by a set of characteristic variables Ψ (e.g. the mixture fraction and scalar dissipation rate for the nonpremixed flames) [17, 49, 71]

$$\phi = \phi(\Psi). \tag{3.45}$$

In the flamelet theory, the turbulent flame is considered as consisting of an ensemble of one-dimensional stretched laminar flames; the combustion takes place in a thin layer, and the local flame surface is assumed to be flat. A series of *a priori* generated laminar flame structures are used in the simulation of the turbulent flames, in combination with a probability density function, to account for the effect of turbulent fluctuations. These pre-computed laminar flame structures are often referred to flamelets, and they are tabulated in a flamelet library for later use. In this case, the detailed chemical kinetics and transport properties can be easily included in the turbulent combustion simulations without requiring high computational costs associated with the solution of

many species and nonlinear chemical reaction rates. The Favre-averaged mean value of variable ϕ can then be calculated as [17, 71]

$$\widetilde{\phi} = \int_{-\infty}^{\infty} \phi(\Psi)\ \widetilde{f}(\Psi)\ \mathrm{d}\Psi, \tag{3.46}$$

where $\phi(\Psi)$ is the value interpolated from the flamelet libraries, and $\widetilde{f}(\Psi)$ represents the Favre-averaged probability density function of variables Ψ.

In the nonpremixed flames, the fuel and air are separated before entering the reaction zone. The chemical reactions are, therefore, mixing controlled, and characterized by the mixing state between fuel and oxidizer, i.e. the mixture fraction ξ and the scalar dissipation rate χ, which represents the straining effects imposed on reaction zones and measures the characteristic diffusion time [17, 72]. In the present work, the mixture fraction ξ is defined in terms of mass fractions of the chemical element carbon C, Y_{C} [72, 95]

$$\xi = \frac{Y_{\mathrm{C}} - Y_{\mathrm{C,min}}}{Y_{\mathrm{C,max}} - Y_{\mathrm{C,min}}}, \tag{3.47}$$

where

$$Y_{\mathrm{C}} = \sum_{\alpha=1}^{N_s} \frac{\beta_{\alpha\mathrm{C}} W_{\mathrm{C}}}{W_\alpha} Y_\alpha. \tag{3.48}$$

Y_α is the the mass fraction of α-th species within the system with N_s chemical species, and $\beta_{\alpha C}$ denotes the mole number of the element carbon in species α. In addition, the scalar dissipation rate is given by the equation (2.14).

In this situation, these two variables, ξ and χ, are chosen as the characteristic variables Ψ, and the mean value of ϕ is expressed as [71]

$$\widetilde{\phi} = \int_0^\infty \int_0^1 \phi(\xi,\chi)\ \widetilde{f}(\xi,\chi)\ \mathrm{d}\xi\ \mathrm{d}\chi, \tag{3.49}$$

where the $\widetilde{f}(\xi,\chi)$ is the joint probability density function of ξ and χ.

In most practical combustion systems, however, the reactive flows are usually characterized with different burning modes, i.e. ranging from pure premixed or nonpremixed combustion to partially premixed combustion. The development of flamelet models to accommodate this multiple combustion regime has been the focus recent years [120–123]. Usually, when the finite-rate chemistry effect becomes important, a reactive scalar Y_{P} referred to as reaction progress variable is defined to characterize the progress of combustion reactions between unburnt and burnt states. Thus, a combination of conserved scalar ξ and reactive scalar Y_{P} is often employed in newly developed flamelet models, for example, the flamelet/progress-variable (FPV) [124–126], flamelet-generated manifolds (FGM) [127, 128], and the flame-prolongation of ILDM (FPI) [129–131].

Furthermore, in the spray combustion, the flames become heavily dependent on the spray behavior, and they are characterized by the turbulent dispersion of evaporating droplets, which causes strong interactions between turbulence, chemistry and sprays. An evaporation-controlled combustion regime is identified [75]. Therefore, a consistent flamelet model adequately accounting for the multiple combustion regimes affected by the spray evaporation effects in two-phase reacting flows is needed.

3.2.4 Spray Flamelet Model

In reactive spray flows, the presence of evaporating liquid complex the local gaseous combustion [31, 132]. The dispersed droplets are the principle contribution of vapor fuels, thus, creating a strong coupling between droplet dynamics and combustion models. Implementation of the gas flamelet model in spray flame calculation cannot fully capture the reaction zones where chemical reactions and evaporation are closely intercoupled [75, 133, 134]. Hollmann and Gutheil [133] proposed a spray flamelet model based on the laminar spray flame, which incorporates the effect of droplet evaporation directly in the flamelet structures and shows to be a promising way to simulate the evaporation-dominated flame regimes. In this extended formulation, the spray flamelet structures depend not only on the mixture fraction and the scalar dissipation rate, but also on the initial droplet radius, R_0, the initial spray velocity, v_0, and the global equivalence ratio E at the spray inlet [135]. Thus, different from the classical formulation of gas flamelet model, Eq. (3.49), the use of this spray flamelet in the simulation of turbulent spray flames takes the form [133]

$$\widetilde{\phi} = \int_0^\infty \int_{-\infty}^\infty \int_0^\infty \int_0^\infty \int_0^1 \phi \; \widetilde{f}(\xi, \chi, R_0, v_0, E) \; \mathrm{d}\xi \; \mathrm{d}\chi \; \mathrm{d}R_0 \; \mathrm{d}v_0 \; \mathrm{d}E. \tag{3.50}$$

In the spray flamelet model, the laminar spray flames in a counterflow configuration are precalculated, and the resulting flame structures of relevant species mass fractions are then transformed into the mixture fraction space and tabulated in a spray flamelet library for later use in the turbulent flame calculations. Compared with the gas flamelet model, the calculations with this spray flamelets can correctly reproduce the flame structures strongly influenced by the spray evaporation [133]. This approach has already been successfully applied in the numerical simulations of turbulent spray flames that are mainly controlled by the turbulent mixing and evaporation [84, 133].

In the present study, the extension of this spray flamelet model to the simulations of more complex spray flames, showing both premixed and non-premixed or partially-premixed regimes, is discussed and studied. The reaction progress variable is introduced for this purpose, and a new formulation of the spray flamelet approach is proposed. The

flamelet structures are tabulated with an additional parameter, which is the reaction progress variable, instead of the scalar dissipation rate of the mixture fraction [136]

$$\widetilde{\phi} = \int_0^{\infty}\int_{-\infty}^{\infty}\int_0^{\infty}\int_0^1\int_0^1 \phi\ \widetilde{f}(\xi, Y_{\mathrm{P}}, R_0, v_0, E)\ \mathrm{d}\xi\ \mathrm{d}Y_{\mathrm{P}}\ \mathrm{d}R_0\ \mathrm{d}v_0\ \mathrm{d}E. \tag{3.51}$$

The reaction progress variable Y_{P} characterizes the progress of chemical reactions, and it defines an important dimension in the reduced sub-space with which the evolution of chemical composition in the spray combustion, with complex local flame structures or combustion regimes, can be described. A commonly used definition of Y_{P} is based on the mass fraction of combustion products CO_2 and H_2O [137]

$$Y_{\mathrm{P}} = Y_{\mathrm{CO_2}} + Y_{\mathrm{H_2O}}, \tag{3.52}$$

and further, based on this definition and the instantaneous species transport equation (3.4), the transport equation for Y_{P} can be given as [48]

$$\frac{\partial(\rho Y_{\mathrm{P}})}{\partial t} + \frac{\partial(\rho U_i Y_{\mathrm{P}})}{\partial x_i} = \frac{\partial}{\partial x_i}\big(\Gamma_{\mathrm{P}}\frac{\partial Y_{\mathrm{P}}}{\partial x_i}\big) + \dot{\omega}_P. \tag{3.53}$$

Here, Eq. (3.6) has been applied to evaluate the species mass flux in Eq. (3.4). $\dot{\omega}_P$ is the chemical source term for the reaction progress variable, and it is defined as $\dot{\omega}_P = \dot{\omega}_{\mathrm{C_2O}} + \dot{\omega}_{\mathrm{H_2O}}$. Similarly, the equation of the mixture fraction ξ, following its definition Eq. (3.47), can be written as [110]

$$\frac{\partial(\rho\xi)}{\partial t} + \frac{\partial(\rho U_i \xi)}{\partial x_i} = \frac{\partial}{\partial x_i}\big(\Gamma_{\mathrm{M}}\frac{\partial \xi}{\partial x_i}\big) + S_{\mathrm{v}}. \tag{3.54}$$

In Eq. (3.51), integration over the sample space is applied to evaluate the mean composition, where $\widetilde{f}$ is defined as the joint probability density function (PDF) of the considered major quantities. To evaluate this joint PDF, assumption of statistical independence between different variables is commonly employed when using moment methods (i.e. the methods based on solution of first and second moment equations) [133, 137–140], and it allows the splitting of the joint PDF into marginal PDFs, and the presumed parameterized forms are used to represent the PDF of each characteristic variables of the flamelet structures.

In turbulent spray flames, however, the scalar statistical distribution will involves a significant dependence on not only the local turbulent mixing, but also the spray evaporation, which as a result, makes the assumptions of the presumed PDF form invalid. In particular, due to the presence of evaporating droplets, the mixture fraction is no longer a conserved scalar. The standard presumed β function was found to be inappropriate for the correct approximation of the mixture fraction PDF in spray combustion [31, 95, 141–143]. An alternative approach has been developed in this situation to solve the transport equation of the joint PDF of considered scalar variables, the basic theory and transport equations of which are described in the next section.

3.3 Transported Joint Probability Density Function Method

3.3.1 Statistical Description

The statistical description of the turbulent gas flows is obtained by using the probability density function $f(\Psi;\mathbf{x},\mathbf{t})$ [30]

$$f(\Psi;\mathbf{x},t)=\langle f^{*}(\Psi;\mathbf{x},t)\rangle, \tag{3.55}$$

which is given in terms of the one-point one-time Eulerian fine-grained joint PDF $f^{*}(\Psi;\mathbf{x},t)$ [30](see Eq. (2.17)). Here, the bracket $\langle\rangle$ denotes the ensemble average. Given any function $Q=Q(\mathbf{x},t)$, its conditional mean can be related to $f(\Psi;\mathbf{x},t)$ by [26]

$$\langle Q(\mathbf{x},t)f^{*}(\Psi;\mathbf{x},t)\rangle=\langle Q(\mathbf{x},t)|\Psi\rangle f(\Psi;\mathbf{x},t), \tag{3.56}$$

and the expected value can be computed as [26]

$$\langle Q(\mathbf{x},t)\rangle=\int_{-\infty}^{\infty}\langle Q(\mathbf{x},t)|\Psi\rangle f(\Psi;\mathbf{x},t)\mathrm{d}\Psi. \tag{3.57}$$

In variable density flows, it is more convenient to work with the density-weighted average [144], which is accomplished by the use of gas mass density function $F(\Psi;\mathbf{x},t)$

$$F(\Psi;\mathbf{x},t)=\rho(\Psi)f(\Psi;\mathbf{x},t), \tag{3.58}$$

then the Favre-averaged mean can be expressed as [26, 144]

$$\widetilde{Q}(\mathbf{x},t)=\frac{\langle\rho Q\rangle}{\langle\rho\rangle}=\frac{\int_{-\infty}^{\infty}Q(\Psi)F(\Psi;\mathbf{x},t)\mathrm{d}\Psi}{\int_{-\infty}^{\infty}F(\Psi;\mathbf{x},t)\mathrm{d}\Psi}. \tag{3.59}$$

In the present study, the transport equation for the mass density function will be derived and solved in the context of two-phase turbulent evaporating spray flows.

3.3.2 Transport Equations of the Joint PDF

In this section, the transport equations of the joint PDF that include the spray evaporation effects are described. For the nonreacting spray flows, the momentum and turbulent mixing are crucial for the evolution of the disperse phase, the dependent variable of joint PDF include the gas velocity and scalar (mixture fraction); in the simulation of spray flames, in order to account for the partially premixed regime, the joint scalar PDF with three dependent variables of a mixture fraction, a reaction progress variable and gas enthalpy is considered.

3.3.2.1 Joint Gas Velocity-Scalar PDF Transport Equation

In this work, a transported joint gas velocity-mixture fraction PDF method is considered for the simulation of turbulent non-reacting spray flows. In this case, the fine grained joint PDF including the dependent variables of gas velocity and mixture fraction is given by [25, 145]

$$f^*(\Psi;\mathbf{x},t)=\delta(\mathbf{U}(\mathbf{x},t)-\mathbf{V})\delta(\xi(\mathbf{x},t)-\zeta), \tag{3.60}$$

and based on the governing equations for gas velocity (Eq. (3.2)) and mixture fraction (Eq. (3.54)), the transport equation of joint velocity-mixture fraction PDF can be derived as [25, 145]

$$\begin{aligned}\frac{\partial F}{\partial t}+\frac{\partial (V_i F)}{\partial x_i}-\left\langle \frac{S_\mathrm{v}}{\rho}\middle|\Psi\right\rangle F+(g_i-\frac{1}{\langle\rho\rangle}\frac{\partial\langle p\rangle}{\partial x_i})\frac{\partial F}{\partial V_i}\\ =\frac{\partial}{\partial V_i}\left(\left\langle -\frac{1}{\rho}\frac{\partial \tau'_{ij}}{\partial x_j}+\frac{1}{\rho}\frac{\partial p'}{\partial x_i}-\frac{1}{\rho}(S_{\mathrm{m},i}-U_i S_\mathrm{v})\middle|\Psi\right\rangle F\right)\\ -\frac{\partial}{\partial \zeta}\left(\left\langle \frac{1}{\rho}\frac{\partial}{\partial x_i}(\Gamma_\mathrm{M}\frac{\partial \xi}{\partial x_i})+\frac{1}{\rho}(1-\xi)S_\mathrm{v}\middle|\Psi\right\rangle F\right).\end{aligned} \tag{3.61}$$

In this equation, the terms on the right-hand side are unclosed; they represent the evolution in the velocity space and mixture fraction space, respectively, due to the pressure fluctuations, viscous dissipation, molecular mixing, and inter-phase exchange effects. In this work, the fluctuating component of acceleration due to the fluctuating pressure gradient and viscous forces (i.e. the first two terms in the velocity sample space) is modeled by a typical closure approach called simplified Langevin model given as [48, 146]

$$\left\langle -\frac{1}{\rho}\frac{\partial \tau'_{ij}}{\partial x_j}+\frac{1}{\rho}\frac{\partial p'}{\partial x_i}\middle|\Psi\right\rangle=(\frac{1}{2}+\frac{3}{4}C_0)\omega_\mathrm{t}(V_i-\langle V_i\rangle)-\frac{C_0\epsilon}{2F}\frac{\partial F}{\partial V_i}, \tag{3.62}$$

which is applied in the present work for the simulation of turbulent two-phase flows. Here, the parameter $C_0 = 2.1$ [25], and ω_t is the turbulence mixing frequency.

The first term in the mixture fraction space represents the PDF evolution by molecular diffusion, the closure of which needs two-point information of scalar; one-point joint PDF cannot account for the gradient statistics [25]. The modeling approach for this unclosed term will be discussed in the following subsections.

3.3.2.2 Joint Scalar PDF Transport Equation

In the previous studies [78, 84], a transported two-variate joint PDF method with considering dependent variables of the mixture fraction ξ and gas enthalpy h was successfully applied to consider the turbulent fluctuations in turbulent spray flames. In

the present work, the newly proposed spray flamelet formulation (Eq. (3.51)) suggests the derivation and solution of a three-variate joint PDF, where together with previous parameters, the chemical reaction progress variable Y_{P} is also added. Thus, a PDF transport equation for $\Phi = (\xi, Y_{\mathrm{P}}, h)$ will be addressed, and the corresponding $f^*(\Psi; \mathbf{x}, t)$ takes the form [136, 147]

$$f^*(\Psi; \mathbf{x}, t) = \delta(\xi(\mathbf{x}, t) - \zeta)\delta(Y_{\mathrm{P}}(\mathbf{x}, t) - \eta)\delta(h(\mathbf{x}, t) - \theta), \tag{3.63}$$

where the sample space $\Psi = (\zeta, \eta, \theta)$ corresponds to the mixture fraction, reaction progress variable and gas enthalpy, respectively.

Derivation of PDF transport equation usually can be achieved by two different approaches [25, 148]. In this work, the transport equation will be derived through the use of the properties of the fine grained PDF $f^*(\Psi; \mathbf{x}, t)$. With the chain rule and the properties of delta-function, the temporal and spatial derivatives of fine-grained PDF f^* are obtained as

$$\frac{\partial f^*}{\partial t} = -\frac{\partial f^*}{\partial \zeta}\frac{\partial \xi}{\partial t} - \frac{\partial f^*}{\partial \eta}\frac{\partial Y_{\mathrm{P}}}{\partial t} - \frac{\partial f^*}{\partial \theta}\frac{\partial h}{\partial t} \tag{3.64}$$

$$\frac{\partial f^*}{\partial x_i} = -\frac{\partial f^*}{\partial \zeta}\frac{\partial \xi}{\partial x_i} - \frac{\partial f^*}{\partial \eta}\frac{\partial Y_{\mathrm{P}}}{\partial x_i} - \frac{\partial f^*}{\partial \theta}\frac{\partial h}{\partial x_i}. \tag{3.65}$$

Making use of these formulations, the material derivative of f^* may be expressed as

$$\begin{aligned}
\rho\frac{\mathrm{D}f^*}{\mathrm{D}t} &= \rho\frac{\partial f^*}{\partial t} + \rho U_i\frac{\partial f^*}{\partial x_i} \\
&= -\rho\frac{\partial f^*}{\partial \zeta}\left(\frac{\partial \xi}{\partial t} + U_i\frac{\partial \xi}{\partial x_i}\right) - \rho\frac{\partial f^*}{\partial \eta}\left(\frac{\partial Y_{\mathrm{P}}}{\partial t} + U_i\frac{\partial Y_{\mathrm{P}}}{\partial x_i}\right) - \rho\frac{\partial f^*}{\partial \theta}\left(\frac{\partial h}{\partial t} + U_i\frac{\partial h}{\partial x_i}\right) \\
&= -\frac{\partial}{\partial \zeta}\left(\rho\frac{\mathrm{D}\xi}{\mathrm{D}t}f^*\right) - \frac{\partial}{\partial \eta}\left(\rho\frac{\mathrm{D}Y_{\mathrm{P}}}{\mathrm{D}t}f^*\right) - \frac{\partial}{\partial \theta}\left(\rho\frac{\mathrm{D}h}{\mathrm{D}t}f^*\right).
\end{aligned} \tag{3.66}$$

Inserting the continuity equation (3.1) into the left-hand side of above equation, taking the ensemble average, and using Eqs. (3.55), (3.56) and (3.58), the transport equation of the gas mass density function including two-phase exchange effects, can then be written as [147]

$$\begin{aligned}
\frac{\partial F}{\partial t} + \frac{\partial(\langle U_i|\Psi\rangle F)}{\partial x_i} - \left\langle \frac{S_{\mathrm{v}}}{\rho}\middle|\Psi\right\rangle F &= -\frac{\partial}{\partial \zeta}\left(\left\langle \frac{\mathrm{D}\xi}{\mathrm{D}t}\middle|\Psi\right\rangle F\right) - \frac{\partial}{\partial \eta}\left(\left\langle \frac{\mathrm{D}Y_{\mathrm{P}}}{\mathrm{D}t}\middle|\Psi\right\rangle F\right) \\
&\quad - \frac{\partial}{\partial \theta}\left(\left\langle \frac{\mathrm{D}h}{\mathrm{D}t}\middle|\Psi\right\rangle F\right).
\end{aligned} \tag{3.67}$$

On the right-hand side of the equation, the material derivative of the mixture fraction ξ, the reaction progress variable Y_{P} and the gas enthalpy h can be replaced by using

their transport equations Eqs. (3.53), (3.54) and (3.3) [149]. Thus, the final form of the PDF transport equation (3.67) reads [136, 147]

$$\begin{aligned}\frac{\partial F}{\partial t}+\frac{\partial(\langle U_i|\Psi\rangle F)}{\partial x_i} &- \left\langle \frac{S_\mathrm{v}}{\rho}\middle|\Psi\right\rangle F \\ = &- \frac{\partial}{\partial\zeta}\left(\left\langle \frac{1}{\rho}\frac{\partial}{\partial x_i}\big(\Gamma_\mathrm{M}\frac{\partial\xi}{\partial x_i}\big)+\frac{1}{\rho}(1-\xi)S_\mathrm{v}\middle|\Psi\right\rangle F\right) \\ &- \frac{\partial}{\partial\eta}\left(\left\langle \frac{1}{\rho}\frac{\partial}{\partial x_i}\big(\Gamma_\mathrm{P}\frac{\partial Y_\mathrm{P}}{\partial x_i}\big)+\frac{1}{\rho}(\dot\omega_\mathrm{P}-Y_\mathrm{P}S_\mathrm{v})\middle|\Psi\right\rangle F\right) \\ &- \frac{\partial}{\partial\theta}\left(\left\langle \frac{1}{\rho}\frac{\partial}{\partial x_i}\big(\Gamma_\mathrm{h}\frac{\partial h}{\partial x_i}\big)+\frac{1}{\rho}(S_\mathrm{e}-hS_\mathrm{v})\middle|\Psi\right\rangle F\right). \end{aligned} \tag{3.68}$$

In this equation, the terms on the left-hand side denote the temporal evolution and convective transport of PDF in physical space, as well as the changes due to spray evaporation. On the right-hand side, the terms include the probability transport in sample space due to the molecular diffusion and sink or source terms arising from either the gas-liquid interactions or chemical reactions. The conditional means in this equation are unclosed and require further modeling.

The conditional spray source terms, accounting for the inter-phase mass and energy transfers, are approximated with their unconditional averages [97]

$$\langle S_\mathrm{v}|\Psi\rangle = \langle S_\mathrm{v}\rangle + \langle S'_\mathrm{v}|\Psi\rangle \tag{3.69}$$

$$\langle S_\mathrm{e}|\Psi\rangle = \langle S_\mathrm{e}\rangle + \langle S'_\mathrm{e}|\Psi\rangle, \tag{3.70}$$

where the last terms, the fluctuations of the source terms, are neglected as first approximation. Modeling of the effects of fluctuating in spray source terms will be studied in the future work.

Decomposing the convective gas velocity $\langle U_i|\Psi\rangle$ into its Favre mean $\widetilde{U}_i$ and the fluctuating part $\langle u''_i|\Psi\rangle$, the PDF convection term on the left-hand side of Eq. (3.68) can be expressed by [25, 100]

$$\frac{\partial(\langle U_i|\Psi\rangle F)}{\partial x_i} = \frac{\partial}{\partial x_i}(\widetilde{U}_i F + \langle u''_i|\Psi\rangle F), \tag{3.71}$$

where the last term on the right-hand side is closed as [25]

$$\langle u''_i|\Psi\rangle F = -\Gamma_\mathrm{t}\frac{\partial(F/\langle\rho\rangle)}{\partial x_i}, \tag{3.72}$$

leading to

$$\frac{\partial(\langle U_i|\Psi\rangle F)}{\partial x_i} = \frac{\partial}{\partial x_i}\left(\left(\widetilde{U}_i+\frac{1}{\langle\rho\rangle}\frac{\partial\Gamma_\mathrm{t}}{\partial x_i}\right)F\right) - \frac{\partial^2}{\partial {x_i}^2}\left(\frac{\Gamma_\mathrm{t}}{\langle\rho\rangle}F\right). \tag{3.73}$$

Here, Γ_t is the turbulent transport coefficient calculated as $\Gamma_t = \mu_t/\mathrm{Sc}_t$. Note that in Eq. (3.72) the gradient-diffusion hypothesis [25] has been used to model the conditional turbulent scalar flux.

Additionally, the molecular mixing terms in Eq. (3.68), i.e. the first term in each sample space, represent the transport of the PDF by the mechanism of molecular diffusion, and they are length-scale dependent, so requiring multipoint information. The PDF transport equations are, however, formulated for one-point one-time statistics, so the mixing models need to account for the effects of molecular diffusion, which will be further discussed in the next subsection.

3.3.3 Modeling of Micro-Mixing

As described in the last section, models are required for closing the specific open terms in PDF transport equation. The molecular scalar mixing terms appearing in either joint scalar PDF or joint velocity-scalar PDF transport equations describe the effects of micro-mixing process, which is an important mechanism especially in turbulent reacting flows where the chemical reactions can occur only after the mixing of reactive species by molecular diffusion at small scales. Modeling of micro-mixing in the transported joint PDF approach is discussed in this subsection.

Interaction-by-exchange-with-the-mean (IEM)

The interaction-by-exchange-with-the-mean (IEM) [150], also known as linear mean-square estimation (LMSE) [83], is one of the most widely used mixing models because of its simplicity and ability of representing the correct variance decay rate. This model assumes a linear relaxation of all scalar values to the local mean, and the corresponding unclosed micro-mixing term is modeled as [150]

$$\left\langle \frac{1}{\rho}\frac{\partial}{\partial x_i}\left(\Gamma_\Phi \frac{\partial \Phi}{\partial x_i}\right) \middle| \Psi \right\rangle = -\frac{1}{2}\omega_\phi(\Phi - \langle\Phi\rangle). \tag{3.74}$$

Here, ω_ϕ is the scalar mixing frequency and characterizes the time scale of mixing process. With the assumption that the time and length scales of scalar and large-scale turbulence are proportional, ω_ϕ can be calculated with [25]

$$\omega_\phi = C_\phi \omega_t, \tag{3.75}$$

where the turbulence mixing frequency ω_t is determined by

$$\omega_t = \epsilon/k, \tag{3.76}$$

and the model parameter C_ϕ is the mechanical-to-scalar time scale ratio with standard value 2.0 [25]. In the frame of Monte-Carlo PDF methods with a system of notional gas

particles, according to Eq. (3.74) the scalar values of each particle will relax towards their local mean at a constant rate of $2/\omega_\phi$ and change essentially independently of the associated values of other particles.

Modified Curl Model

The modified Curl model [151], based on Curl's coalescence dispersion model [152], is a direct particle-interaction model. In this model, the molecular diffusion is simulated by the stochastic interaction between gas particles. At each mixing event, particle pairs, denoted as i and j, are randomly selected from the set of particles present in each computational cell, and change their scalar values to their averaged mean by [151]

$$\Phi^{(i)}(t+\Delta t) = \Phi^{(i)}(t) + \frac{1}{2}a\big(\Phi^{(j)}(t) - \Phi^{(i)}(t)\big) \tag{3.77}$$

$$\Phi^{(j)}(t+\Delta t) = \Phi^{(j)}(t) + \frac{1}{2}a\big(\Phi^{(i)}(t) - \Phi^{(j)}(t)\big), \tag{3.78}$$

where the extent of mixing is determined by the parameter a, which is randomly chosen from a uniform distribution in (0,1). The number of particle pairs participating in each mixing step is determined by $N_{mix} = 2N\omega_\phi\Delta t$, where N is the total particle number in the cell.

This particle-pair interaction model shows the easy integration into a stochastic particle framework as applied in transported PDF simulations. Similar to the IEM model, modified Curl model does not relax to the Gaussian distribution in a homogeneous turbulence.

Euclidean Minimum Spanning Tree (EMST)

The EMST model [153] is another important mixing model used in the transported PDF calculations. It is also a particle interaction mixing model that mixing is represented by interactions between pairs of selected particles, while in this method, particles are determined by an age property to be in the mixng or non-mixing subset. At each given time, the particles only at the mixing state will participate in the mixng processes and interact along the edges of a contructed Euclidean minimum spanning tree, which is used to ensure the localness of mixing processes. The neighboring particles contected in one branch of the tree mix over time as [153, 154]

$$\Phi^{(i)}(t+\Delta t) = \Phi^{(i)}(t) + bB_n\Delta t\big(\Phi^{(j)}(t) - \Phi^{(i)}(t)\big) \tag{3.79}$$

$$\Phi^{(j)}(t+\Delta t) = \Phi^{(j)}(t) + bB_n\Delta t\big(\Phi^{(i)}(t) - \Phi^{(j)}(t)\big), \tag{3.80}$$

where b is a coefficient determined to ensure the desired mixing frequency, and B_n is defined based on the position of the branch in the tree. This model focuses on

the localness preservation of mixing in composition space, but it is not sufficient for guaranting physically realistic prediction [155].

Other Mixing Models

Several other mixing models have been proposed in the past, for example, the Mapping closure model [156], Fokker-Planck closure model [157], Langevin mixing model [158] and parameterized scalar profile (PSP) model [159]. Specific, PSP model is proposed recently by Meyer et al. [159] and shows a promising extension of the IEM model. In IEM model, in each cell all particles follow a deterministic relaxation towards their average value at the same rate ω_ϕ (see Eq. (3.74)), and in the parameterized scalar profile (PSP) model, each particle is prescribed with a specified one-dimensional scalar profile using three additional parameters, where the individual length scale and profile boundaries are determined. More description of the predictive capabilities of various mixing models can be found in Refs. [48, 160]

In this thesis, the extended IEM model with additional terms $S_{l,\Phi}$ accounting for the spray evaporation effects [84], is used for describing the micro-mixing in the turbulent spray flows. The evolution of scalar Φ is then described by the extended IEM model [84]

$$\frac{\mathrm{d}\Phi}{\mathrm{d}t} = -\frac{1}{2}C_\phi\omega_\mathrm{t}(\Phi - \langle\Phi\rangle) + S_{l,\Phi}. \tag{3.81}$$

Humza et al. [149] studied the extended modified Curl model for the simulation of a methanol/air turbulent spray flame, where the modified Curl model shows somewhat better performance than IEM model; however, due to the underestimation of the experimental data by both models, a final conclusion about the performance of the mixing models cannot yet be drawn. A better conclusion may be obtained when applying these two models to the simulation of different turbulent spray flames.

For the spray flames, to account for the effects of spray evaporation on the local scalar mixing, the scalar dissipation rate $\widetilde{\chi}$ calculated based on the transport equation is proposed as [161]

$$\begin{aligned}\frac{\partial\langle\rho\rangle\widetilde{\chi}}{\partial t} + \frac{\partial}{\partial x_i}\left(\langle\rho\rangle\widetilde{u}_i\widetilde{\chi} - \Gamma_\chi\frac{\partial\widetilde{\chi}}{\partial x_i}\right) &= \alpha_P\frac{\mu_\mathrm{t}}{Sc_\mathrm{t}}\frac{\widetilde{\chi}}{\widetilde{\xi''^2}}\left(\frac{\partial\widetilde{\xi}}{\partial x_i}\right)^2 + \beta_P\frac{\widetilde{\chi}}{k}\left(G_k - \frac{2}{3}\langle\rho\rangle k\frac{\partial\widetilde{u}_j}{\partial x_j}\right)\\ &\quad - \alpha_D\langle\rho\rangle\frac{\epsilon\widetilde{\chi}}{k} - \beta_D\langle\rho\rangle\frac{\widetilde{\chi}^2}{\widetilde{\xi''^2}}\\ &\quad + \lambda_1\frac{\widetilde{\chi}}{\widetilde{\xi''^2}}S_{\widetilde{\xi''^2}} + \lambda_2\frac{\widetilde{\chi}}{\epsilon}S_\epsilon + (1-\lambda_1-\lambda_2)\widetilde{\chi}S_\mathrm{v}.\end{aligned} \tag{3.82}$$

Here, the model constants are $\alpha_P = 2.0$, $\beta_P = 0.72$, $\alpha_D = 0.96$, $\beta_D = 2.0$, and $\lambda_1 = 1.0$, $\lambda_2 = 0.5$ [161]. The last three terms on the right hand side of this equation denote the

effects of spray evaporation, and include the spray source terms S_{v}, $S_{\widetilde{\xi''^2}}$, and S_ϵ for density, mixture fraction variance $\widetilde{\xi''^2}$ and dissipation rate ϵ, respectively.

3.4 Liquid Phase

The dynamics of liquid phase are described in Lagrangian coordinates, and the stochastic Lagrangian equations for the droplet motion, evaporation and heating are solved and given here.The dilute spray is assumed with negligible droplet-droplet interactions. Spherically symmetric and single-component droplets are considered.

3.4.1 Droplet Motion

In the most general case, the equation of motion for the spherical droplets in a turbulent flow is govened by [162, 163]

$$m_{\mathrm{d}}\frac{\mathrm{d}\mathbf{V}_{\mathrm{d}}}{\mathrm{d}t} = F_{\mathrm{D}} + F_{\mathrm{g}} + F_{\mathrm{p}} + F_{\mathrm{a}} + F_{\mathrm{B}}, \tag{3.83}$$

where $\mathbf{V}_{\mathrm{d}}$ and m_{d} are the velocity and mass of each droplet. Following Newton's second law, this equation describes the balance of forces acting on a droplet that moves through the fluid. The left-hand side is the mass of a droplet, multiplied by its acceleration. The terms on the right-hand side represent the contributions for the droplet acceleration; they include Stokes drag force F_{D}, gravity F_{g}, the force due to pressure gradient F_{p}, added mass effect F_{a}, and Basset history term F_{B}. Under the assumption that the density of the fuel liquid is much larger than that of the carrier gas, $\rho_l \gg \rho$, the only forces that have a significant contribution for the droplets motion are the drag force F_{D} and gravitation F_{g}; all others have negligible effects [18, 163, 164]. The equation of droplet motion is then simplified to [18, 145, 163]

$$\frac{\mathrm{d}\mathbf{V}_{\mathrm{d}}}{\mathrm{d}t} = \frac{3}{8}\frac{1}{r_{\mathrm{d}}}\frac{\rho}{\rho_l}C_D(\mathbf{U}-\mathbf{V}_{\mathrm{d}})|\mathbf{U}-\mathbf{V}_{\mathrm{d}}| + \mathbf{g}, \tag{3.84}$$

and the droplet position $\mathbf{x}_{\mathrm{d}}$ can be obtained by solving

$$\frac{\mathrm{d}\mathbf{x}_{\mathrm{d}}}{\mathrm{d}t} = \mathbf{V}_{\mathrm{d}}. \tag{3.85}$$

In Eq. (3.84), r_{d} is the droplet radius, and $\mathbf{g}$ is the acceleration of gravity. The drag coefficient C_D characterizes the complex inter-dependence between the dispersed droplets and carrier turbulent flows, and it is usually expressed by the Schiller-Naumann correlation [165]

$$C_D = \begin{cases} \frac{24}{\mathrm{Re_d}}\left(1 + 0.15\ \mathrm{Re_d}^{0.687}\right) & \text{if } \mathrm{Re_d} \le 10^3 \\ 0.44 & \text{if } \mathrm{Re_d} > 10^3, \end{cases} \tag{3.86}$$

where the droplet Reynolds number $\mathrm{Re_d}$ defines the gas flow characteristics around droplets, and it is calculated as [18, 165]

$$\mathrm{Re_d} = \frac{2r_\mathrm{d}\rho|\mathbf{U} - \mathbf{V}_\mathrm{d}|}{\mu_\mathrm{g}}. \tag{3.87}$$

μ_g is the viscosity of surrounding gas, and $\mathbf{U} = \widetilde{\mathbf{U}} + \mathbf{u}''$ is the instantaneous gas velocity sampled along the droplet trajectory, where the mean gas velocity $\widetilde{\mathbf{U}}$ is interpolated from the calculated mean gas velocity at the surrounding grid points, and $\mathbf{u}''$ is the fluctuating part, which is modeled with the one-step Langevin equation model (LEM) described by Lain and Sommerfeld [166]. This model is based on the correlation between the fluid and particle trajectories. The time and spatial correlation denoted by the Eulerian $R_{L,i}$ and Lagrangian $R_{E,i}$ expressions are combined to give a relation for the fluctuating velocities at two successive time steps as [166, 167]

$$u_i''(t_{n+1}) = R_{P,i}(\Delta t, \Delta r)u_i''(t_n) + \sigma\chi_i\sqrt{1 - R_{P,i}^2(\Delta t, \Delta r)}. \tag{3.88}$$

$R_{P,i}$ is the correlation function, which is given as the product of the Lagrangian and Eulerian part [166, 167]

$$R_{P,i}(\Delta t, \Delta r) = R_{L,i}(\Delta t)R_{E,i}(\Delta r), \tag{3.89}$$

and χ_i is a Gaussian random number with mean value zero and a standard deviation of unity. An exponential form is used to define the Lagrangian correlation function $R_{L,i}$ [166, 167]

$$R_{L,i}(\Delta t) = \exp(-\frac{\Delta t}{T_L}), \tag{3.90}$$

and the Lagrangian integral time scale is computed as $T_L = C_T\sigma^2/\epsilon$ with $\sigma^2 = 2k/3$ and $C_T = 0.24$ [18]. The Eulerian part can be expressed as function of longitudinal and transversal correlation coefficients, $f(\Delta r)$ and $g(\Delta r)$ as [166, 167]

$$R_{E,i}(\Delta r) = \{f(\Delta r) - g(\Delta r)\}\frac{\Delta r_i \Delta r_j}{\Delta r^2} + g(\Delta r)\delta_{ij}, \tag{3.91}$$

where

$$f(\Delta r) = \exp(-\frac{\Delta r}{L_E}) \tag{3.92}$$

$$g(\Delta r) = (1 - \frac{\Delta r}{2L_E})\exp(-\frac{\Delta r}{L_E}). \tag{3.93}$$

Here, $\Delta r = |\mathbf{U} - \mathbf{V}_d|\Delta t$ is the separation distance between the fluid element and the droplet, and the integral length scale is calculated as $L_E = 3.0T_L\sigma$.

3.4.2 Droplet Evaporation

The mass coupling between gas and liquid phases is due to the fact that additional fuel vapor enters the gas phase through spray evaporation. In the spray combustion, this evaporation process usually has a direct effect on the combustion rate since chemical reaction occurs only after the mixing of vaporized fuels and air in the appropriate combustible ratio. Thus, the combustion efficiency is influenced by the evaporation rate. For proper modeling of droplet evaporation, different mathematical models have been studied [168–172].

As described in the work of Sirignano [170], depending on the transport properties inside the droplets, different liquid phase models can be classified in six groups: (1) model based on the assumption that the temperature at droplet surface is uniform and constant (often referred to d^2 law model); (2) infinite conductivity model, where droplet temperature is spatially uniform and varies with time; (3) conduction limit model (the finite thermal conductivity is taken into account, but the recirculation inside the droplet is not considered); (4) effective conductivity model (accounts for both the finite thermal conductivity and the recirculation inside the droplet); (5) vortex model describing the recirculation inside droplet in terms of vortex dynamics; (6) model based on the full solution of the Navier-Stokes equation. Among these models, groups (2), (3) and (4) are often applied in most practical simulations of turbulent evaporating spray flows due to their relatively good performance and computational efficiency [170, 172, 173].

Abramzon and Sirignano [174] refined the infinite conductivity model to take into account the convective effects on heat and mass transfer at droplet surface, which is considered through use of the modified Nusselt number and Sherwood number. Miller et al. [175] studied the performance of some existing evaporation models, where the simulations with the equilibrium and non-equilibrium models are conducted for different droplet-laden flows. The results with non-equilibrium models show most favorable agreement with a wide range of experimental data.

In the present work, the droplet evaporation rate in a convective flow field is described by the Abramzon-Sirignano model [174]

$$\frac{\mathrm{d}m_\mathrm{d}}{\mathrm{d}t} = \dot{m}_\mathrm{d} = 2\pi r_\mathrm{d} \hat{\rho} \hat{D} \widetilde{\mathrm{Sh}} \ln(1 + B_\mathrm{M}), \tag{3.94}$$

where $\hat{D}$ is the binary diffusion coefficient, evaluated in the gas film using the "1/3-rule" [176]. The Spalding mass transfer number B_M, is evaluated based on the vapor mass fraction in the gas phase far from the droplet, Y_∞, and mass fraction of fuel vapor at the droplet surface, $Y_{F\mathrm{s}}$ [85, 174]

$$B_\mathrm{M} = \frac{Y_{F\mathrm{s}} - Y_\infty}{1 - Y_{F\mathrm{s}}}, \tag{3.95}$$

and

$$Y_{Fs} = \frac{X_{Fs}}{W_\mathrm{g}/W_\mathrm{v} + (1 - W_\mathrm{g}/W_\mathrm{v})X_{Fs}}. \tag{3.96}$$

Here, W_v and W_g are the molecular weight of vapor fuel and the gas surrounding the droplet, respectively. Based on the Langmuir-Knudsen law [177], the thermodynamic non-equilibrium effect is considered in the calculation of the surface mole fraction, X_{Fs} [175]

$$X_{Fs} = \frac{P_\mathrm{atm}}{P_\mathrm{g}} \exp\left[\frac{L_V(T_\mathrm{d})}{R/W_\mathrm{v}}\left(\frac{1}{T_\mathrm{b}} - \frac{1}{T_\mathrm{d}}\right)\right] - \beta\left(\frac{L_K}{r_\mathrm{d}}\right), \tag{3.97}$$

where R is the universal gas constant and T_b the droplet boiling point. $L_V(T_\mathrm{d})$ is the droplet temperature T_d dependent latent heat of vaporization. P_atm and P_g are the standard atmospheric pressure and the gas pressure, respectively. The Knudsen layer thickness, L_K, and the non-dimensional evaporation parameter, β, are given with the following expression [175]

$$L_K = \frac{\mu_\mathrm{g}\sqrt{2\,\pi T_\mathrm{d}\,R/W_\mathrm{v}}}{P_\mathrm{g}\mathrm{Sc_g}}, \quad \beta = 1.5\ \mathrm{Pr_g}\,\tau_\mathrm{d}\,\frac{\dot{m}_\mathrm{d}}{m_\mathrm{d}}. \tag{3.98}$$

3.4.3 Droplet Heating

Considering a uniform temperature distribution within the droplet, the infinite conductivity model, including the non-equilibrium effects at the droplet surface, is used for the description of droplet heat transfer [175]

$$\frac{\mathrm{d}T_\mathrm{d}}{\mathrm{d}t} = \frac{f_2\ \widetilde{\mathrm{Nu}}}{3\ \mathrm{Pr_g}}\frac{1}{\tau_\mathrm{d}}\left(\frac{C_{p,\mathrm{g}}}{C_{p,l}}\right)(T_\mathrm{g} - T_\mathrm{d}) - \frac{L_V(T_\mathrm{d})}{C_{p,l}}\left(\frac{\dot{m}_\mathrm{d}}{m_\mathrm{d}}\right). \tag{3.99}$$

Here, $\tau_\mathrm{d} = 2/9\rho_l {r_\mathrm{d}}^2/\mu_\mathrm{g}$ is the droplet relaxation time. $C_{p,\mathrm{g}}$ and $C_{p,l}$ are the heat capacity at constant pressure for the gas and liquid phase, respectively, and $L_V(T_\mathrm{d})$ the droplet temperature dependent latent heat of vaporization. The parameter f_2 is a correction factor for the interphase thermal transfer due to the spray evaporation and is defined as [175]

$$f_2 = \frac{\beta}{e^\beta - 1}. \tag{3.100}$$

Following the work of Abramzon and Sirignano [174], the modified $\widetilde{\mathrm{Nu}}$ and Sherwood $\widetilde{\mathrm{Sh}}$ numbers in Eqs. (3.94) and (3.99) are used to account for the blowing effect on the droplet evaporation [174]

$$\begin{aligned}\widetilde{\mathrm{Nu}} &= 2(1 + 0.276\frac{{\mathrm{Re_d}}^{1/2}{\mathrm{Pr_g}}^{1/3}}{F(B_\mathrm{T})}) \\ \widetilde{\mathrm{Sh}} &= 2(1 + 0.276\frac{{\mathrm{Re_d}}^{1/2}{\mathrm{Sc_g}}^{1/3}}{F(B_\mathrm{M})}),\end{aligned} \tag{3.101}$$

with

$$F(B) = \frac{(1+B)^{0.7}}{B}\ln(1+B)$$
$$\mathrm{Pr_g} = \frac{\mu_\mathrm{g} C_{p,\mathrm{g}}}{\lambda_\mathrm{g}} \text{ and } \mathrm{Sc_g} = \frac{\mu_\mathrm{g}}{\rho_\mathrm{g} D}. \tag{3.102}$$

In Eq. (3.102), B stands for either the mass or the heat transfer number, $B_\mathrm{T} = (1 + B_\mathrm{M})^\phi - 1$ and $\phi = (1/\mathrm{Le})(C_{p,l}/C_{p,\mathrm{g}})(\widetilde{\mathrm{Sh}}/\widetilde{\mathrm{Nu}})$ [174], and λ_g is the thermal conductivity. Here the unmodified Nusselt and Sherwood numbers are evaluated based on the model of Ranz and Marshall [178, 179].

3.5 Spray Source Terms

The solution of the droplet equations (3.84), (3.94) and (3.99) allows evaluation of the spray source terms in the gas-phase governing equations to account for the interphase exchange due to spray evaporation. The concrete formulation of spray source terms appearing in the gaseous phase for the mass S_v, momentum S_m, energy S_e and the turbulent kinetic energy S_k are given as [79, 95]

$$S_\mathrm{v} = \sum_{k=1}^{n_\mathrm{d}} N_{\mathrm{d},k}\dot{m}_{\mathrm{d},k} \tag{3.103}$$

$$S_\mathrm{m} = \sum_{k=1}^{n_\mathrm{d}} N_{\mathrm{d},k}\left[-m_{\mathrm{d},k}\frac{\mathrm{d}\mathbf{V}_{\mathrm{d},k}}{\mathrm{d}t} + \mathbf{V}_{\mathrm{d},k}\dot{m}_{\mathrm{d},k}\right] \tag{3.104}$$

$$S_\mathrm{e} = \sum_{k=1}^{n_\mathrm{d}} N_{\mathrm{d},k}\left[-\frac{\mathrm{d}}{\mathrm{d}t}(m_{\mathrm{d},k}C_{pl}T_{\mathrm{d},k}) - \frac{1}{2}\frac{\mathrm{d}}{\mathrm{d}t}(m_{\mathrm{d},k}\mathbf{V}_{\mathrm{d},k}^2)\right] \tag{3.105}$$

$$S_k = \sum_{k=1}^{n_\mathrm{d}} N_{\mathrm{d},k}\mathbf{u}''\dot{m}_{\mathrm{d},k}\mathbf{V}_{\mathrm{d},k}, \tag{3.106}$$

where n_d is the number of droplet parcels present in the considered volume, the droplet groupings are used, and $N_{\mathrm{d},k}$ corresponds to the number of real droplets in one computational parcel k [18]. The corresponding spray source terms $S_{\widetilde{\xi''^2}}$ and S_ϵ for the mixture fraction variance $\widetilde{\xi''^2}$ and dissipation rate of the turbulent kinetic energy ϵ read $S_\mathrm{v}\widetilde{\xi''^2}(1-2\,\widetilde{\xi})\widetilde{\xi}$ and $c_s\epsilon/kS_k$ [79, 95], respectively, and the model constant $c_s = 1.5$ [79].

The following chapter introduces the numerical methods used for both the gas and liquid phases, as well as their boundary conditions.

4. Numerical Solution

The numerical scheme for the gas phase is based on a hybrid Eulerian finite-volume and Lagrangian Monte-Carlo method, which includes a Lagrangian Monte-Carlo particle method for solving the high-dimensional joint PDF transport equation, coupled with an Eulerian finite volume method, providing the necessary information of the turbulence time scale, and the mean pressure or velocity field. For the liquid phase, a Lagrangian discrete parcel method is used to simulate the spray dynamics with a point-source approximation [180].

4.1 Finite Volume Method

The finite volume method is one of the most widely used numerical methods for the approximate solution of partial differential equations. This method is based on the solution of the continuous gas-phase governing equations in their integral form over the control volume, which is given by [80]

$$\int_V \frac{\partial(\rho\Phi)}{\partial t}\mathrm{d}V + \int_V \frac{\partial(\rho U_i\Phi)}{\partial x_i}\mathrm{d}V = \int_V \frac{\partial}{\partial x_i}\left(\Gamma_\Phi \frac{\partial\Phi}{\partial x_i}\right)\mathrm{d}V + \int_V S_\Phi \mathrm{d}V. \tag{4.1}$$

Here, Φ represents a conserved quantity of the gas density ($\Phi = 1$), velocity component ($\Phi = U_j$) or the scalars ($\Phi = Y_\alpha$, h), etc., and S_Φ is the corresponding source term. Considering a steady-state case, and applying the Gauß's divergence theorem, the above equation can be rewritten as [80]

$$\int_A n_i\left(\rho U_i\Phi - \Gamma_\Phi \frac{\partial\Phi}{\partial x_i}\right)\mathrm{d}A = \int_V S_\Phi \mathrm{d}V, \tag{4.2}$$

where A is the surface area of the considered volume cell V, and n_i is the outward pointing unit vector normal to the surface A at the i^{th}- direction. Here, the Einstein summation convention applies over the repeated index i. From the equation (4.2), the physical meaning of finite volume method is clear; fluxes of the quantity flowing through the surface of a control volume are balanced by the generation or consumption of Φ.

In this work, the gas-phase conservation equations are solved with a CFD solver based on the finite-volume method, where the SIMPLE (Semi-Implicit Method for

Pressure-Linked Equation) algorithm [181, 182] is employed for the pressure-velocity coupling. The general form of the governing equations for a steady, two-dimensional, axisymmetric flow, considering the two-phase exchange effects, can be written as [79, 110]

$$\frac{\partial(\tilde{\rho}\tilde{U}_i\tilde{\Phi})}{\partial x_i} - \frac{\partial}{\partial x_i}\left(\Gamma_\Phi \frac{\partial\tilde{\Phi}}{\partial x_i}\right) = S_{\mathrm{g},\Phi} + S_{l,\Phi}. \tag{4.3}$$

Here, $S_{\mathrm{g},\Phi}$ denotes the gas phase source term (see Eqs. (3.35)-(3.37)), and $S_{l,\Phi}$ represents additional source terms associated with the interactions of the gas and the liquid phase (see Eqs. (3.103)-(3.106)).

After integration of governing equations (4.3) over the control volume following Eq. (4.2), the algebraic discretized equations would be obtained, where the flow field variables are evaluated on some discrete points in each volume cell, and they are interpreted as the average value over the finite volume. The numerical results are then determined by solving the discretized formulations with a specific solution algorithm, which will be described in the following subsections.

4.1.1 Discretized Equations

First, the governing equations are discretized spatially, dividing the computational domain with discrete meshes. A sketch of the two-dimensional structured finite-volume mesh used for discretization is depicted in Fig. 4.1. A control volume around the central nodal point P is identified, which has a width of $(\Delta x \times \Delta y)$, and where there are four neighbours in x and y direction, denoted as E, W and N, S, respectively. The boundaries or faces of the control volume are located at the mid-way between adjacent nodes, and are indicated by e, w, n and s for the east, west, north and south sides, accordingly. Based on the control volume defined above, the discretized formulation of equation (4.3) may be written as [181, 183]

$$a_P\Phi_P = a_N\Phi_N + a_S\Phi_S + a_E\Phi_E + a_W\Phi_W + b, \tag{4.4}$$

with

$$\begin{aligned}
a_N &= D_n A(|P_{\Delta n}|) + [[-F_n, 0]] \\
a_S &= D_s A(|P_{\Delta s}|) + [[F_s, 0]] \\
a_E &= D_e A(|P_{\Delta e}|) + [[-F_e, 0]] \\
a_W &= D_w A(|P_{\Delta w}|) + [[F_w, 0]] \\
a_P &= a_N + a_S + a_E + a_W + S_\mathrm{v}\Delta x\Delta y \\
b &= (S_{\mathrm{g},\Phi} + S_{l,\Phi})\Delta x\Delta y.
\end{aligned} \tag{4.5}$$

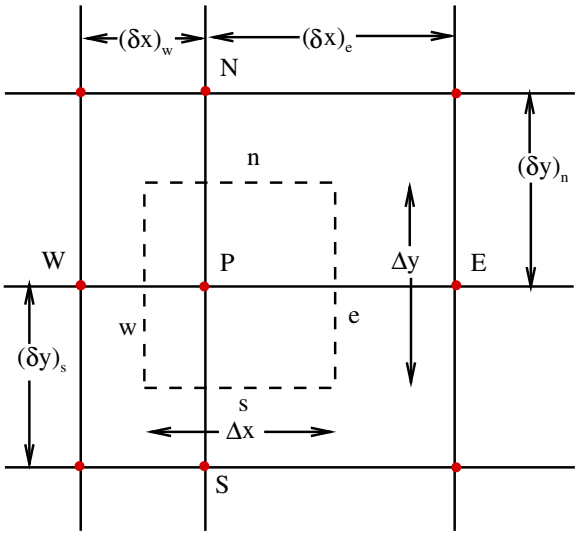

Figure 4.1: A sketch of the two-dimensional finite-volume mesh [110].

It can be noted that the source terms accounting for the inter-phase exchange effects appear to be included in the coefficient of a_P and b. Here, the diffusion coefficient D_l and convective mass flux F_l at cell faces are given as [181, 183]

$$D_l = \frac{\Gamma_l \Delta y}{(\delta x)_l}, \quad F_l = (\tilde{\rho}\tilde{U})_l \Delta y, \quad l = e, w \tag{4.6}$$

$$D_l = \frac{\Gamma_l \Delta x}{(\delta y)_l}, \quad F_l = (\tilde{\rho}\tilde{V})_l \Delta x, \quad l = n, s, \tag{4.7}$$

where the symbol $[[a_1, a_2]]$=max(a_1, a_2), and $P_{\Delta l}$ is the Peclet number, which is defined by [181, 183]

$$P_{\Delta l} = \frac{F_l}{D_l}. \tag{4.8}$$

For the numerical scheme of upwind differencing and central differencing, used in this work for evaluation of the cell face values F_l and D_l, the function $A(|P_{\Delta n}|)$ takes the value of unity.

The governing equations for the gas scalar properties are solved following the aforementioned discretization procedure, while the solution of the gas velocity requires special treatment due to the direct pressure-velocity coupling through the pressure source terms appeared in the momentum equations. To avoid the unphysical behavior of the discretized momentum equation for spatially oscillating pressures, e.g., the zigzag type of distribution [184], a staggered grid technique [185] is adopted, where values of the gas velocity differing from scalar quantities, including pressure, are stored at the grid

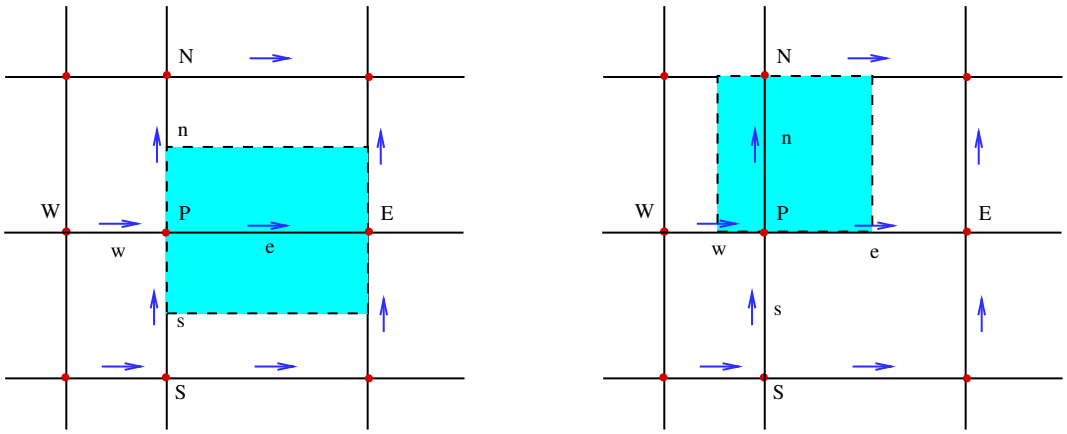

Figure 4.2: The control volume of (a): axial velocity and (b): radial velocity [110].

cells. As illustrated in Fig. 4.2, the control volume of velocity is defined at the (scalar) cell faces. Horizontal arrows denote the locations for axial U-velocity and vertical ones indicate the radial V-velocity. Employing the staggered grids, the discretized equation of gas velocity, U_e and V_n can be written as [80]

$$a_e U_e = \sum a_l U_l + b + (p_P - p_E)\Delta y \tag{4.9}$$

$$a_n V_n = \sum a_l U_l + b + (p_P - p_N)\Delta x, \tag{4.10}$$

where, similar to Eq. (4.4), the coefficient a_l has taken into account of both diffusion and convection influences from neighbouring nodes, and b represents the corresponding source term (4.5). p_P, p_E and p_N are the pressure values at the nodes P, E, N, respectively, which shows another advantage of staggered grids, namely that the pressure value used in the discretized momentum equations is obtained from the pressure field solved at the (scalar) grid nodes and no interpolation is needed. Vice versa, in Eq. (4.7) the velocity value at the cell faces is determined directly from the solved velocity field at the staggered grids.

In addition, a pressure correction technique based on the SIMPLE algorithm is adopted to solve for the pressure-velocity coupling. This algorithm is basically an iterative solution approach [181]. A guessed pressure field starts the iterative process, and is used to solve the momentum equation and to obtain an initial guessed velocity field. Then, a pressure correction p' is determined from a pressure correction equation, which is then used to update the 'corrected' velocity and the pressure field. The iteration proceeds till the convergence of velocity and pressure is achieved. With the basic idea that the correct velocity field should satisfy the continuity equation, the

pressure correction formula for p' can be obtained as [184]

$$a_P p'_P = a_N p'_N + a_S p'_S + a_E p'_E + a_W p'_W + b, \tag{4.11}$$

and

$$\begin{aligned} a_E &= (\tilde{\rho}d)_e \Delta y,\ a_W = (\tilde{\rho}d)_w \Delta y,\ a_N = (\tilde{\rho}d)_n \Delta x,\ a_S = (\tilde{\rho}d)_s \Delta x \\ b &= [(\tilde{\rho}\tilde{U}^*)_w - (\tilde{\rho}\tilde{U}^*)_e]\Delta y + [(\tilde{\rho}\tilde{U}^*)_s - (\tilde{\rho}\tilde{U}^*)_n]\Delta x + S_{\mathrm{v}} \Delta x \Delta y \\ a_P &= \sum_l a_l,\ \ l = E, W, N, S \\ d_l &= \Delta y / a_l,\ \ l = e, w, \quad d_l = \Delta x / a_l,\ \ l = n, s. \end{aligned} \tag{4.12}$$

Given the discretized formula for the system of gas governing equations, a proper solution algorithm is needed to solve the resulting linear algebraic equations.

4.1.2 Solution Algorithm

In this work, the Thomas algorithm or the so-called tridiagonal matrix algorithm (TDMA) [186] is used to solve the discretized algebraic equations. In this algorithm, for multi-dimensional problems, a direct Gaußian elimination method is applied to each direction iteratively. The discretized equations (4.4), (4.10) and (4.11) can be rewritten in a general form as [80, 186]

$$a_i \Phi_{i-1} + b_i \Phi_i + c_i \Phi_{i+1} = d_i, \tag{4.13}$$

with Φ_{i-1}, Φ_i and Φ_{i+1} being the three neighbor node values in one direction. The corresponding tridiagonal form then gives [80, 186]

$$\begin{bmatrix} b_1 & c_1 & & & \\ a_2 & b_2 & c_2 & & \\ & \ddots & \ddots & \ddots & \\ & & a_{N-1} & b_{N-1} & c_{N-1} \\ & & & a_N & c_N \end{bmatrix} \begin{bmatrix} \Phi_1 \\ \Phi_2 \\ \vdots \\ \Phi_{N-1} \\ \Phi_N \end{bmatrix} = \begin{bmatrix} d_1 \\ d_2 \\ \vdots \\ d_{N-1} \\ d_N \end{bmatrix}$$

The solution procedure consists of two parts: forward elimination and back substitution. For $i = 1$, the equation can be rewritten as

$$\Phi_1 = -\frac{c_1}{b_1}\Phi_2 + \frac{d_1}{b_1} = P_1 \Phi_2 + Q_1, \tag{4.14}$$

inserting Eq. (4.14) into equation ($i = 2$), and eliminating Φ_1, yields

$$\Phi_2 = \frac{-c_2}{a_2 P_1 + b_2}\Phi_3 + \frac{d_2 - a_2 Q_1}{a_2 P_1 + b_2} = P_2 \Phi_3 + Q_2. \tag{4.15}$$

Following the same elimination procedure, the general formula for relating Φ_i and Φ_{i+1} gives

$$\Phi_i = \frac{-c_i}{a_i P_{i-1} + b_i}\Phi_{i+1} + \frac{d_i - a_i Q_{i-1}}{a_i P_{i-1} + b_i} = P_i \Phi_{i+1} + Q_i, \tag{4.16}$$

with

$$P_i = \frac{-c_i}{a_i P_{i-1} + b_i}, \quad Q_i = \frac{d_i - a_i Q_{i-1}}{a_i P_{i-1} + b_i}, \tag{4.17}$$

For $i = N$, specifically, the relation obtained is

$$P_N = 0, \quad Q_N = \frac{d_N - a_N Q_{N-1}}{a_N P_{N-1} + b_N} = \Phi_N, \tag{4.18}$$

and, starting from Eq. (4.18), the back substitution is applied to calculate the Φ_i ($i = N-1, N-2, ..., 2, 1$).

To finish one iteration, the above elimination and substitution processes are performed in order to solve the node variables for the lines in one direction, and repeated for the lines in other directions.

4.2 Stochastic Lagrangian Particle Method

4.2.1 Lagrangian Monte-Carlo Solution of PDF Transport Equations

The equations for the transported joint PDF, derived in the last chapter (3.3.2), show a high dimensionality in both physical and scalar sample spaces, which makes the traditional discretization solution, such as finite-difference or finite-volume method, impractical. A Monte-Carlo method, using a Lagrangian trajectory tracking [25], is used. The gas flow is discretized in terms of flow mass into a large number of stochastic notional gas particles. The joint PDF transport equation is then transformed into a set of stochastic differential equations (SDEs), which provides the evolution of each particle and its properties. For the joint scalar (mixture fraction, reaction progress variable, and gas ethalpy) PDF transport equation (3.68), the set of SDEs are given as [136, 147]

$$x_i^*(t + \mathrm{d}t) = x_i^*(t) + \left(\widetilde{U}_i + \frac{1}{\langle\rho\rangle}\frac{\partial \Gamma_\mathrm{t}}{\partial x_i}\right)\mathrm{d}t + (\frac{2}{\langle\rho\rangle}\Gamma_\mathrm{t})^{1/2}\mathrm{d}W_i \tag{4.19}$$

$$\xi^*(t + \mathrm{d}t) = \xi^*(t) + \left(-\frac{1}{2}C_\phi\omega_\mathrm{t}(\xi^* - \langle\xi\rangle) + (1 - \langle\xi\rangle)\frac{\langle S_\mathrm{v}\rangle}{\langle\rho\rangle}\right)\mathrm{d}t \tag{4.20}$$

$$Y_\mathrm{P}^*(t + \mathrm{d}t) = Y_\mathrm{P}^*(t) + \left(-\frac{1}{2}C_\phi\omega_\mathrm{t}(Y_\mathrm{P}^* - \langle Y_\mathrm{P}\rangle) + \frac{1}{\langle\rho\rangle}(\langle\dot{\omega}_\mathrm{P}\rangle - \langle Y_\mathrm{P}\rangle\langle S_\mathrm{v}\rangle)\right)\mathrm{d}t \tag{4.21}$$

$$h^*(t + \mathrm{d}t) = h^*(t) + \left(-\frac{1}{2}C_\phi\omega_\mathrm{t}(h^* - \langle h\rangle) + \frac{1}{\langle\rho\rangle}(\langle S_\mathrm{e}\rangle - \langle h\rangle\langle S_\mathrm{v}\rangle)\right)\mathrm{d}t. \tag{4.22}$$

Here, the superscript $*$ denotes the Lagrangian particle properties, and Eqs. (4.19) - (4.22) give the stochastic evolution of gas particles' position x^*, mixture fraction ξ^*, reaction progress variable Y_{P}^* and enthalpy h^*, which is linked to the evolution of joint PDF in physical-scalar space by a correspondence between SDEs and the Fokker-Planck equation [30].

In Eq. (4.19), $\mathrm{d}W_i$ is the increment of a stochastic Wiener process, which follows a Gaußian distribution with the mean $\langle dW_i(t)\rangle = 0$ and the covariance $\langle dW_i(t)dW_j(t)\rangle = \mathrm{d}t\delta_{ij}$. In the numerical implementation, the approximation [26]

$$\Delta W_i = \theta_i\sqrt{\Delta t} \tag{4.23}$$

is used, and θ_i and Δt are the standard Gaußian random number and the computational time step. This stochastic Wiener process represents the random walk of particles in the physical space and the effects of molecular diffusion process on the mean composition [26].

The above system of stochastic differential equations for particle properties is solved using the Euler's forward integration method [48]. The flow mean velocity and the turbulent mixing frequency needed in Eqs. (4.19)- (4.22) are obtained from Eulerian finite-volume calculations and are computed by a bilinear interpolation scheme from the Eulerian mesh points. The same scheme is used to evaluate the particle mean fields as [187]

$$\langle\Phi\rangle = \frac{\sum_{n=1}^{N_p} m_n^*\Phi_n^* g(\mathrm{x}_n^*)}{\sum_{n=1}^{N_p} m_n^* g(\mathrm{x}_n^*)} \tag{4.24}$$

where $g(\mathrm{x}_n^*)$ is the bilinear basis function [187], and the summation is applied over N_p particles present in the volume. m^* denotes the mass weight of gas particle. In the evaporating spray flows, the additional mass source is distributed within the entire flow, and m^* evolves following [145]

$$\frac{\mathrm{d}m^*}{\mathrm{d}t} = m^*\frac{\langle S_{\mathrm{v}}\rangle}{\langle\rho\rangle} \tag{4.25}$$

For the case of the joint velocity-mixture fraction PDF, the particle trajectory is modeled with the gas velocity determined according to the simplified Langevin equation (see Eq. (3.62)), which is extended by Ge and Gutheil [145] to consider the spray evaporation effect, as [85, 145]

$$x_i^*(t+\mathrm{d}t) = x_i^*(t) + U_i^*(t)\mathrm{d}t \tag{4.26}$$

$$\begin{aligned} U_i^*(t+\mathrm{d}t) &= U_i^*(t) + \left(g_i - \frac{1}{\langle\rho\rangle}\frac{\partial\langle p\rangle}{\partial x_i} + \frac{1}{\langle\rho\rangle}\left[\langle S_{\mathrm{m},i}\rangle - \langle U_i\rangle\langle S_{\mathrm{v}}\rangle\right]\right)\mathrm{d}t \\ &- \left(\frac{1}{2} + \frac{3}{4}C_0\right)(U_i^*(t) - \langle U_i\rangle)\omega_{\mathrm{t}}\mathrm{d}t \\ &+ (C_0\epsilon)^{1/2}\mathrm{d}W_i. \end{aligned} \tag{4.27}$$

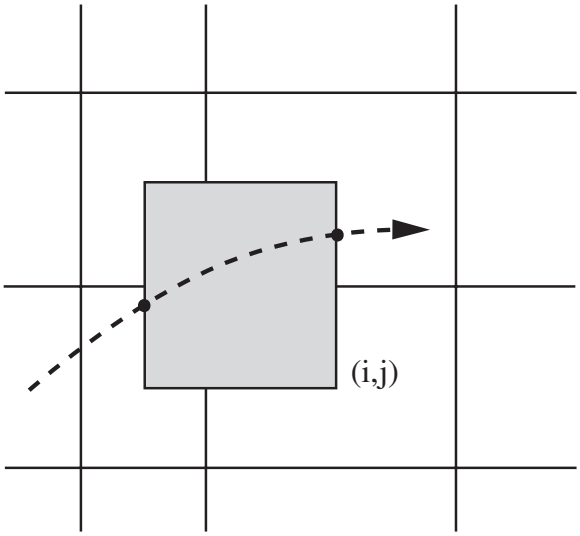

Figure 4.3: Lagrangian droplet tracking in the frame of Eulerian mesh [110].

The molecular mixing of the mixture fraction is modeled with the extended IEM model (see Eq. (4.20)).

4.2.2 Lagrangian Discrete Parcel Method for Dilute Sprays

In this work, spherically symmetric and single-component droplets are assumed for the liquid phase, and the poly-disperse turbulent dilute spray flows and flames are considered and simulated based on the mathematical formulations introduced in the last chapters. The droplet-droplet interactions are neglected, whereas two-way coupling is retained; the interaction between the continuous gas and disperse liquid phase by mass, momentum and energy exchange is considered.

Using the discrete parcel method, different groups of droplets are computed, and the evolution of each group in the continuous gas flow is determined through the Lagrangian tracking method [18]. In one computational parcel, numbers of droplets are identified and share the same properties (position x_d, size r_d, velocity V_d and temperature T_d). Eqs. (3.85), (3.84), (3.94) and (3.99) describe the time evolution of these properties along the trajectory of each computational parcel, and are integrated with a Euler scheme [188].

The source terms stemming from the evaporating dispersed droplets are fed back to the gas phase equations. The solution of the droplet evolution in a Lagrangian way

then allows for the calculation of the spray source terms as [145]

$$S_{l,\Phi} = \frac{1}{V}\sum_{k=1}^{n_d}\left[(\dot{M}_{d,k}\Phi_k)_{\text{in}} - (\dot{M}_{d,k}\Phi_k)_{\text{out}}\right], \tag{4.28}$$

where summation is implemented over the particles that pass through the considered Eulerian mesh cell V, as depicted in the Fig. 4.3. The subscripts 'in' and 'out' indicate the properties that the particle carries with, when moving in or out of the computational cell. $\dot{M}_{d,k}$ is the liquid mass flow rate represented by the k-th droplet parcel, which over time would evolve linearly with the size of the droplets in a way as [145]

$$\dot{M}_{d,k}(t) = \dot{M}_{d,k}(t_0)\frac{r_{\text{d}}^3(t)}{r_{\text{d}}^3(t_0)}. \tag{4.29}$$

The initial value $\dot{M}_{d,k}(t_0)$ is determined from the experimental data at the inlet boundary. In terms of the mathematical models and numerical methods used, proper boundary conditions applied for good representation of a spray flow system are described in the next subsection.

4.3 Boundary and Initial Conditions

The specification of appropriate initial and boundary conditions is crucial for the existence of a solution or a unique smoothed one of the underlying partial differential equations [189]. In the hybrid Eulerian-Lagrangian method, a different treatment is needed for the description of the continuous and the dispersed phases. In the present work, the experimental data of the gas and liquid phase at the first experimental cross-section are employed to determine the inlet conditions for the computation.

For the gas phase, the distributions of flow variables are specified with Dirichlet conditions at the inlet, according to the available measurements, and the turbulent quantities k and ϵ are usually estimated with the equation [80]

$$k = \frac{3}{2}(u')^2, \quad \epsilon = C_\mu^{3/4}\frac{k^{3/2}}{l} \tag{4.30}$$

Here, u' is the measured gas fluctuating velocity. l represents the turbulent length scale and is set to be 10% of the inlet dimension. The model constant C_μ=0.09 [133]. On the other boundaries of the domain, a Neumann type condition with null value is used.

For the PDF particles, the initial number per cell is prescribed to be 50, and at each new time step, new particles are introduced into the domain at the inlet grid cell with particle properties consistent with the inlet experimental condition. At the symmetry line, particles that traverse the boundary are reflected back into the domain to ensure

the zero-flux boundary condition, while they are removed from the ensemble if they move out of the computational domain at other boundaries.

The liquid phase is represented by numerous discrete droplet parcels. At the inlet, the initial number of droplet parcels is set to be 10,000. Each parcel consists of numbers of droplets, and these droplets have identical properties of position, droplet size, and droplet velocity. As to the initial condition, for each droplet parcel, the position is randomly determined by assuming a uniform distribution around each grid point, and the droplet size is prescribed with the Rosin-Rammler distribution [18], matching the measured Sauter mean diameter (SMD) for every spray flow. The total number $N_{\mathrm{d},k}$ of droplets within the k-th droplet parcel can be determined with the droplet size and parcel mass $\dot{M}_{d,k}$ (see Eq. (4.29)) as [85, 136]

$$N_{\mathrm{d},k} = \frac{\dot{M}_{d,k}}{m_{\mathrm{d}}}, \tag{4.31}$$

where, assuming spherical droplets with no deformation, the mass m_{d} of a droplet with radius r_{d} is $m_{\mathrm{d}} = 4/3\pi r_{\mathrm{d}}^3 \rho_l$.

Due to the random appearance of the droplets at the inlet plane, their velocity is determined based on the droplet size and is sampled from a Gaußian distribution matching the experimental mean and fluctuating velocities of the corresponding droplet size groups [85, 136, 190]

$$\mathbf{V}_{\mathrm{d}}(r_{\mathrm{d}}) = \widetilde{\mathbf{V}}_{\mathrm{d}}(r_{\mathrm{d}}) + \mathbf{v}_{\mathrm{d}}^{'}(r_{\mathrm{d}})\sqrt{2}\mathrm{erf}^{-1}(2\theta - 1). \tag{4.32}$$

Here, the parameter θ is a random number uniformly distributed between (0, 1). $\widetilde{\mathbf{V}}_{\mathrm{d}}$ and $\mathbf{v}_{\mathrm{d}}^{'}(r_{\mathrm{d}})$ are, respectively, the experimental values of the droplet mean and fluctuating velocities.

5. Simulations of Non-Reacting and Reacting Spray Flows

For model validation, the non-reacting and reacting turbulent spray flows are simulated with the transported joint PDF method and the spray flamelet model developed in the present work. The test cases include the nonreacting acetone spray flows and reacting spray flows with liquid fuel ethanol. The experiments are conducted on the Sydney spray burner by Gounder, Kourmatzis, and Masri [28, 101] at the University of Sydney, Australia.

5.1 Acetone Spray Flows

In the experiments, the non-reacting spray jets consist of eight cases of acetone evaporating sprays. The effects of different inlet mass loading and turbulence levels on the flow structure are studied. In addition to the non-reacting cases of acetone, two non-reacting, non-evaporating kerosene sprays are provided. In this work, the numerical simulations of acetone evaporating spray flows using transported joint gas velocity-mixture fraction PDF method are presented, and both the droplet turbulent dispersion and evaporation are studied [85]. In the following section, the experimental setups of the test cases are described firstly. Then, numerical results for the acetone spray flows with different characteristics of the turbulence and inlet liquid mass loading are shown and discussed by comparison with the experimental data [28, 101].

5.1.1 Description of the Test Case

The schematic of the spray burner is depicted in Fig. 5.1. The burner comprises of three main streams, i.e. a central atomized spray jet, an annular hot-pilot and an outside air co-flow. In case of non-reacting spray flows, the hot-pilot stream is replaced by an air stream with the same characteristics of the outside air co-flow. The central nozzle diameter of the spray jet is $D = 10.5$ mm. The jet is surrounded by an annular pilot stream with a diameter of 25 mm. The whole burner assembly is situated in a co-flow stream of air having a diameter of 104 mm and four air inlets with a bulk velocity of

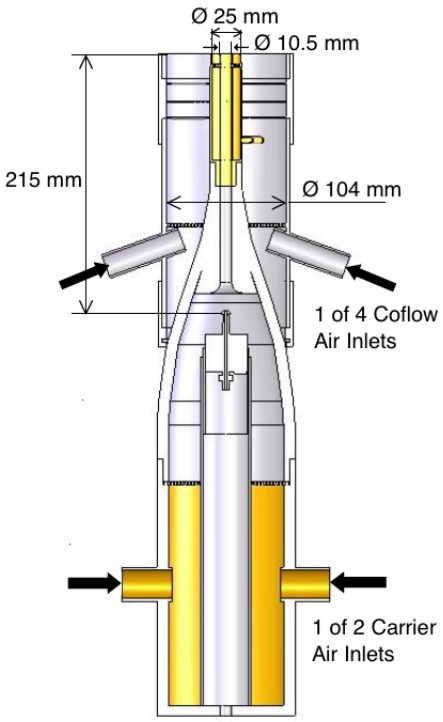

Figure 5.1: Geometry of the experimental configuration by Gounder et al. [28].

Table 5.1: Inflow conditions of the acetone sprays SP2, SP6, and SP7, set B, taken from Gounder et al. [28].

Parameter	SP2	SP6	SP7
Bulk jet velocity (m/s)	36	36	60
Carrier mass flow rate (g/min)	225	225	376
Liquid fuel injection rate (g/min)	75	45	75
Liquid fuel rate at jet exit (g/min)	33.9	26.7	44.2
Vapor fuel rate at jet exit (g/min)	41.0	18.3	30.8
Mixture fraction at jet exit	0.154	0.0752	0.0757
Jet Reynolds number	31,800	28,100	46,700

4.5 m/s. The central spray of droplets is generated using an ultrasonic nebulizer, the head of which is located inside the burner with 215 mm distance from the nozzle exit plane. A more detailed description of the experimental setup is given by Gounder et al. [28].

In the experiments, the laser Doppler velocimetry (LDV) and phase Doppler anemometry (PDA) are applied for the measurements of the mean velocity, turbulence intensity, and droplet size as well as mass flux. These two systems are both the laser optical in-

strument and use light-scattering interferometry for the velocity measurements [11, 191]. Therefore, no calibration is required, and high accuracy and resolution are obtained. PDA makes use of the phase difference caused by the scattered light from two different detectors to determine the droplet size [191]. Experimental studies using these two techniques have been conducted for the different two-phase flows [192–194].

In the present study, the spray jet flows labeled as SP2, SP6 and SP7, which differ in the inlet liquid mass loading and the carrier air velocity, are simulated. The inflow conditions of these three spray flows are given in Tab. 5.1.

5.1.2 Results and Discussion

Figure 5.2 shows the contour plot of the computed mixture fraction of three test cases SP2 (top), SP6 (center) and SP7 (bottom). In the simulation, the mass fractions of chemical species are determined with the local mixture fraction, and thus, Fig. 5.2

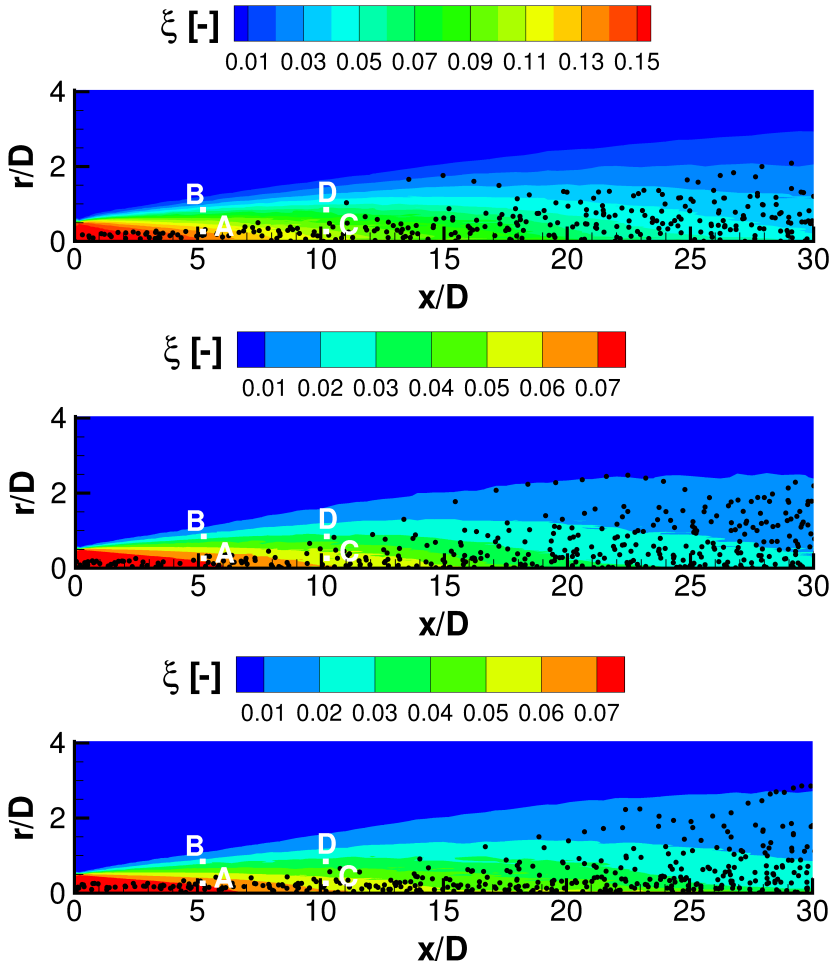

Figure 5.2: Contour plot of the mean mixture fraction for SP2 (top), SP6 (center) and SP7 (bottom) [85].

also reflects the distribution of vapor fuel concentration in the flow field. It can be seen that the level of the value of mixture fraction in SP6 and SP7 is quite similar, whereas they are lower than that of SP2. Also, near to the nozzle exit, a high mixture fraction zone is found, which indicates that the high concentration of fuel vapor in this area may retard the evaporation of the incoming droplets, because the mass transfer coefficient is lower compared to a gas ambience of air. The filled black dots in Fig. 5.2 display representative distributions of droplets. The droplets are mainly transported in axial direction due to their large initial momentum near the jet exit, and as long as moving downstream they gradually travel towards the outer regions of the central main jet. In the computation, local stochastic data are collected for the analysis of the statistic correlations of fluid properties, i.e. the gas velocity and mixture fraction, and four monitor points A, B, C, and D are situated at different positions in the flow field, cf. Fig. 5.2.

In Fig. 5.3 (a), the cross-averaged evaporation rate for these three sprays are presented along the axial direction. It is seen that SP7 reaches the highest spray evaporation rate compared to other two cases, SP2 and SP6, even though SP2 has the same liquid mass loading as SP7 at the inlet boundary. The difference between SP2 and SP7 in the evaporation rate is even doubled at the locations of $x/D = 5$ and 10. This can be partly attributed to the fact that, at the nozzle exit, a lower liquid fuel mass rate of 33.9 g/min is found in SP2 compared to 44.2 g/min of SP7; however, as shown in Fig. 5.2, the pre-vaporized liquid acetone forms an accumulation of fuel vapor near the inlet, which holds back the evaporation processes of the injected droplets. In SP2, the vapor mass fraction in this domain is almost twice of that in SP7. This is even more obvious when looking at the spray evaporation rate of SP2 and SP6 at $x/D = 5$, where the evaporation rate in SP2 is even lower than that of SP6 because of the high concentration of fuel vapor in SP2. In these three evaporating spray flows, the droplet evaporation reaches its peak value near the location of $x/D = 10$, after which the evaporation of droplets slows down again. The position of $x/D = 10$ corresponds to the location where the influence of the inlet fuel vapor becomes weaker.

Figure 5.3 (b) shows the comparison of the evaluated evaporation rates for five different droplet size groups in spray flow SP2. The evaporation rate conditioned on size group 20 µm $< d_\mathrm{d} \leq$ 30 µm describes higher magnitudes than that of other four droplets groups. Comparatively, for the droplet size group 40 µm $< d_\mathrm{d} \leq$ 50 µm, the evaporation rate is relatively low, but it reaches the same level as the group of 20 µm $< d_\mathrm{d} \leq$ 30 µm at location $x/D = 30$, which implies that the larger droplets may function as main factor in spray evaporation. The trend in the other two flows, SP6 and SP7, is similar as shown in Figs. 5.3 (c) and (d), respectively. The plot confirms that intermediate droplet sizes highly contribute to the evaporation and fuel

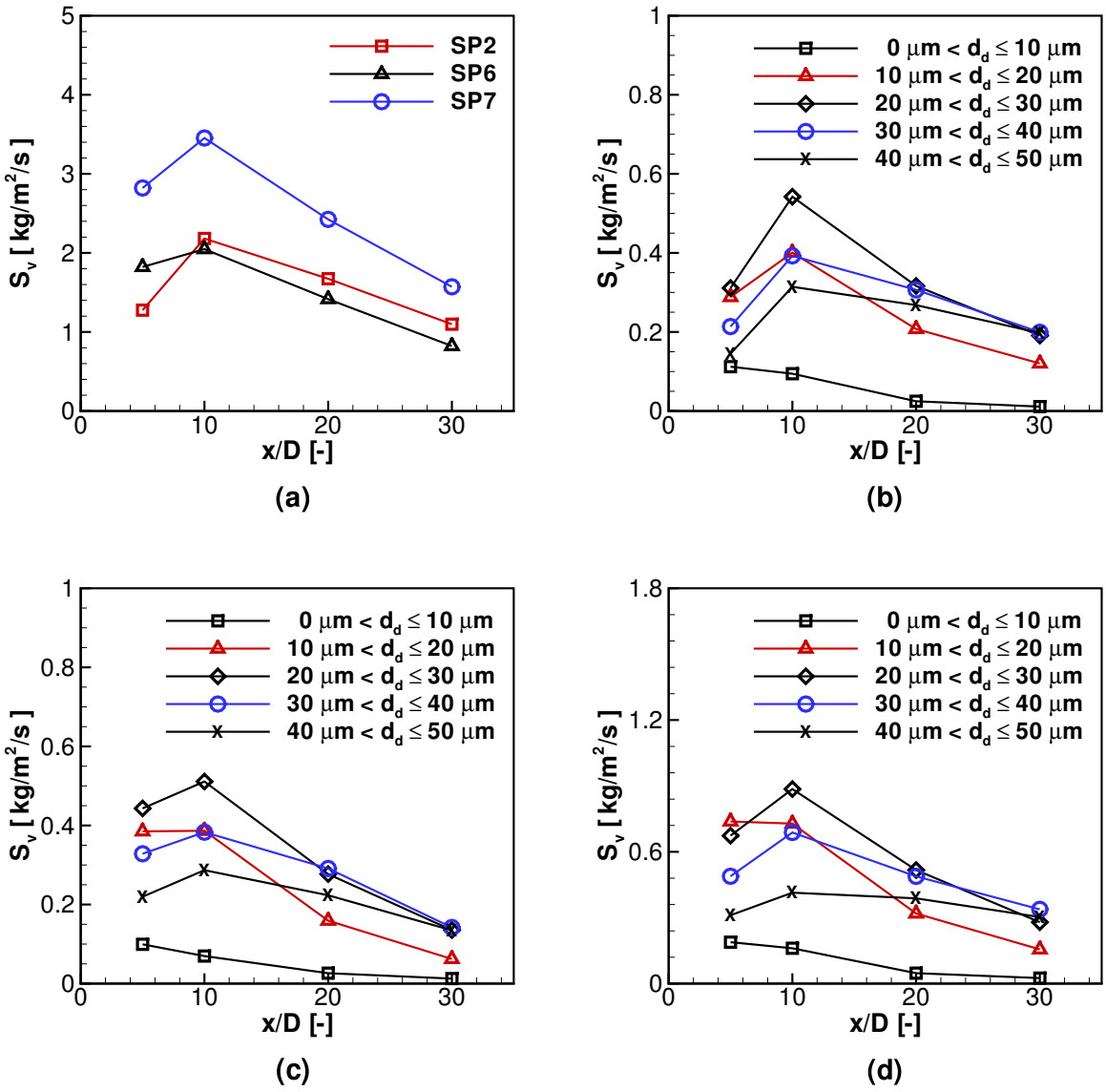

Figure 5.3: Axial profiles of the cross-sectional total mean evaporation rate of SP2, SP6 and SP7 (a); evaporation rate for different droplet size groups in spray SP2 (b), SP6 (c) and SP7 (d) [85].

vapor source. Small droplets evaporate fast, but they cool down the gas environment, leading to retardation of spray evaporation, and larger droplets will need more time to evaporate because of droplet heating.

The computed radial profile of Sauter mean diameter (SMD) is compared with the experimental results (taken from Gounder et al. [28]) as shown in Fig. 5.4. From top to bottom, these figures illustrate the results at locations $x/D = 5$, 10 and 20, for SP2 (top), SP6 (center) and SP7 (bottom), respectively. At the axial positions $x/D = 5$ and $x/D = 10$, good agreement between the computed and the experimental SMD is

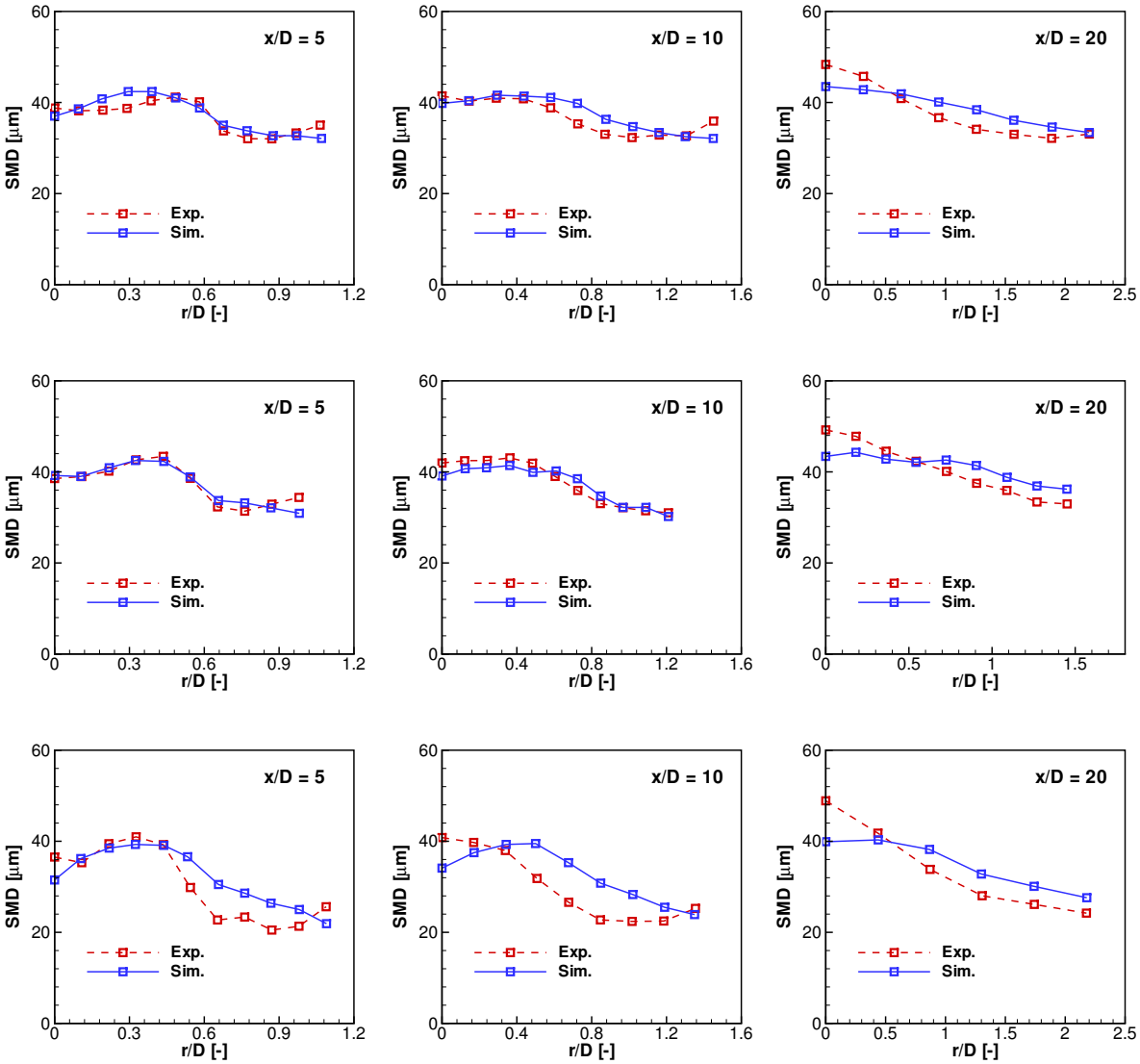

Figure 5.4: Radial profiles of the Sauter mean diameter, SMD. SP2 (top), SP6 (center) and SP7 (bottom) [85]. The experimental data are provided by Prof. Masri at the University of Sydney, Australia [28, 101].

achieved, except for the case SP7, where some deviation exists. At higher distance of $x/D = 20$, for three cases, the numerical results seem to under-predict the SMD near the centerline. As displayed in Fig. 5.3, in all the three sprays, the droplet evaporation rate peaks around the location $x/D = 10$, and it can be expected that the trend of the Sauter mean diameter will be similar at positions $x/D = 5$ and $x/D = 10$, whereas at location $x/D = 20$, the SMD increases due to the intense evaporation of intermediate sizes of droplets. It is also worth to note that the profile of the SMD in SP7 differs from the other two sprays. It indicates that the inflow liquid mass loading hardly influences the droplet diameter distribution in contrast to the inlet turbulence level.

Figure 5.5 shows the computed radial profiles of liquid volume flux compared with measurements (by Gounder et al. [28]) for three cases. Similar to the SMD radial profiles, at upstream cross-section $x/D = 5$, the computed liquid volume flux matches well with the experimental data, whereas further downstream at $x/D = 20$, the computed liquid volume flux near the centerline is higher than in the experiment. This over-prediction implies a tendency of droplet accumulation near the centerline as droplets move downstream, which has also been observed in other discrete Lagrangian droplet calculations [195]. This explains the underestimation of the SMD at $x/D = 20$, cf.

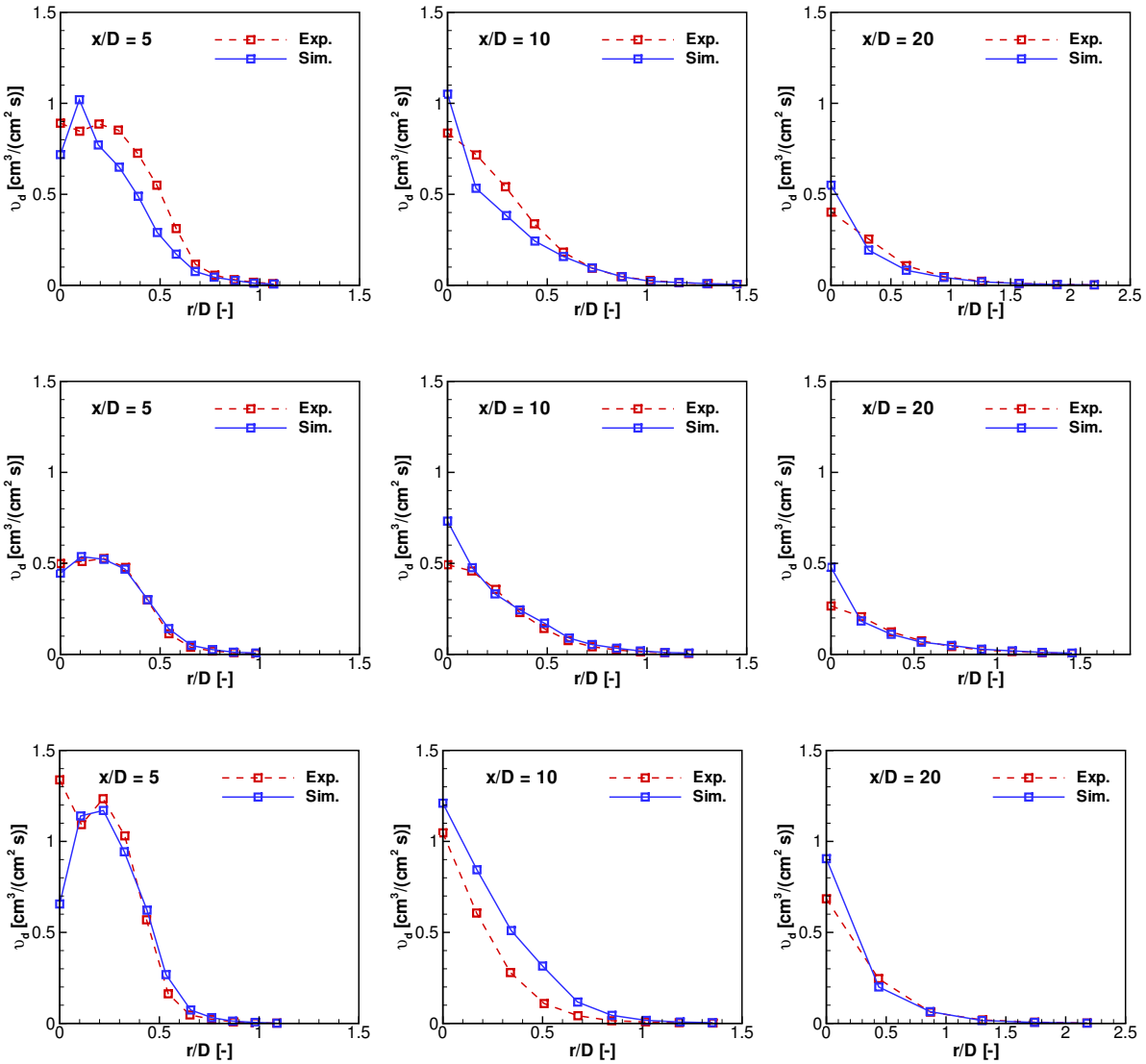

Figure 5.5: Radial profiles of the liquid volume flux. SP2 (top), SP6 (center) and SP7 (bottom) [85]. The experimental data are provided by Prof. Masri at the University of Sydney, Australia [28, 101].

Fig. 5.4. In SP7, at the location $x/D = 10$, the computed liquid volume flux is higher than the experimental data along the radial direction. This may be explained by an underestimation of the turbulence intensity, which leads to a weak radial transport of droplets and thus, the axial convection dominates in this region.

Figures 5.6 and 5.7 present the radial profiles of the droplet axial mean and root mean square (r.m.s) velocities for the size group $0 < d_{\mathrm{d}} \leq 10$ µm at axial positions $x/D = 5$, 10 and 20. It is shown that the computed axial mean velocity profiles generally follow the trend of the experimental data, even though at $x/D = 20$, the droplet

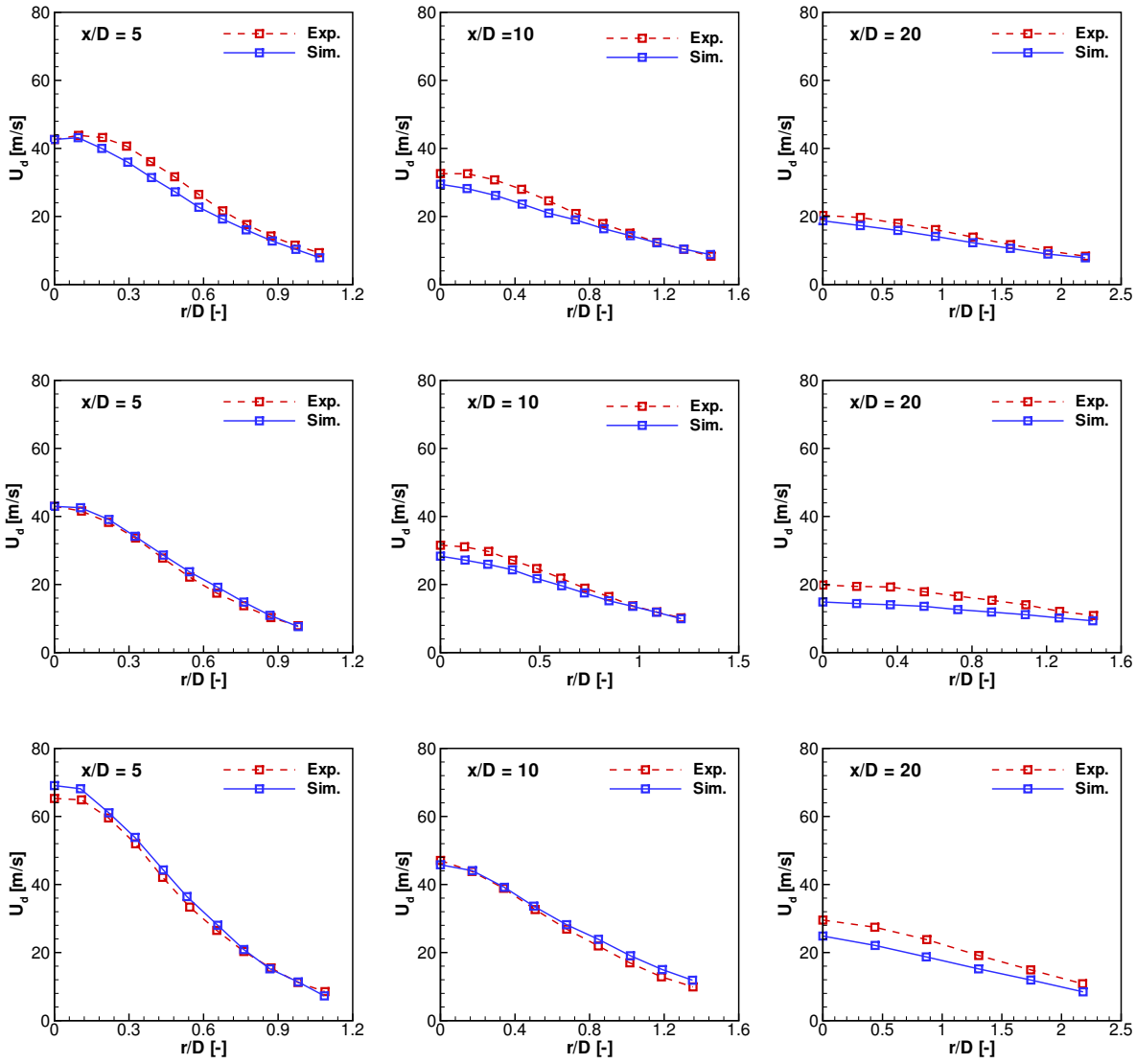

Figure 5.6: Radial profiles of the droplet mean velocity for size group $0 < d_{\mathrm{d}} \leq 10$ µm. SP2 (top), SP6 (center) and SP7 (bottom) [85]. The experimental data are provided by Prof. Masri at the University of Sydney, Australia [28, 101].

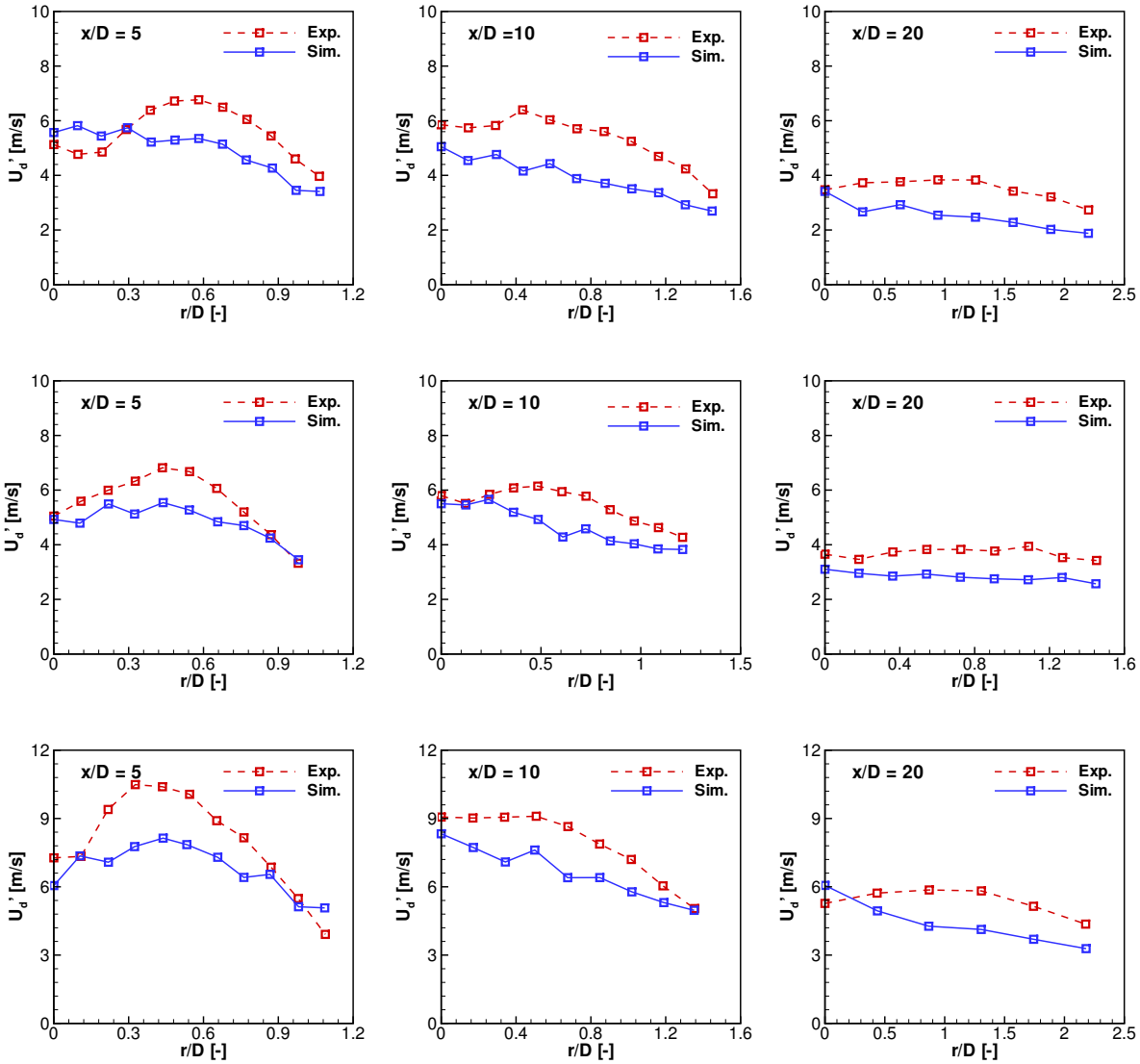

Figure 5.7: Radial profiles of the droplet r.m.s velocity for size group $0 < d_{\mathrm{d}} \leq 10$ µm. SP2 (top), SP6 (center) and SP7 (bottom) [85]. The experimental data are provided by Prof. Masri at the University of Sydney, Australia [28, 101].

axial velocity tends to be underestimated. Comparatively, the droplet axial fluctuating velocity shown in Fig. 5.7 presents an apparent discrepancy between numerical and experimental data. At the upstream location of $x/D = 5$, the profiles of droplet axial r.m.s velocity exhibit a peak value in radial direction around $r/D = 0.6$, $r/D = 0.4$ and $r/D = 0.3$ for test cases of SP2, SP6 and SP7, respectively. This marks the general locations of the intense shear layer in the jet flows, where the production of turbulent kinetic energy is enhanced. Small droplets with diameters less than 10 µm are usually treated as tracer particles for the carrier gas flow, and they essentially follow the fluid flow due to their low Stokes number. Here, the peak value of droplet fluctuating veloc-

ity for the small size class $0 < d_d \leq 10$ µm is not well predicted, which means that the gas-phase turbulence intensity is under-predicted in the present simulations. Due to this underestimation of turbulence level in this domain, the radial turbulent dispersion of small droplets is weakened, which leads to the accumulation of small droplets near the centerline, and this partly explains the over-prediction of the droplet volume flux at downstream locations in Fig. 5.5.

Figures 5.8 and 5.9 present the radial profiles of the axial mean and fluctuating

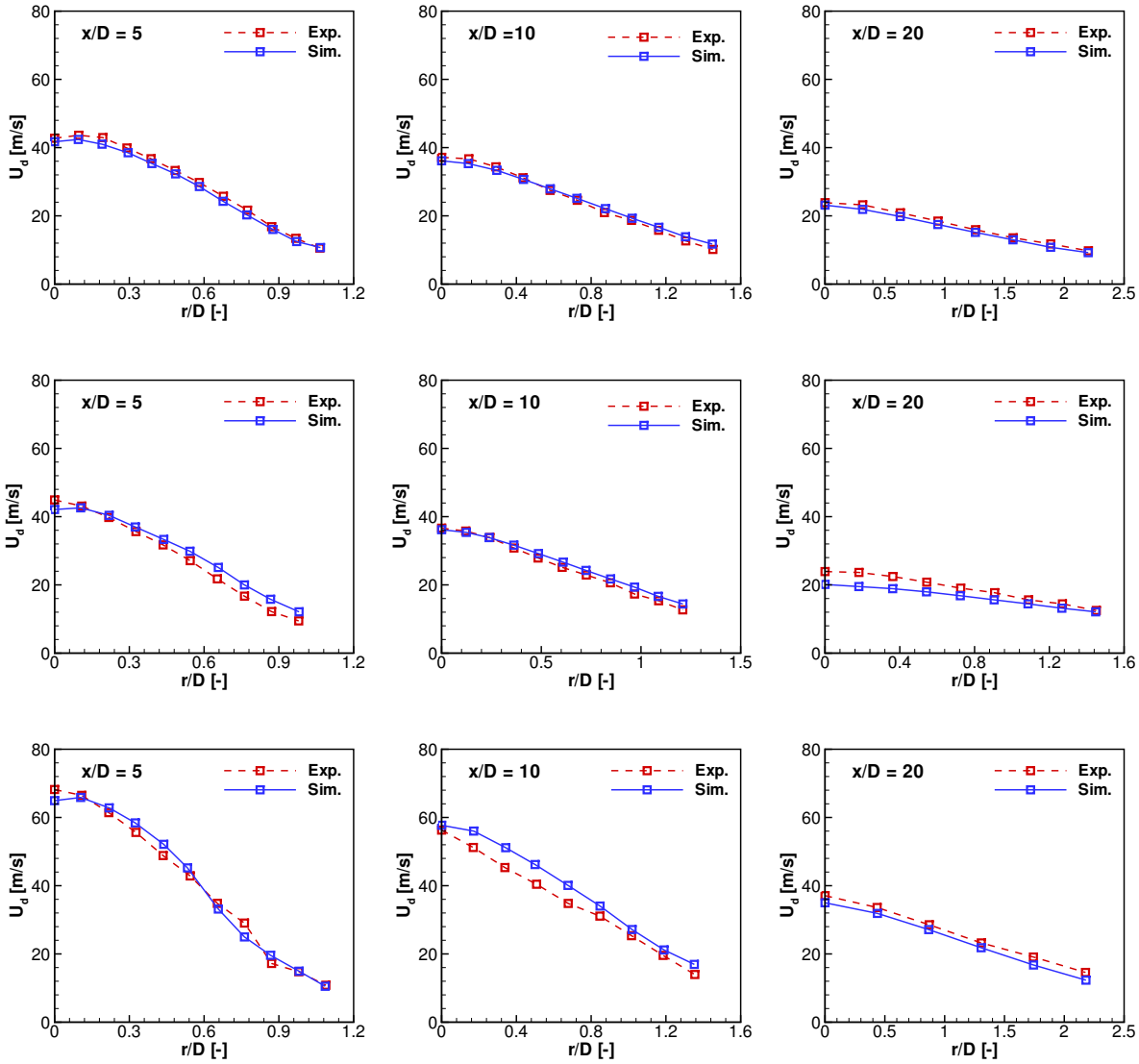

Figure 5.8: Radial profiles of the droplet mean velocity for size group 40 µm $< d_d \leq$ 50 µm. SP2 (top), SP6 (center) and SP7 (bottom) [85]. The experimental data are provided by Prof. Masri at the University of Sydney, Australia [28, 101].

velocities for the larger droplet size group 40 µm $< d_{\mathrm{d}} \leq$ 50 µm. Regarding the mean droplet velocity, good agreement between computational and experimental results is observed, however, compared to the behavior of small droplets shown in Fig. 5.7, the computed r.m.s velocity of larger droplet matches better with experiments, especially at the location $x/D = 5$; this is primarily due to the fact that large droplets are less responsive to the turbulent fluctuations in the fluid flow. It is worthy to note that for the spray flow SP7 in Fig. 5.9 at position $x/D = 5$, there is a peak between $r/D = 0.6$

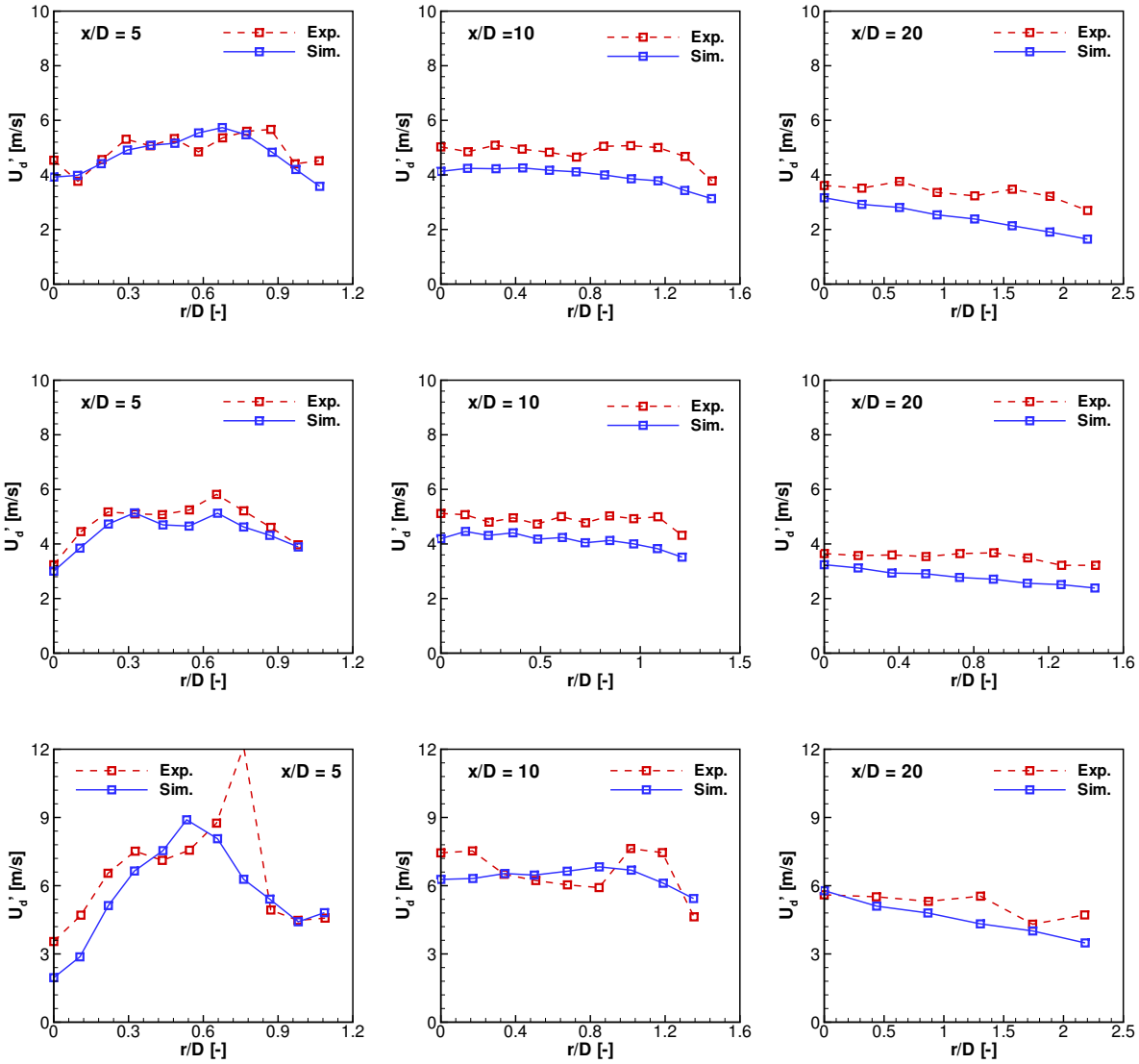

Figure 5.9: Radial profiles of the droplet r.m.s velocity for size group 40 µm $< d_{\mathrm{d}} \leq$ 50 µm. SP2 (top), SP6 (center) and SP7 (bottom) [85]. The experimental data are provided by Prof. Masri at the University of Sydney, Australia [28, 101].

and $r/D = 0.9$. The computed results cannot capture this high value, which may be responsible for the overestimation of the SMD of SP7 near this region, cf. Fig. 5.4, because the high turbulence level in this region may reduce the number of large droplets through the turbulent dispersion, leading to a lower predicted value of SMD.

Numerical studies of acetone spray characteristics in such non-reacting turbulent gas flows were also reported in several previous works [58, 196]. Chrigui et al. [58] used RANS-based RNG (Re-Normalization Group) $k-\epsilon$ turbulence modeling for gas phase simulation, and a non-equilibrium evaporation model for the evaporating spray. In their computations, the acetone spray flows SP1, SP2 and SP5 with different carrier air flow rates are simulated, showing a discrepancy of the axial mean velocity at upstream locations, whereas good agreement with experimental data is obtained further downstream. For the fluctuating velocity, the results for the axial velocity show a better agreement with experiment in case of SP2, but for the other two sprays, an underestimation is observed. In terms of droplet volume flux, their computed results show, especially at upstream locations, a droplet accumulation at the outer edge of the spay flow, where the computed value is higher than the experimental data, and near the centerline, the droplet volume flux is somewhat under-predicted. Thus, even though there are still some discrepancies found in their computations, a more sophisticated turbulence model is still expected to improve the simulation results and the turbulent dispersion of droplets characterizing a wide range of Stokes number. The test cases SP1 and SP2 are also studied by De et al. [196], where the experimental set A rather than the set B is used, and a standard k-ϵ model is applied. Generally, a much better match between the computed results and measurements is obtained, which may be attributed to the lack of consideration of the radial droplet velocities, where the comparison may not be made due to the lack of experimental data in set A.

In the present calculations, the transported joint PDF model allows for the study of local statistical correlations of gas velocity and mixture fraction. Therefore, four monitor points A–D are selected, cf. Fig. 5.2. These four points in SP2, SP6 and SP7 are located at the same positions. Positions A and B reside at the cross-section $x/D = 5$ and positions C and D at $x/D = 10$. The local joint PDF of gas velocity and mixture fraction for cases SP2, SP6 and SP7 is presented in Figs. 5.10, 5.11 and 5.12, respectively, where the plots (a), (b), (c) and (d) correspond to the locations A, B, C, and D, respectively.

It can be seen that by comparison of the joint PDF of SP2, at the upstream locations $x/D = 5$ an almost linear correlation of the gas velocity and mixture fraction is observed in point B, whereas in A, some scattering exists, showing deviation to the linear dependence. Moreover, the mixture fraction at position B shows a much narrower range of values compared to the other three positions, leading to a PDF values

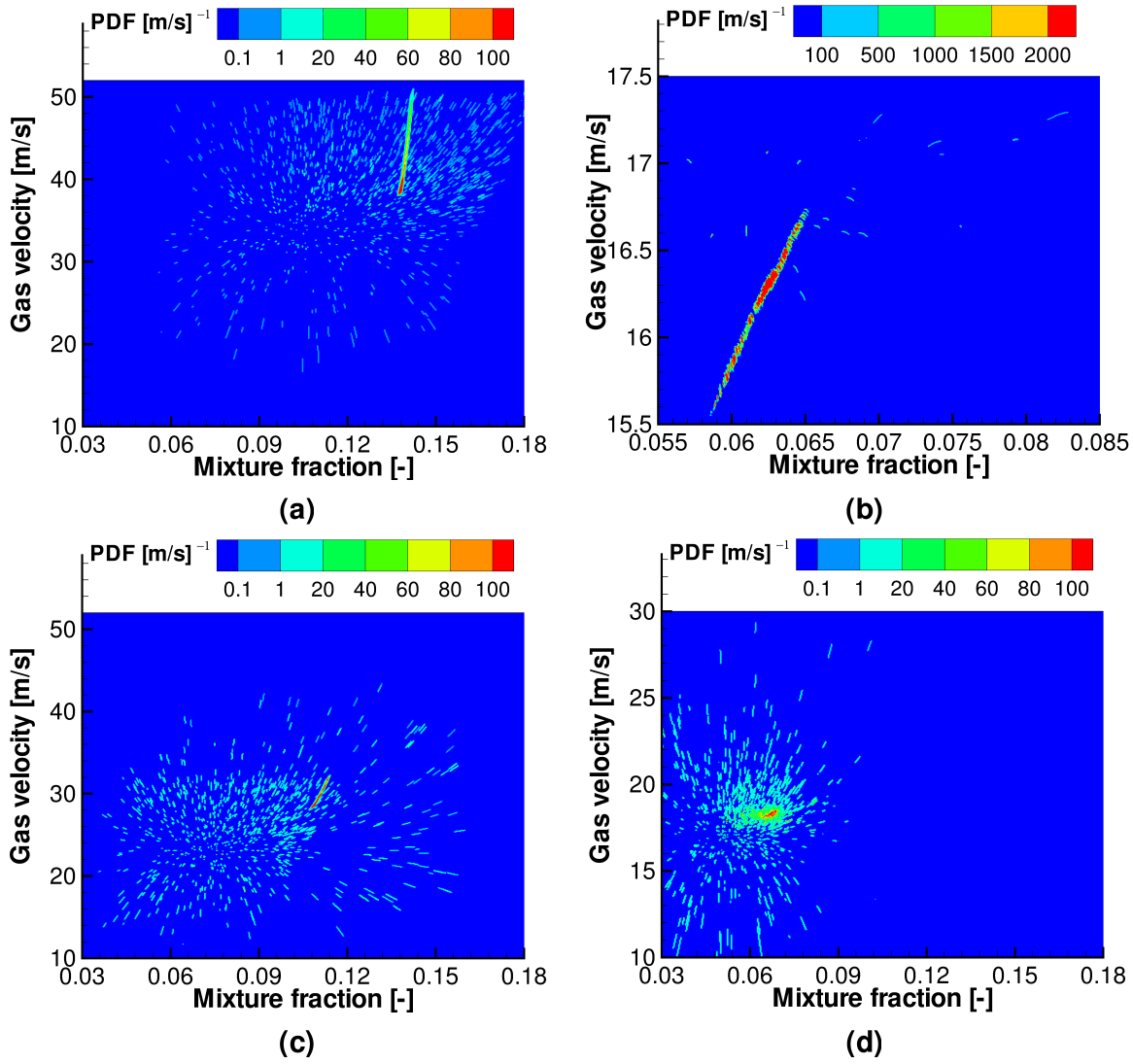

Figure 5.10: Joint probability density function of the gas velocity and the mixture fraction for positions (a) - A, (b) - B, (c) - C, and (d) - D, cf. Fig. 5.2, in spray flow SP2 [85].

up to 2,000 $(\mathrm{m/s})^{-1}$ compared to about 100 $(\mathrm{m/s})^{-1}$ for other positions. Moving downstream to the location $x/D = 10$, the joint PDF of the gas velocity and the mixture fraction tend to cover over the entire local range. However, compared with the outer edge positions B and D, the correlations of the gas velocity and the mixture fraction at positions A and C, which are close to the centerline, are more similar to each other than those away from the centerline at positions B and D; this may be attributed to the dominant effect of turbulent convection of the gas flow near the centerline. At position B, the mixture fraction attains much lower absolute values compared to the other positions, since position B resides outside of the spray jet, where the influence of spray particles is absent.

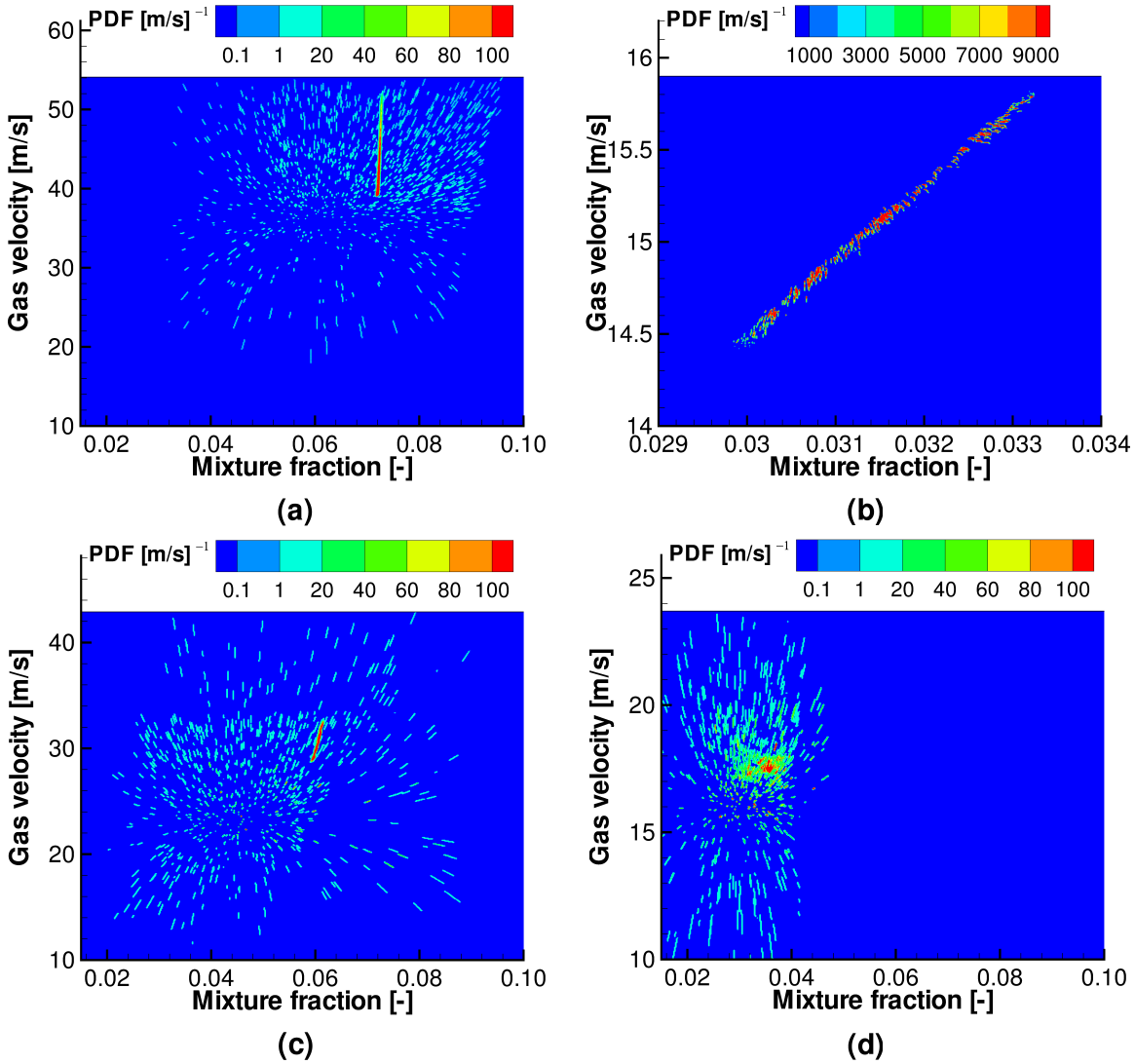

Figure 5.11: Joint probability density function of the gas velocity and the mixture fraction for positions (a) - A, (b) - B, (c) - C, and (d) - D, cf. Fig. 5.2, in spray flow SP6 [85].

Compared with SP2, in SP6 and SP7, the correlation of the gas velocity and mixture fraction shows similar behavior. The most apparently different location is at position B, where the linear correlation in SP6 is more intense, resulting in the local joint PDF value up to 9,000 $(\mathrm{m/s})^{-1}$, whereas in case SP7, the value of the joint PDF declines to 100 $(\mathrm{m/s})^{-1}$, and much more scattering exists, showing a weaker dependence. This may be due to the fact that location B resides in the turbulence shear layer, and in SP7, the local turbulence intensity is much higher than in the other two sprays.

Here, the results of this statistical correlation between gas velocity and mixture fraction may be compared to previous results for a turbulent methanol spray flow injected through a hollow-cone nozzle [197, 198]. There, similarly four monitor points

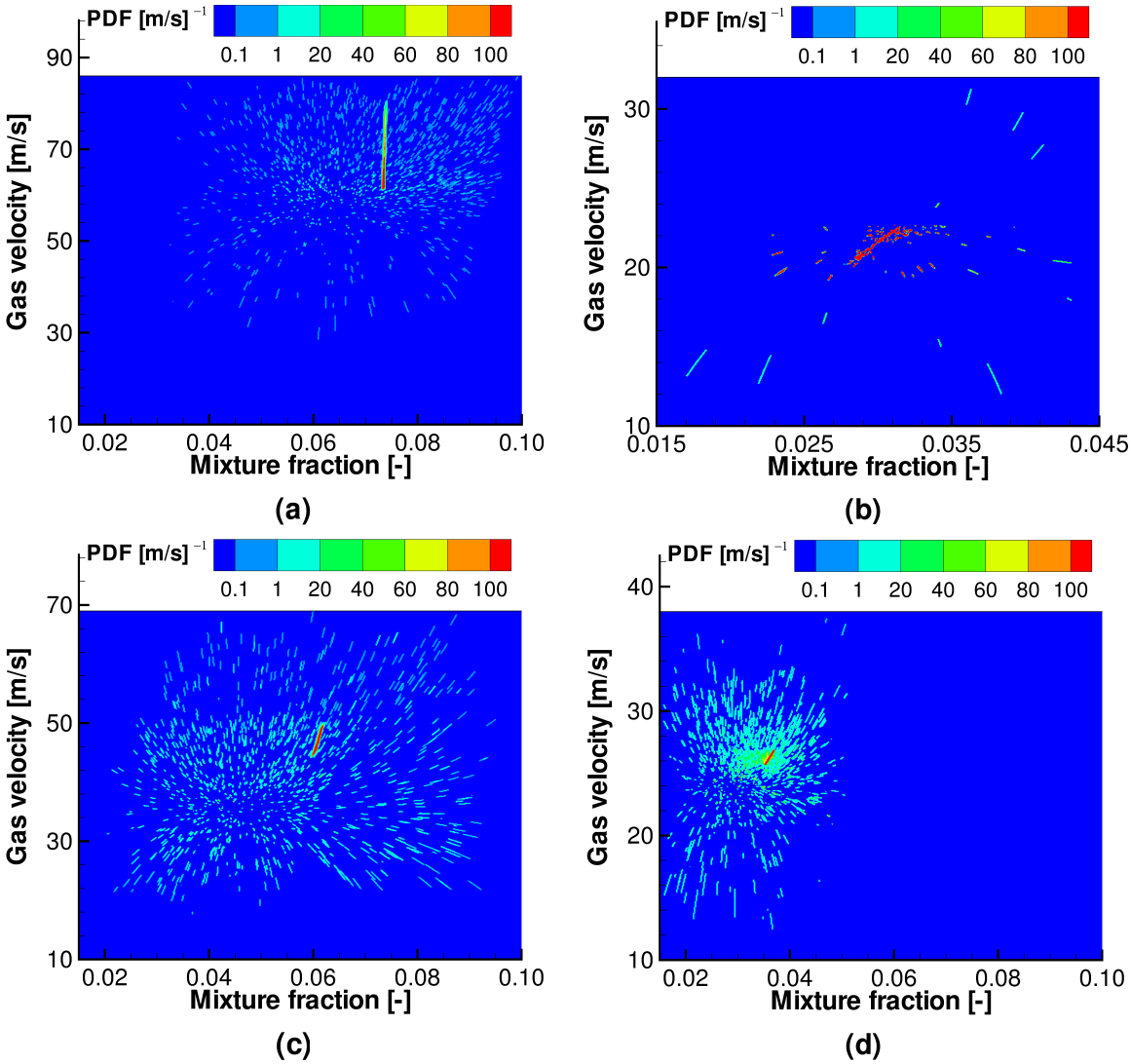

Figure 5.12: Joint probability density function of the gas velocity and the mixture fraction for positions (a) - A, (b) - B, (c) - C, and (d) - D, cf. Fig. 5.2, in spray flow SP7 [85].

were chosen; two reside near the centerline and two are located at the outer edge of the spray. In this methanol spray [198], the gas velocity and the mixture fraction show much stronger correlations, and a piecewise linear relation exits at the positions near the centerline. In contrast, in the present acetone spay, the joint PDF near the centerline shows a linear correlation only for the rich mixture, and a scattered distribution is found further downstream at $x/D = 10$, indicating that the turbulence intensity is larger in the sprays studied here compared to that methanol/air spray flow [197].

5.2 Ethanol/Air Spray Flames

In this section, the reacting spray flows are numerically studied with the newly proposed combined transported joint PDF and spray flamelet/ progress variable approach. The turbulent piloted ethanol/air spray flames EtF2, EtF6, and EtF7 with different inlet flow conditions are simulated and discussed with the comparison of experimental data available from [28, 101]. The focus is on the properties of the polydisperse sprays in the turbulent reacting flows and their effects on the flame structures. These spray flames also belong to the experimental spray jet flames studied in the group of A. Masri at the Univeristy of Sydney [28, 101].

5.2.1 Description of the Test Case

The geometry of this Sydney spray burner (cf. Fig 5.1) has been described in section 5.1.1. In the reacting case, the annular pilot stream is arranged around the central spray jet for flame stabilization, and a hot mixture of acetylene, hydrogen and air at stoichiometric condition is introduced. The central ethanol spray, carried by an air flow, traverse a pre-evaporation distance before reaching the nozzle exit, so that a mixture of vapor fuel and air is found at the jet exit. The measurements include the Laser Doppler Velocimetry and Phase Doppler Anemometry for the droplet velocity and size distribution, and thermocouple measurements for gas temperature at different downstream locations.

Thermocouples are used to measure the gas temperature based on the thermoelectrical property of metals, where the dissimilar metals are used to form two junctions and the temperature difference between these two junctions is determined by the induced voltage [11]. The measured temperature based on the metal junctions can be

Table 5.2: Inflow conditions of the ethanol spray flames, EtF2, EtF6, and EtF7, set B, taken from Gounder et al. [28].

Parameter	EtF2	EtF6	EtF7
Bulk jet velocity (m/s)	36	36	60
Carrier mass flow rate (g/min)	225	225	376
Liquid fuel rate at jet exit (g/min)	66.3	41.1	60
Vapor fuel rate at jet exit (g/min)	8.7	3.9	5
Mixture fraction at jet exit	0.0372	0.017	0.013
Jet Reynolds number	30,500	27,400	45,600

very different from that of surrounding gas because of the effects of heat transfer by convection, conduction, and radiation, which then can affect the accuracy of thermocouple measurements [11]. Despite this disadvantage, due to their economy and simplicity, thermocouples are still a widely used type of temperature sensor for measurement.

The experimental inflow conditions for the spray flames, EtF2, EtF6, and EtF7 are given in Tab. 5.2. As spray flame EtF7 shows a highest Reynolds number, more intense interactions between spray, turbulence and chemistry are expected in this flame and thus, validation of the newly proposed formulation of a combined transported three-variate joint PDF and spray flamelet/progress variable approach is applied in the simulation of EtF7. Spray flames EtF2 and EtF6 are simulated with previous formulation developed by Ge and Gutheil [84] in terms of the formulation (3.50) for the comparison.

5.2.2 Results and Discussion

For the reacting spray flows, the description of combustion chemistry is needed, and in the present work it is achieved using the spray flamelet model, where the flamelet library is constructed by pre-calculating a laminar spray flame in the counterflow configuration. A detailed chemical scheme consisting of 38 species and 337 elementary reactions [199, 200] and detailed transport properties are adopted. The determination of boundary conditions for this laminar spray flame calculation is motivated by the setup of experiments under consideration, and it contains a mixture of vapor fuel and air serving as carrier gas for the mono-disperse ethanol spray, which is directed against an opposed air stream in the counterflow configuration. According to the experimental conditions for case EtF7, the droplets are carried by fuel/air mixture with a vapor fuel mass fraction of 0.013. All streams enter at the ambient gas temperature of 300 K at atmospheric pressure, and the initial spray and carrier gas velocities equal 0.44 m/s [75, 201]. The calculation of this laminar spray flame in the counterflow configuration is carried out by my colleague Dr. H. Olguin [75, 201].

The calculated spray flame structures are then tabulated into a flamelet library, using a reaction progress variable and a mixture fraction defined in Eqs. (3.47) and (3.52). The reaction source term for the progress variable $\dot{\omega}_{\mathrm{P}}$ ($\dot{\omega}_{\mathrm{P}} = \dot{\omega}_{\mathrm{CO_2}} + \dot{\omega}_{\mathrm{H_2O}}$) is obtained from the established flamelet library. Figure 5.13 shows the contours of (a) the CO_2 mass fraction and (b) the progress variable source term taken from the generated spray flamelet libraries. The peak values of CO_2 formation are in the region around the stoichiometric mixture fraction ξ_{st} of 0.1. This generated spray flamelet library will be used to simulate the ethanol spray flame EtF7, combined with the transported three-variate joint scalar PDF method, Eq. (3.68). To evaluate the performance of this newly proposed spray flamelet/progress variable formulation (SFP) (3.51), in this work, sim-

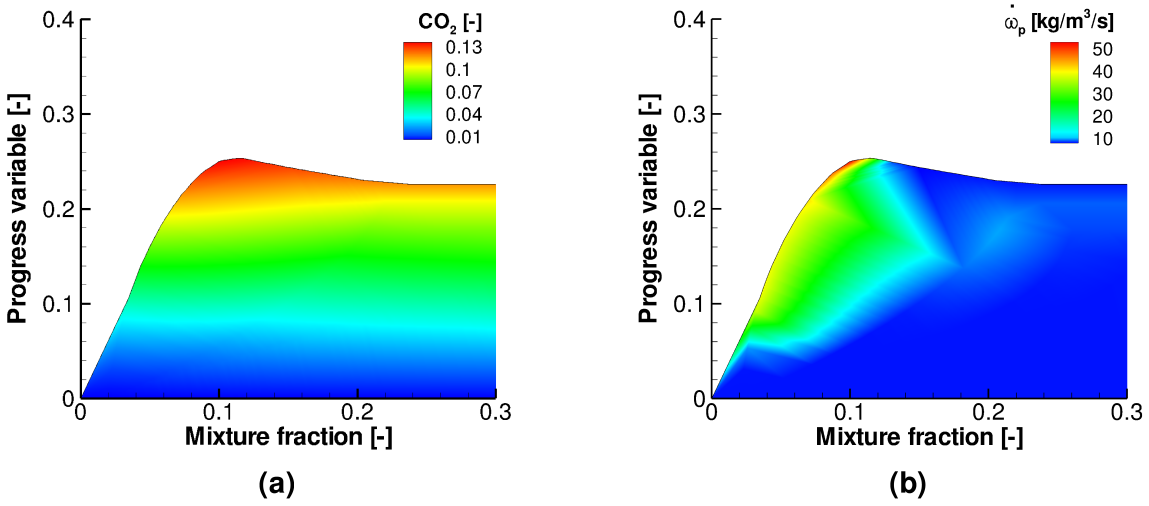

Figure 5.13: The contours of (a): CO_2 mass fraction and (b): progress variable source term in dependence of the mixture fraction and reaction progress variable, taken from the generated spray flamelet library [147].

ulations employing the former transported joint PDF/spray flamelet model (SF) [84, 133] in terms of the formulation (3.50), are also carried out for the comparisons. In the following discussion, the computational results based on these two different formulations will be referred to as "SFP" and "SF", respectively, the first of which stands for the new formulation. Also, simulations of spray flames EtF2 and EtF6 using model formulation (SF) are performed for the comparison.

5.2.2.1 Model Evaluation with Experimental Data

Figure 5.14 shows the radial profiles of gas temperature for the spray flames EtF2 and EtF6. The computed results using the previous model formulation SF are compared with the experimental data at three cross-sections, $x/D = 10$, 20, and 30. It can be seen that, although the trend of experiments is generally reproduced by the numerical results, an apparent overestimation of the gas temperature for both spray flames is observed primarily at the radial positions near the centerline. Specifically, at location $x/D = 10$, the gas temperature is well estimated at the outside of spray jet, and moving to the inner side, however, the computed temperature is much higher than that in experiments. Since this cross-section is close to the nozzle exit where sprays are injected, this high temperature domain predicted by SF modeling is expected to enhance the evaporation of incoming sprays and highly affect the prediction of flame structures further downstream. This can be well demonstrated by comparing the predictions from both the formulation SF and the newly developed formulation SFP.

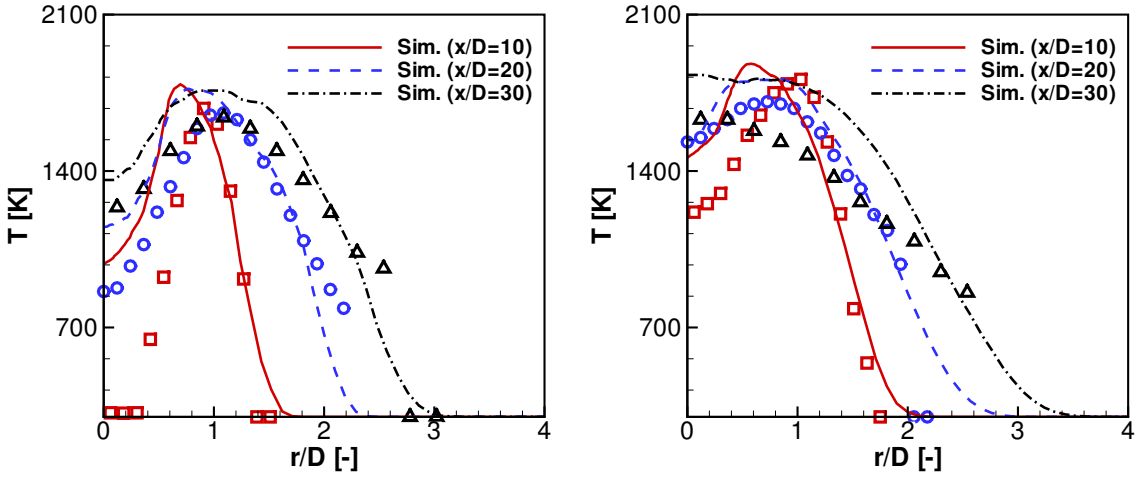

Figure 5.14: Radial profiles of mean gas temperature for (a) spray flame EtF2 and (b) spray flame EtF6; in the plots, □, ○, and Δ represent the experimental data at the cross-sections of $x/D = 10$, 20, and 30, respectively. The experimental data are provided by Prof. Masri at the University of Sydney, Australia [28, 101].

Below, the performance of the new formulation (SFP) propsed in this work is discussed based on the simulation of spray flame EtF7 using both SF and SFP modeling approaches. The numerical results of both gas and liquid properties will be analyzed and discussed with the comparison of experiments taken from Gounder et al. [28].

Figure 5.15 shows the contour plots of mean gas temperature, droplet velocity and evaporation rate for the ethanol spray flame EtF7. In each plot, the numerical results from SF and SFP computations are presented at the left-hand side and right-hand side, respectively. As displayed in Fig. 5.15 (a), the gas temperature predicted by the two approaches shows a significant difference especially close to the inlet. In the SFP (right) computation, the central evaporating spray with a large initial momentum is spread downstream surrounded with the hot-pilot stream, where the pilot flame provides a pre-heating zone for the evaporation of incoming droplets. The inner flame front is established at the downstream around $x/D = 20$. In contrast, an attached flame is found in SF (left) simulation, where the central high-temperature region starts relatively close to the nozzle exit and combustion occurs in a vaporization-controlled reaction regime [202]. Small difference is observed by the comparison of the computed droplet velocity in Fig. 5.15(b), and, due to the flow dilatation induced by the heat release of intense chemical reactions near the inlet, the velocity field from SF is some-

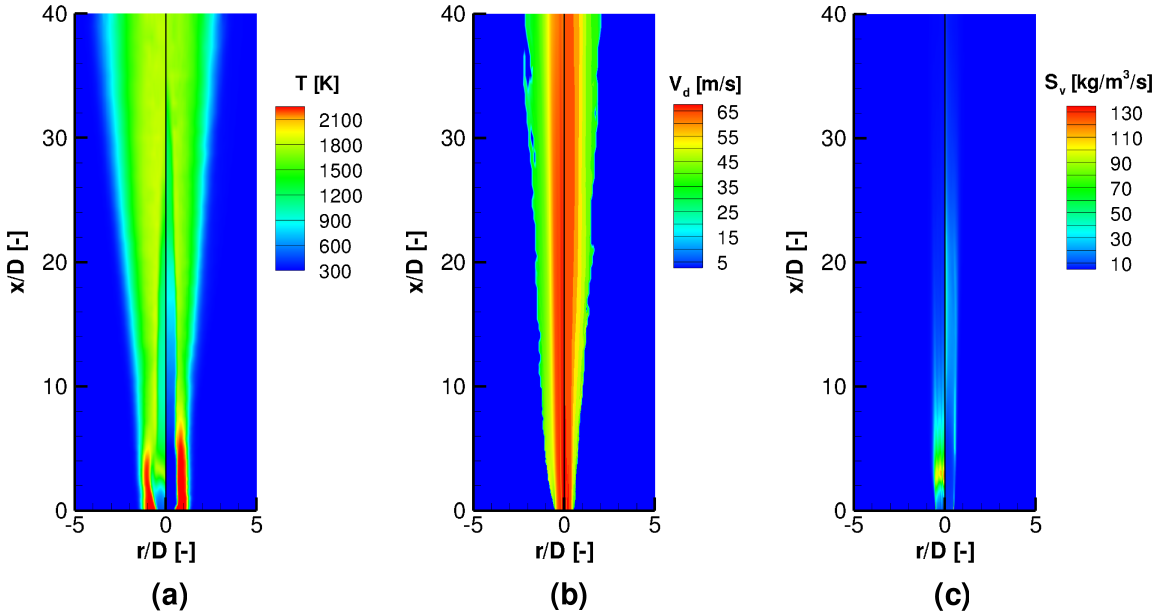

Figure 5.15: Contour plots of (a): gas temperature, (b): droplet velocity, and (c): mean evaporation rate for spray flame EtF7. Each plot consists of computational results from SF (left) and SFP (right), respectively [147].

what broader. The gas-phase temperature can substantially affect the ethanol liquid evaporation with its high volatility at atmospheric pressure. This can be seen from the evaluated evaporation rate shown in Fig. 5.15 (c). As the prevailing high-temperature presented upstream near the exit plane in SF simulation, the droplets in this central region tend to vaporize faster and much more vapor fuel is released compared with the SFP simulation. More comparisons of this difference in evaporation statistics at different cross-sections of the jet flame will be discussed below.

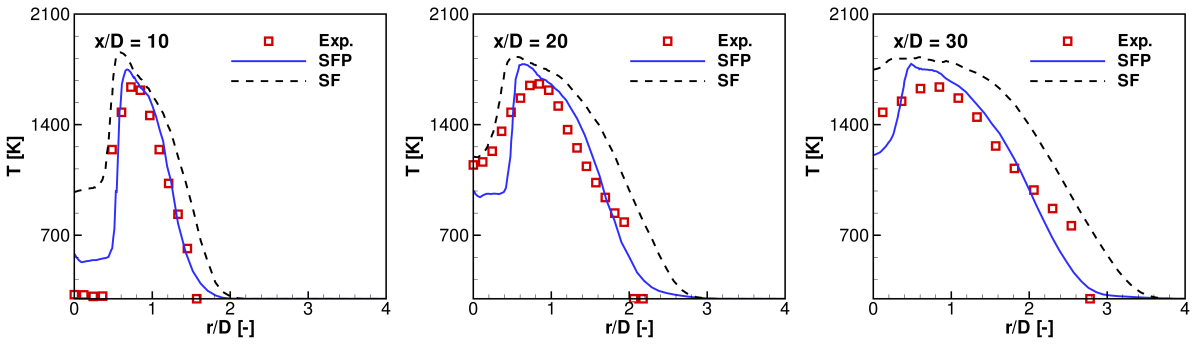

Figure 5.16: Radial profiles of mean gas temperature at three different cross-sections, $x/D = 10$, 20, 30 [147] for spray flame EtF7. The experimental data are provided by Prof. Masri at the University of Sydney, Australia [28, 101].

Figure 5.16 shows the radial profiles of gas temperature computed using the two different approaches at three cross-sections, x/D = 10, 20, and 30. As shown in the figure, a generally good agreement with experimental data (the red dot) is observed for the SFP calculation. Comparatively, the SF temperature are higher than both, the experimental data and numerical results of SFP, which is consistent with the observations from the temperature contour plot depicted in Fig. 5.15 (a). The SF predicts an early combustion at the bottom of this spray jet flame, and droplets start to evaporate immediately after injection. A large amount of vapor fuel is generated, leading to intense chemical reaction and broader flame reaction zone at the downstream. Therefore,

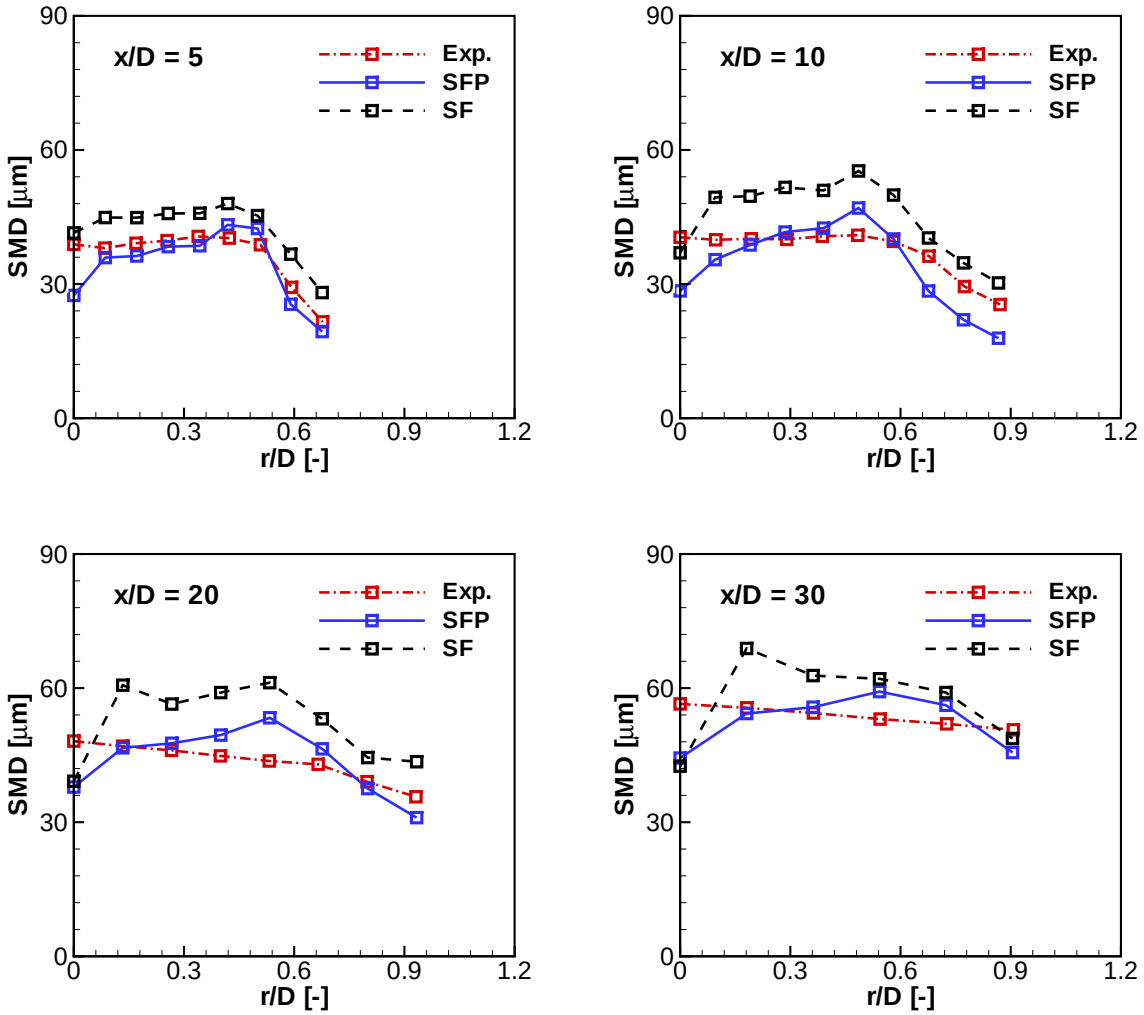

Figure 5.17: Radial profiles of droplet Sauter mean diameter (SMD) at different cross-sections, x/D = 5, 10, 20 and 30 for spray flame EtF7 [147]. The experimental data are provided by Prof. Masri at the University of Sydney, Australia [28, 101].

it can be seen that SFP simulation improves the results of SF, and it well predicts the gas temperature distribution and the combustion mode occurring in the present spray flame. Below, the computed droplet fields are compared with the available experimental data for the droplet size, liquid flux and velocity.

For the liquid phase, the droplet size distribution is characterized by its Sauter mean diameter (SMD). The simulated and measured SMD radial profiles at different axial locations are plotted in Fig. 5.17. As indicated in Fig. 5.16 of the radial gas temperature profiles, the SF approach results in the over-prediction of the gas temperature, which is also reflected on its overestimation of SMD since a hotter gas environment enhances evaporation of the small droplets causing a higher SMD. It can be seen that the computed SMD value in SF is much larger than in the experiments and in SFP predictions. The computed value in SFP generally matches the trend indicated by the experimental measurements at all cross-sections, while it is noted that a peak in the SMD profiles exists around the radial position $r/D = 0.5$, which the boundary of inner cold spray jet and the hot-pilot stream is located. The droplets that traverse this boundary experience a notably steep temperature gradient and thus the enhanced phase transition, which will be the condition where non-equilibrium effects are relevant and droplet properties do not have enough time to relax to its thermodynamic equilibrium.

Additionally, it is observed that the SMD value shows an increment when moving from cross-section $x/D = 5$ to $x/D = 30$, because smaller droplets evaporate more rapidly, and this is more apparent after the cross-section $x/D = 20$, where the inner flame front starts as shown in Fig. 5.15 (a) of SFP calculation (right). This implies that in the present flame structure, accurate simulation of this flame front location will be crucial for the prediction of spray evolution especially in the far-field region.

The liquid volume flux is another proper indicator for spray dynamics evaluation. Results presented in Fig. 5.18 are the computed radial profiles of the liquid volume flux from two models and the available experimental data. It is shown that a large deviation from the measured data is found for the SF calculation, and at the near-field region the liquid volume flux has decreased dramatically. At the upstream location $x/D = 5$, the predicted liquid volume flux given by SF is almost half of that in the measurements, which confirms the influence of the near-field high temperature zone in the SF simulation; combustion taking place in this region consumes most of the incoming liquid droplets, and the released fuel supports a near-field attached flame, which is mainly dominated by the evaporation related parameters, e.g. the liquid inflow mass rate.

Comparatively, SFP modeling shows better performance and its predicted results reproduce the general characteristics of the experimental profiles. At $x/D = 5$, the

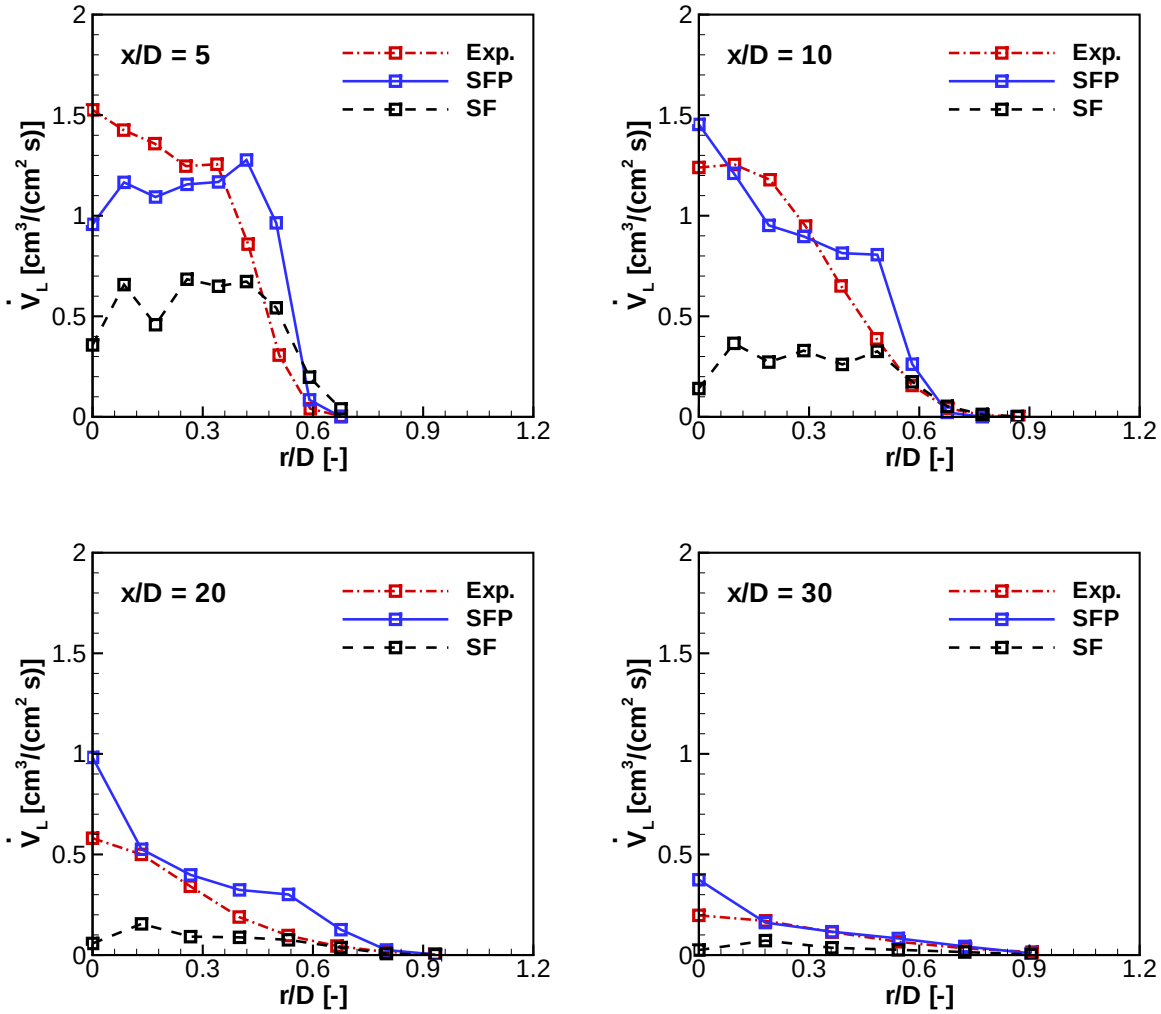

Figure 5.18: Radial profiles of droplet volume flux at different cross-sections, $x/D = 5$, 10, 20 and 30 for spray flame EtF7 [147]. The experimental data are provided by Prof. Masri at the University of Sydney, Australia [28, 101].

disagreement of the calculated and measured values near the centerline can be associated with the overestimated gas temperature in this region as shown in Fig. 5.16, and moving downwards the computed central liquid volume flux is increased again at $x/D = 10$, but later the droplet flux is reduced along with the slowly increased local gas temperature near centerline indicated in Fig. 5.16. The spray droplets are mainly evaporated when reaching $x/D = 20$. The increase of the droplet flux at $x/D = 10$, which is higher than the experiments, indicates the tendency of droplet accumulation near the centerline as droplets move downstream [203]. Previous simulations given by Chrigui et al. [58] reported similar deviations, and there it was argued that the error introduced in the measurement might be part of the reason for these discrepancies.

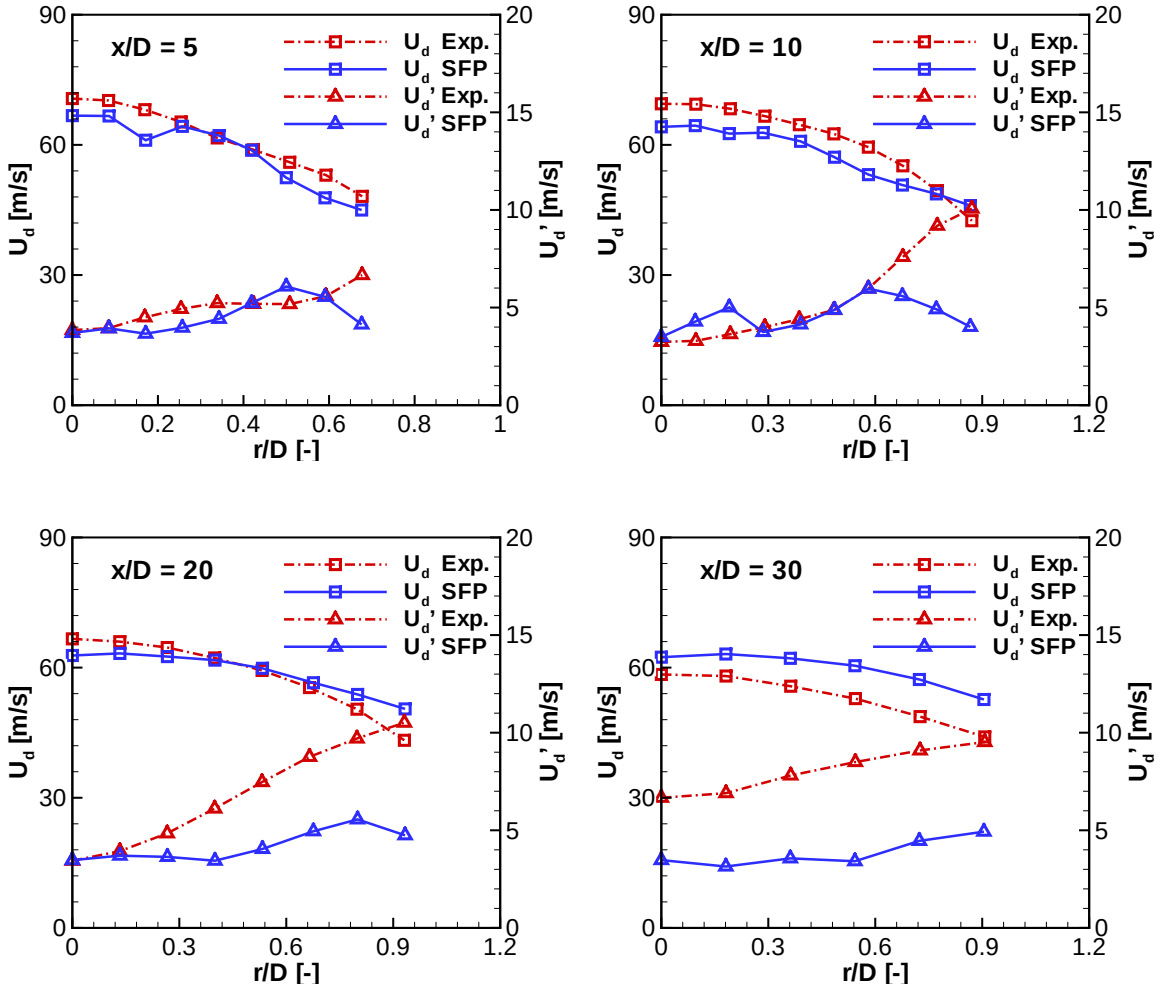

Figure 5.19: Radial profiles of axial mean U_d and fluctuating U'_d droplet velocity at different cross-sections, $x/D = 5$, 10, 20 and 30 for spray flame EtF7 [147]. The experimental data are provided by Prof. Masri at the University of Sydney, Australia [28, 101].

Figure 5.19 presents the simulated and experimentally measured results for the axial component of the mean and fluctuating droplet velocities. As shown in Fig. 5.15 (b), a small difference in velocity profiles between the results obtained by the two approaches is found, and here only the radial profiles from SFP computation are presented and compared with the experimental data. Concerning the mean velocity, the agreement between the numerical simulation and experimental data is reasonable. The droplet velocity is around the inlet bulk jet velocity of 60 m/s. The Sydney spray flame [28] consists of a set of experiments of pilot spray jet flame with a range of inflow conditions, among which the spray flame EtF7 has the largest jet velocity, which is close to the measured blow-off limits of jet velocity about 75 m/s. The high flow rate of the

inner evaporating spray generates a stratified mixture and prevents the hot-pilot propagating through the inner well-mixed vapor/air jet at the upstream. It was evident in the experiments that the most important parameters for determining flame structure include the flow rates of liquid fuel and its carrier air as well as the heat diffusivity from the pilot [28].

Again in Fig. 5.19, as to the fluctuating velocity, the qualitative characteristics of experimental data are computed and an under-prediction exists at the downstream locations. Similar discrepancy for the droplet axial fluctuating velocity is observed in the simulations by De and Kim [190], where the use of a more sophisticated droplet dispersion model is suggested for an improved prediction of gas-droplet interactions and their effects on droplet dispersion. The discrepancies of SMD and droplet volume flux around the radial position $r/D = 0.5$, as shown in Figs. 5.17 and 5.18, are expected to be eliminated if the prediction of droplet dispersion can be improved.

In summary, in terms of both gas and liquid phase mean properties predictions, it can be stated that the new reaction progress variable SFP approach performs much better, and the reaction progress variable helps to identify the progress of gas-phase reaction and characterize the premixed effects, which are of great importance for an accurate prediction of the corresponding spray properties. Detailed statistical analysis of the present flame structures is given in the next subsection by means of this newly proposed formulation, where more physical insights of the combustion modes about this pilot spray may be gained.

5.2.2.2 Local flame structure analysis

In this section, numerical results extracted from the SFP computation are presented for a more detailed flame structure analysis. Figure 5.20 shows the contour plot of the calculated mixture fraction (left) and OH mass fraction (right). The black filled dots display the distribution of the representative droplets in the flowfield. As shown in the mixture fraction plot, sided by the pilot stream with stoichiometric mixture fraction ξ_{st}, the inner lean mixture prevails at the upstream till the locations around $x/D = 20$ near the centerline. Further downwards, an area of high concentration of vapor fuel is observed, which marks the region where inner intense combustion takes place; this is coherent with the gas temperature results observed in Fig. 5.15 (a) (right). At the inner side, the droplet-laden flow with its high momentum travels mainly through the domain near the centerline and is heated up by the heat release originated from the pilot flame, leading to the formation of a fuel pool at the axial distance far from inlet. It is also seen that the OH profile shows negligible values in the core region of the central jet.

Based on the data extracted from the Lagrangian droplet tracking procedure, fig-

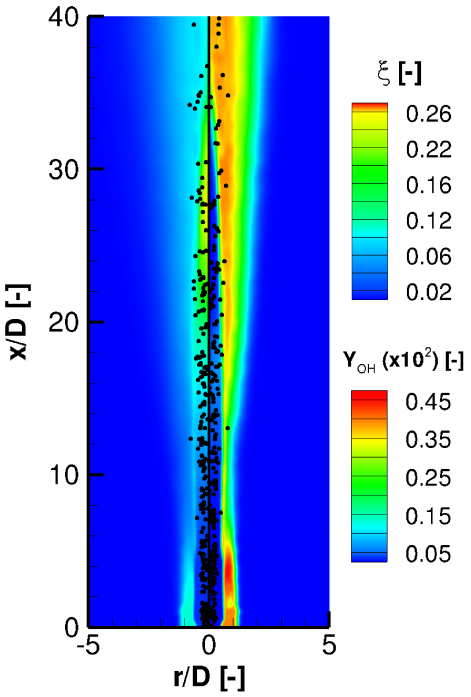

Figure 5.20: Contour plots of mixture fraction (left) and mass fraction of species OH (right) (scaled by 1×10^2) for spray flame EtF7. Filled dots: the representative droplets in the flowfield [147].

ure 5.21 shows the scatter plot of vapor mass fraction Y_{Fs} at the droplet surface as a function of droplet radius r_d. Four monitor points are selected at different positions of the flow field; two of them situate at a cross-section $x/D = 5$ and another two at $x/D = 10$. In each plot, the mass evaporation rate is also presented for each droplet with the colored dots. Y_{Fs} defined by Eq. (3.96) is a function of droplet temperature T_d in terms of Eq. (3.97), and is associated with the mass Spalding number for the determination of the evaporation rate of each droplet.

At the position near the nozzle exit and centerline, due to the high initial momentum and small residence time, the droplets at these regions will not receive much heat from the carrier gas, and their temperature, thus, do not change too much. As displayed in the Fig. 5.21 (a), even though some of the small droplets reach a high value of Y_{Fs}, almost all droplets within different size groups reach the same value of vapor mass fraction around 0.11, which is much higher than that found at the inlet spray jet where the fuel mass fraction is set as 0.013 to account for vaporized fuel as given in Table 5.2. Therefore, it can be stated that the spray evaporation in this region is mainly driven by the large gradient in the vapor mass fraction between droplet surface and surrounding gas flows, which, at the same time, leads to the temperature drop of part of small droplets, indicated by the small decrease of Y_{Fs} shown at the left-hand side of

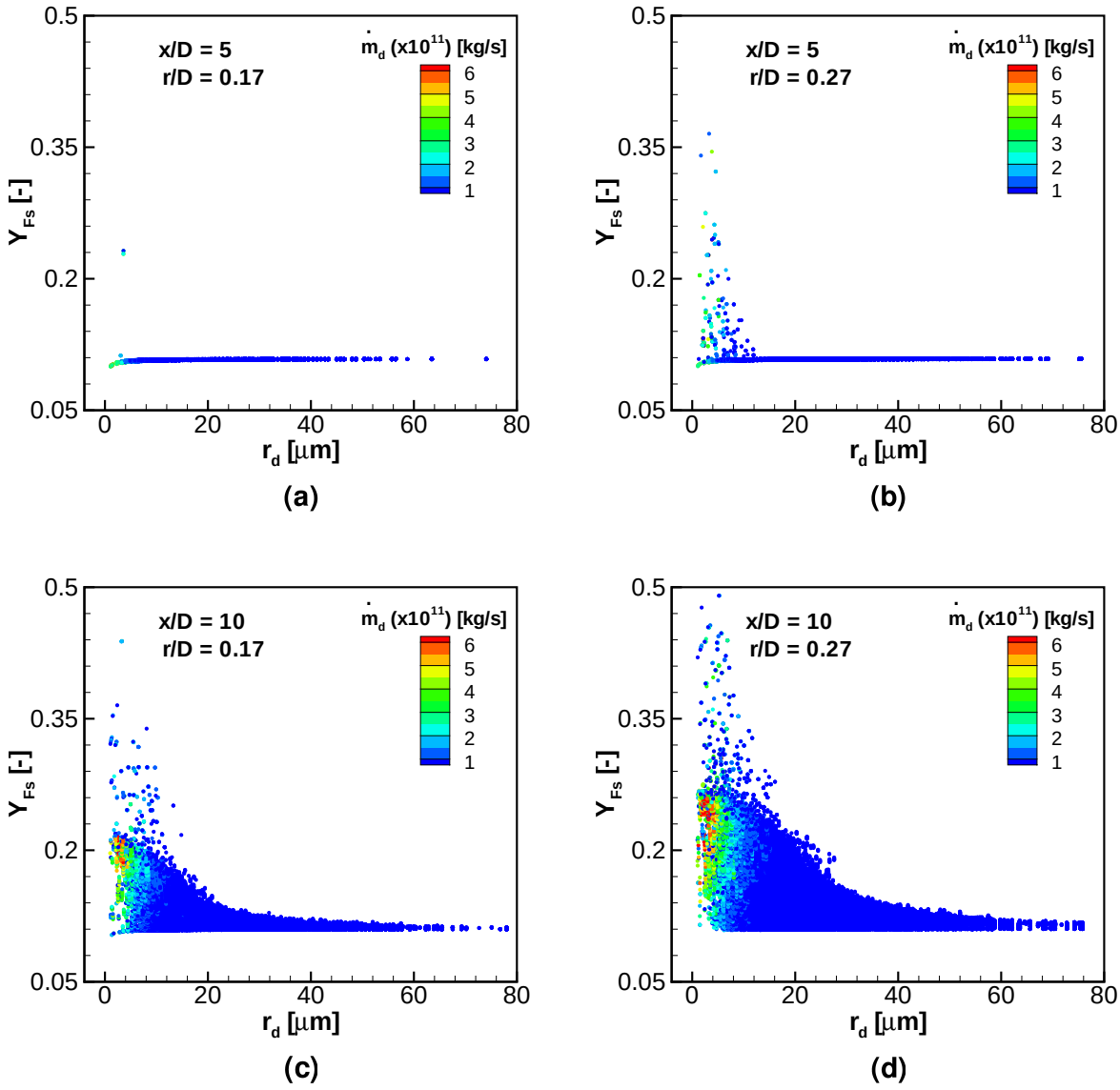

Figure 5.21: Scatter plots of fuel mass fraction at droplet surface Y_{Fs} versus droplet radius r_{d} at four selected positions of spray flame EtF7. Colored dots: the corresponding droplet evaporation rate (scaled by 1×10^{11}) [147].

the blue line in Fig. 5.21 (a). This is because of the latent heat release associated with droplet evaporation.

At the outer side position, the influence of the hot-pilot heating is expected to become more relevant. As shown in Fig. 5.21 (b), compared with Fig. 5.21 (a), for more small droplets their value of Y_{Fs} increases significantly. Further downstream at the axial location $x/D = 10$ shown in Figs. 5.21 (c), (d), this becomes more remarkable, and more intense evaporation is observed with colored dots clouded around the region with small droplet. At the same time, the large droplets begin to become active with

gradual temperature increase due to the heating from the pilot, and their surface mass fraction increases considerably at this downstream location. This is in line with the fact that compared with small droplets, more time is needed for heating up large droplets, and it is most likely related to the droplet size dependent relaxation time τ_{d} appearing in droplet temperature Eq. (3.99).

Figure 5.22 gives the scatter plot of OH mass fraction versus the mixture fraction ξ. The Lagrangian statistical data are extracted from four different cross-sections, where in each axial location the stochastic particle information are collected at all radial positions. As shown in the plots at four axial locations, two distinct parts are found in each plot; a lower 'scatter-part' and an outer side 'line-part', where the upper line-part is consistent with the observation in the piloted turbulent pure gas flames [86, 204],

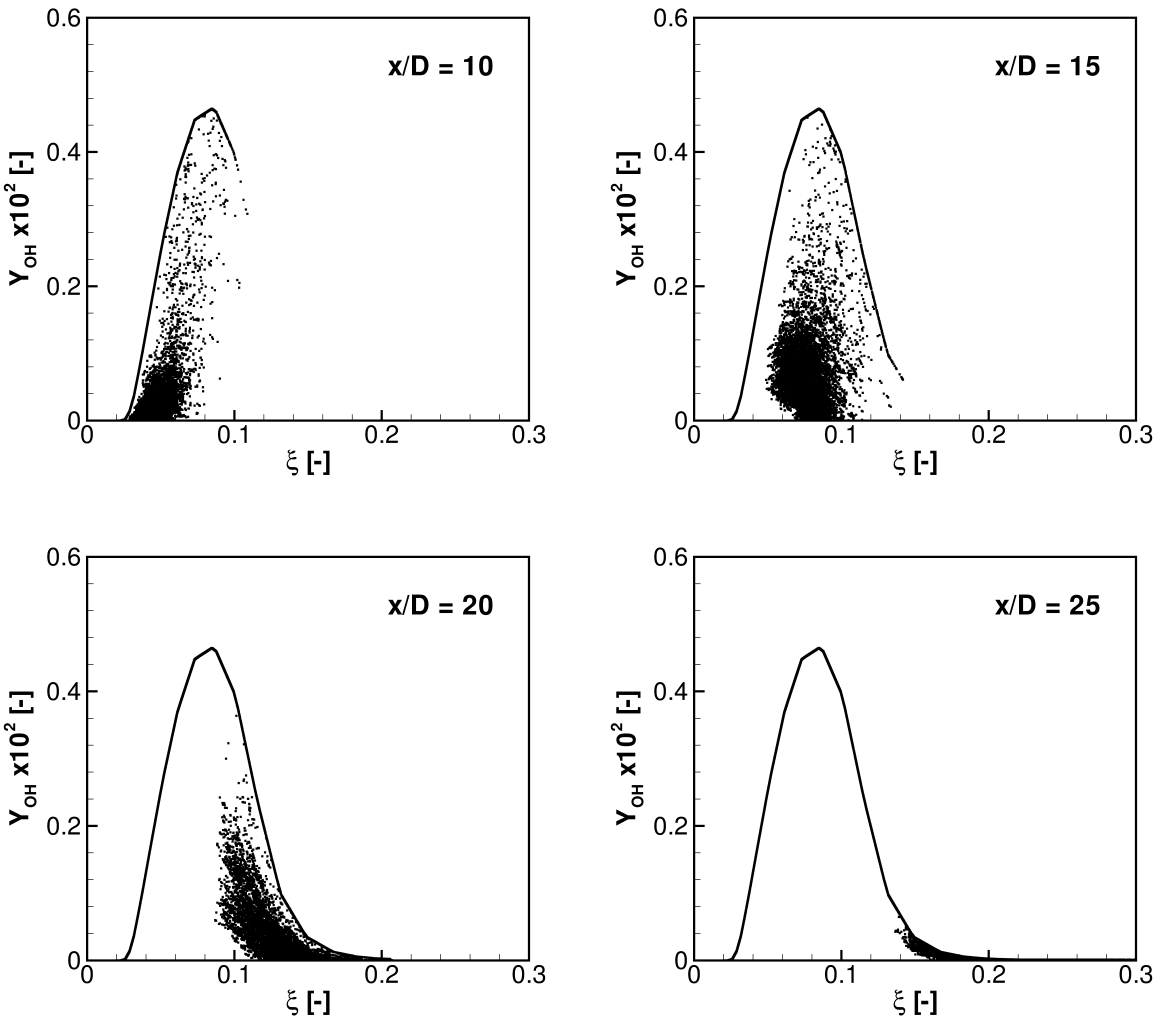

Figure 5.22: Scatter plots of OH mass fraction Y_{OH} (scaled by 1×10^2) versus mixture fraction ξ at four downstream cross-sections of spray flame EtF7 [147].

excepting the lower scatter-part, which is mainly caused by the droplet evaporation in the present spray flame. Since the inlet mixture fraction at the spray jet is below the stoichiometric condition, the lean mixtures are found in the lower part at the upstream location $x/D = 10$, while with inner spray evaporation enhanced downwards as illustrated in the discussion of Fig. 5.21, this premixed lean mixtures move close to the stoichiometric condition (see plot at location $x/D = 15$), and switch to rich conditions at cross-section $x/D = 20$. It is also noted that at $x/D = 10$, nearly all scatter data locate in a domain with relatively small mixture fraction; the extension of OH profiles in the rich side towards downstream positions implies the broadening of the reaction zones due to the presence of evaporating sprays.

Figure 5.23 shows the scatter data of the gas temperature conditioned on the mix-

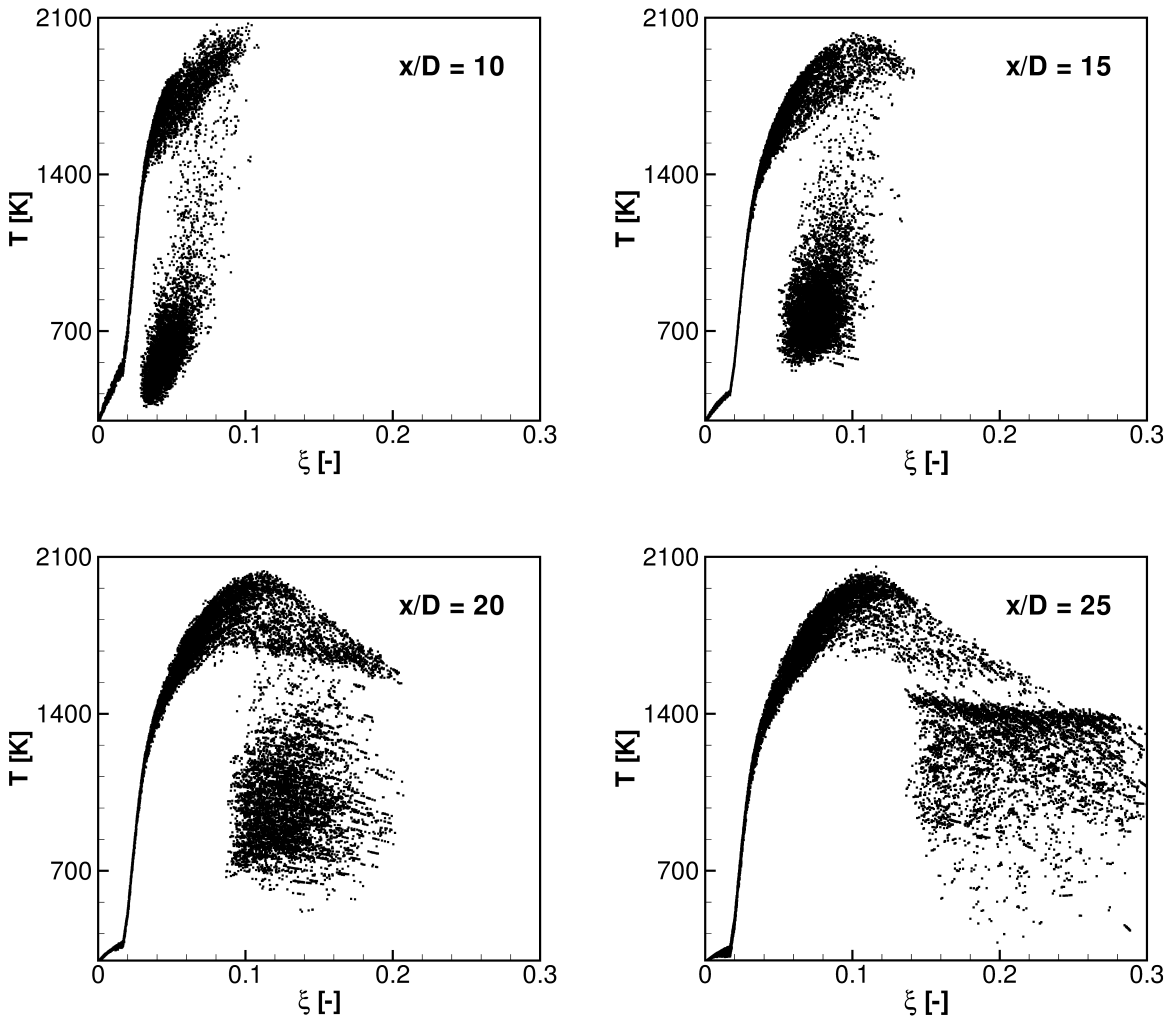

Figure 5.23: Scatter plots of mean gas temperature versus mixture fraction ξ at four downstream cross-sections of spray flame EtF7 [147].

ture fraction. As shown in the figure, similarly two distinguished regions are observed in each plot. The upper regime shows the characteristics of the classical non-premixed flamelet combustion mode, and it resides in the area where the gas temperature peaks around the stoichiometric mixture fraction of 0.1, and gas entities are mainly involved in the mixing between the air coflow and hot-pilot. The lower branch corresponds to the area where gas particles are influenced by the evaporation of the spray, and this region is isolated by the pilot flame, forming a zone where the released vapor fuel mixes and reacts with local carrier gas under the influence of the heating through pilot flame. Therefore, for one given mixture fraction, several points with variable temperatures but equal values of mixture fraction can be found, which essentially is equivalent to the structure of a premixed flame with constant equivalence ratio.

Also, as shown in the plots at $x/D = 10$, 15, with increasing distance from the exit, the lean premixed core at the lower part is gradually heated up due to the interaction with the upper fully burning (diffusion flame) region, and the most reactive region starts to develop at $x/D = 20$, where the temperature of the lower scatter-part rises up significantly and a rich mixture develops. In addition, as noted early in OH profile (see Fig. 5.22), the upper line part has developed from lean side (at $x/D = 10$) to the rich side (at $x/D = 20$), indicating the promotion of diffusion flame to the inside spray jet. Meanwhile, note that in Fig. 5.22, at position $x/D = 25$, few thermochemical states are accessed for the lower part, which implies that diffusion flame appears to be the dominant combustion mode at the far-field region at the present flame conditions.

6. Summary and Outlook

In this thesis, both turbulent non-reacting and reacting spray flows were modeled and simulated using the transported joint probability density function (PDF) method, where in the gas phase the transport equations for the joint PDF of considered gas variables, including the interphase coupling effects, were derived and solved. The dependent variables of joint PDF for the non-reacting spray flows include the gas velocity and the mixture fraction. In the simulation of turbulent reacting sprays, in order to account for the pre-vaporization effects and partially premixed regimes in complex turbulent spray flames, transport equation of a three-parameter joint PDF of mixture fraction, reaction progress variable and gas enthalpy is derived and modeled in a combination of the newly proposed spray flamelet model.

Applied in the simulation of reacting spray flows, the spray flamelet model is used to include the detailed chemical reactions and transport properties, where a flamelet library including the spray evaporation effects is pre-generated based on the calculation of a counterflowing laminar spray flame. The new spray flamelet formulation includes a reaction progress variable in addition to the classical mixture fraction, and the effects of pre-evaporation of the sprays are taken into account by including the pre-vaporized fuel in the carrier gas stream of the fuel spray.

Following the Eulerian-Lagrangian approach with two-way coupling between phases, the spray dynamics is modeled based on a point-particle approximation; the droplet particles are treated as point mass which are affected by the carrier gas through mass, momentum, and energy interactions. The dilute spray is assumed consisting of spherically symmetric droplets that do no interact. The droplet motion is solved by a stochastic Lagrangian tracking approach, and along the droplet trajectories the phase and heat transfers are taken into account by a non-equilibrium evaporation model. The Monte-Carlo Lagrangian particle method is used to solve the joint PDF transport equation, where the discrete joint PDF that is a set of delta function in the sample space of considered variables, is represented by an ensemble of gas particles. For the particle evolution, a Eulerian finite-volume solver is used to provide the necessary information of the turbulence scales, as well as the mean velocity and pressure field.

Model validation is carried out in the frame of the polydisperse turbulent non-reacting and reacting spray flows that have been experimentally studied in the group of Prof. Masri at the University of Sydney, Australia [28, 101]. Specifically, it consists of

the numerical simulations of a series of turbulent acetone spray flows showing different turbulence level and different inlet liquid mass loadings. Futher, the turbulent piloted ethanol/air spray flames are simulated, which exhibit complex local flame structure and provide a good benchmark for evaluating the new modeling formulation proposed in this work. The computed results are compared with the available experimental data [28], including droplet velocity, size distribution and liquid volume flux, as well as the gas temperature in the reacting cases.

In chapter 5, an investigation of non-reacting acetone spray jet flows is presented with the joint gas velocity and mixture fraction PDF method. The extended simplified Langevin model and interaction-by-exchange-with-the-mean (IEM) model are used, respectively, for velocity and mixture fraction evolution of discrete gas particles, and additional terms accouting for two-phase effects are incorporated. The flows considered include three acetone spray jets, denoted as SP2, SP6 and SP7 [28]. These three spray flows form two comparative groups, i.e. one with increased liquid mass loading and fixed carrier gas velocity (SP2, SP6), and the other one preserves the same liquid mass loading but with increased carrier gas velocity (SP2, SP7). These spray flows feature with the polydispersity of spray droplets, which facilitates the study of the characteristics of droplet turbulent dispersion and evaporation.

Generally, a good agreement between computed results and experiments for droplet size and mean velocities is reported. By comparison of the radial profiles of Sauter mean diameter in these three spray flows, it is found that compared with the inflow mass loading, the turbulence level has a more pronounced effect on the droplet size distribution. However, the over-prediction of liquid volume flux is observed near the centerline, which is attributed to the accummulation of droplet in the regions far way from the inlet. The computed droplet axial fluctuating velocity is somewhat smaller than the measurements, and an improved turbulence model is expected to eliminate this discrepancy.

Moverover, the local statistical distribution of the discrete joint PDF of the gas velocity and mixture fraction in the flows are extracted from the transported PDF calculations, and the results are analyzed and compared within these three different spray flows. A linear dependence between the gas velocity and the mixture fraction is found close to the nozzle exit and an intermediate correlation is observed at other positions in the present spray jet flows. The elevated turbulence level of the gas flow results in the scattered distribution that deviates from the linear dependence.

The second part of chapter 5 presents the numerical studies of the turbulent spray flames (EtF2, EtF6 and EtF7) with liquid fuel ethanol. The considered spray flame consists of three main streams, i.e. a central spray jet, an annular hot-pilot and outside air co-flow. The hot-pilot stream is applied for flame stabilization and provides the heat

release for the evaporation of sprays at the inner side. The spray evolution and combustion properties are investigated in the ethanol spray flames. A combined transported joint probability density function and spray flamelet approach for two-phase reacting flows has been developed and applied in the simulation of this complex pilot-stabilized spray flame. The fuel considered is liquid ethanol in air, for which the detailed chemical reaction mechanism at the atmospheric pressure is used [200], consisting of 38 sepcies and 337 elementary reactions. For the evaluation of model performance, two different simulations are carried out. One calculations applied the newly proposed spray flamelet/progress variable approach combined with the joint three-variate PDF transport equation (see Eq. (3.68)); the other one employed the former transported joint PDF/spray flamelet model [84] in terms of Eq. (3.50). In the results discussion, these two simulations are referred to as "SFP" and "SF", respectively, and the first one stands for the new computational formulation.

The experimental data of Gounder et al. [28] are used for results comparision. Simulation of spray flames EtF2 and EtF6 using the model formulation SF shows that the gas temperature is generally overestimated, and a high temperature zone is predicted near the centerline, which is expected to enhance the spray evaporation and influence the flame prediction further downstream.

Validation of newly developed formulation SFP is conducted based on the simulation of spray flame EtF7, which has higher Reynolds number and more intense local interactions between spray, turbulence and chemistry. Computations of spray flame EtF7 based on both SF and SFP modeling approaches are discussed by comparison with the experiments. In terms of the mean gas temperature, and liquid phase properties, i.e. droplet size distribution, liquid volume flux and velocity distribution, the computation with new spray flamelet/reaction progress variable approach SFP shows an improved performance, and the results are in good agreement with measurements. However, the previous model formulation SF appears to over-estimate the occurrence of combustion near the jet inlet, resulting in the overprediction of gas temperature and the droplet sizes, and meantime underprediction of liquid volume flux. In this case, an unphysical attached flame is observed. As to the droplet velocity prediction, small difference is found between simulations SFP and SF, while in both simulations droplet fluctuating velocities are underestimated, indicating the need of using more sophisticated turbulence model or droplet dispersion model to improve the computations.

Based on the simulation using the new formulation SFP, local flame structure is analyzed with the Lagrangian statistics of both gas and liquid phase. The analysis of the scatter plots of fuel mass fraction at droplet surface versus droplet radius shows the important influence of hot-pilot heating on inner spray evaporation, and it can be seen that a deep temperature gradient between inner spray and pilot flame is established,

forming the condition where non-equilibrium effects are relevant. At the same time, results confirm that in the polydisperse two-phase flows the spray with wide range of Stokes numbers would show different behavior to two-phase interactions and accurate prediction of different size group of droplets would be important for the evolution of gas-phase combustion.

The scatter plots of OH mass fraction and gas temperature extracted from the transported PDF calculations are also investigated. A partially premixed combustion is found in this piloted turbulent ethanol spray flame, where nonpremixed, premixed and evaporation-dominated combustion regimes coexist and interact. Due to the pre-vaporization of the ethanol droplets near the nozzle exit, the lean premixed gas mixture is found at the inner side of spray jet. Moving downstream, this inner-sided partially reacted core, which is controlled by spray evaporation, is heated up by the surrounding hot-pilot stream, leading to the extension of reaction zone in the rich side. During this process, the outside diffusion flame is promoted towards the inner side and form a flame front at the downstream locations, where the inner spray evaporation is largely enhanced. Downstream, the diffusion flame becomes the dominant combustion mode.

In summary, a new formulation based on a combined transported joint PDF and spray flamelet model for the consideration of partially premixed combustion regimes has been developed, which in the present situation, is mainly caused by a pilot flame used for flame stabilization. Overall, computations using this newly proposed spray flamelet/progress variable approach allow to account for the reaction progress, distinguishing between mixing-controlled regions and those with intense reactions, and the numerical study in this work provides new insight into the local flame structure influenced by the evaporating sprays.

For the future work, since the accurate flow field information is important for the prediction of disperse liquid phase, it would be interesting to test other turbulence models such as Re-Normalisation Group (RNG) k-ϵ model or Reynolds stress modeling approach. Also, the predictive capability of this new combined formulation should be assessed for various spray combustion conditions with different fuel or more complex geometry. Additionally, model development with application in the large eddy simulation would be another promising way for accurate prediction of complex two-phase turbulent spray flows.

Appendix

A. Nomenclature

Symbol	Unit	Description
A	m^2	Surface area of control volume
B_M		Spalding mass transfer number
B_T		Spalding heat transfer number
C_p	$\mathrm{J\ kg^{-1}\ K^{-1}}$	Specific heat capacity at constant pressure
C_D		Drag coefficient
C_ϕ		Ratio of mechanical to scalar time-scales
$D_{\phi,m}$	$\mathrm{m^2\ s^{-1}}$	Mixture diffusion coefficient of species ϕ
E		Equivalence ratio
f^*		One-point one-time fine-grained probability density function
F		Mass density function
h	$\mathrm{J\ kg^{-1}}$	Total enthalpy
$\Delta h^o_{f,\alpha}$	$\mathrm{J\ kg^{-1}}$	Mass formation enthalpy of species α
k	$\mathrm{m^2\ s^{-2}}$	Turbulent kinetic energy
Le		Lewis number
L_V	$\mathrm{J\ kg^{-1}}$	Latent heat of evaporation
Nu		Nusselt number
p	Pa	Pressure
Pr		Prandtl number
$\overline{R}$	$\mathrm{J\ mol^{-1}\ K^{-1}}$	Universal gas constant
Re		Reynolds number
R_0		Initial droplet radius
Sc		Schmit number
S_e	$\mathrm{J\ m^{-3}\ s^{-1}}$	Spray source term for energy
Sh		Sherwood number
S_k	$\mathrm{kg\ m^{-1}\ s^{-3}}$	Spray source term for turbulent kinetic energy
S_m	$\mathrm{kg\ m^{-2}\ s^{-2}}$	Spray source term for momentum
S_v	$\mathrm{kg\ m^{-3}\ s^{-1}}$	Spray source term for mass
T	K	Temperature
T_b	K	Boiling temperature of liquid phase
t	s	Time

$\mathbf{U}$	m s^{-1}	Gas velocity
$\mathbf{V}$	m s^{-1}	Gas velocity in sample space
$\mathbf{V}_{\mathrm{d}}$	m s^{-1}	Droplet velocity
W_α	kg mol^{-1}	Molecular weight of species α
$\mathbf{x}$	m	Position
X_α		Mole fraction of species α
Y_{Fs}		Mass fraction of fuel vapor at droplet surface
Y_{P}		Reaction progress variable
Y_α		Mass fraction of species α
ξ		Mixture fraction
ζ		Variable for mixture fraction in sample space
η		Variable for reaction progress variable in sample space
θ		Variable for enthalpy in sample space
χ	s^{-1}	Scalar dissipation rate
ϵ	m^2 s^{-3}	Dissipation rate of turbulent kinetic energy
$\dot{\omega}_\alpha$	kg m^{-3} s^{-1}	Specific chemical reaction rate of species α
δ		Kronecker symbol
Γ_ϕ		Exchange coefficient for variable ϕ
ρ	kg m^{-3}	Gas density
λ	J m^{-1} K^{-1} s^{-1}	Thermal conductivity of gas mixture
μ	kg m^{-1} s^{-1}	Dynamic viscosity of gas mixture
ν_t	m^2 s^{-1}	Turbulent kinematic viscosity

Subscript Description

Symbol	Quantity
g	Gas phase
l	Liquid phase
d	Droplet
t	Turbulent
atm	Atmospheric
0	Initial condition
∞	Far field condition
m	Mixture

B. Acknowledgements

Firstly, I would like to express my sincere gratitude to my supervisor, Prof. E. Gutheil for her constant guidance, patience and encouragement. Without her continuous support and help, this dissertation would not have been possible. Prof. E. Gutheil gave me this opportunity to study in this excellent research group and extend my research interests in the field of numerical combustion. Her excellent guidance makes my PhD experience productive and simulating. And she also supported me to attend different conferences through which I learned a lot and greatly practised my presentation skills. I appreciate all her contributions of time and ideas during the discussion and correction of my papers, presentations and this thesis, and in these processes, she helped me improve a lot my scientific writing. Also, no matter if I met problems in work or life, she would always help me with her best effort.

I want to thank to all my colleagues: Dr. X. Cui, Dr. R. M. Humza, Dr. S. Reddy, Dr. L. Cao, Dr. H. Grosshans, Dr. H. Olguin, O. Norena, A. Sanches, A. Farnoud. Their kind help and good discussion that we had in the group seminar or during lunch time, made these four years a splendid and memorable experience in my life.

Special thanks to O. Norena and A. Sanches for proof reading this thesis, and Dr. Hai-Wen Ge for giving me lots of valuable suggestions at the beginning of my PhD study. My appreciation also go to the secretary, E. Vogel, and the computer system administrator, M. Trunk, for their kindness help, which makes my study and life in this group much easier.

I gratefully acknowledge the financial support from the China Scholarship Council and the DFG through the Heidelberg Graduate school of Mathematical and Computational Methods for the Sciences (HGS-MathComp).

Finally, I wish to give special thanks to my parents (Mr. Jian-min Hu and Mrs. Shun-rong Li), and my girlfriend (Hui-ling Chen) for their love and constant support. Thank you for being with me and giving me strength to get through all the difficulties that I confronted throughout my PhD pursuit in Germany.

Bibliography

[1] REN21 Renewables 2014 Global Status Report. Total world energy consumption by source 2013. http://www.ren21.net/status-of-renewables/global-status-report/, 2014.

[2] International Energy Agency. Key World Energy Statistic 2014. *International Energy Agency Publications,* http://www.iea.org/, 2014.

[3] U. S. DOE Energy Information Administration. World energy consumption outlook by source in 2013. https://en.wikipedia.org/wiki/Energy-development, 2013.

[4] H. Lee, W. C. Clark, and C. Devereaux. Biofuels and Sustainable Development. *An Executive Session on Grand Challenges of the Sustainability Transition*, San Servolo Island, Venice, 19–20 May, 2008.

[5] International Energy Agency. Technology Roadmap: Biofuels for Transport. *International Energy Agency Publications,* http://www.iea.org/, 2011.

[6] URL: `http://biofuel.org.uk/`.

[7] London Royal Society. Sustainable biofuels: prospects and challenges. 2008.

[8] D. Pimentel and T. Patzek. Ethanol production using corn, switchgrass and wood and biodiesel production using soybean and sunflower. *Natural Resources and Research*, **14**: 65 –76, 2005.

[9] A. K. Agarwal. Biofuels (alcohols and biodiesel) applications as fuels for internal combustion engines. *Progress in Energy and Combustion Science*, **33**: 233–271, 2007. ISSN: 0360-1285.

[10] REN21 Renewable Energy Policy Network for the 21st Century. Renewables 2015 Global Status Report. http://www.ren21.net/status-of-renewables/global-status-report/, 2015.

[11] J. Warnatz, U. Mass, and R. W. Dibble. *Combustion: Physical and Chemical Fundamentals, Modeling and Simulation, Experiments, Pollutant Formation,* 4th Edition. Springer Berlin Heidelberg, 2006.

[12] A. H. Lefebvre and D. R. Ballal. *Gas Turbine Combustion: Alternative Fuels and Emissions,* Third Edition. CRC Press, 2010.

[13] G. P. Merker, C. Schwarz, G. Stiesch, and F. Otto. *Simulating Combustion: Simulation of combution and pollutant formation for engine-development.* Springer Berlin Heidelberg, 2006.

[14] C. E. Baukal. *Industrial Combustion Pollution and Control.* CRC Press, 2003.

[15] URL: `https://en.wikipedia.org/wiki/List_of_gasoline_additives`.

[16] S. B. Pope. Small scales, many species and the manifold challenges of turbulent combustion. *Proceedings of the Combustion Institute*, **34**: 1–31, 2013.

[17] N. Peters. *Turbulent Combustion.* Cambridge University Press, 2000.

[18] C. T. Crowe and J. D. Schwarzkopf and M. Sommerfeld and Y. Tsuji. *Multiphase flows with droplets and particles, Second Edition.* CRC Press, 2011.

[19] A. Williams. *Combustion of Liquid Fuel Sprays.* Butterworth-Heinemann, 1990.

[20] G. Stiesch. *Modeling Engine Spray and Combustion Processes.* Springer Berlin Heidelberg, 2003.

[21] J. Reveillon and F.-x. Demoulin. Effects of the preferential segregation of droplets on evaporation and turbulent mixing. *Journal of Fluid Mechanics*, **583**: 273–302, 2007. ISSN: 1469-7645.

[22] P. Jenny, D. Roekaerts, and N. Beishuizen. Modeling of turbulent dilute spray combustion. *Progress in Energy and Combustion Science*, **38**: 846 –887, 2012.

[23] Y. Baba and R. Kurose. Analysis and flamelet modelling for spray combustion. *Journal of Fluid Mechanics*, **612**: 45–79, 2008.

[24] M. P. Musculus, P. C. Miles, and L. M. Pickett. Conceptual models for partially premixed low-temperature diesel combustion. *Progress in Energy and Combustion Science*, **39**: 246 –283, 2013.

[25] S. B. Pope. PDF methods for turbulent reactive flows. *Progress in Energy and Combustion Science*, **11**: 119 –192, 1985.

[26] D. C. Haworth. Progress in probability density function methods for turbulent reacting flows. *Progress in Energy and Combustion Science*, **36**: 168 –259, 2010.

[27] B. Naud. *PDF modeling of turbulent sprays and flames using a particle stochastic approach.* PhD Thesis. TU Delft, 2003.

[28] J. D. Gounder, A. Kourmatzis, and A. R. Masri. Turbulent piloted dilute spray flames: Flow fields and droplet dynamics. *Combustion and Flame*, **159**: 3372 –3397, 2012.

[29] X. Jiang, G. Siamas, K. Jagus, and T. Karayiannis. Physical modelling and advanced simulations of gas - liquid two-phase jet flows in atomization and sprays. *Progress in Energy and Combustion Science*, **36**: 131 –167, 2010.

[30] S. B. Pope. *Turbulent Flows*. Cambridge University Press, 2000.

[31] K. Luo, H. Pitsch, M. Pai, and O. Desjardins. Direct numerical simulations and analysis of three-dimensional n-heptane spray flames in a model swirl combustor. *Proceedings of the Combustion Institute*, **33**: 2143 –2152, 2011.

[32] T. Kitano, J. Nishio, R. Kurose, and S. Komori. Effects of ambient pressure, gas temperature and combustion reaction on droplet evaporation. *Combustion and Flame*, **161**: 551 –564, 2014.

[33] J. Réveillon and L. Vervisch. Spray vaporization in nonpremixed turbulent combustion modeling: a single droplet model. *Combustion and Flame*, **121**: 75 –90, 2000.

[34] G. Borghesi, E. Mastorakos, and R. S. Cant. Complex chemistry DNS of n-heptane spray autoignition at high pressure and intermediate temperature conditions. *Combustion and Flame*, **160**: 1254 –1275, 2013.

[35] Y. Xu and S. Subramaniam. Effect of particle clusters on carrier flow turbulence: A direct numerical simulation study. *Flow, Turbulence and Combustion*, **85**: 735–761, 2010.

[36] R. O. Fox. Large-Eddy-Simulation Tools for Multiphase Flows. *Annual Review of Fluid Mechanics*, **44**: 47–76, 2012.

[37] W. Jones, S. Lyra, and S. Navarro-Martinez. Large Eddy Simulation of a swirl stabilized spray flame. *Proceedings of the Combustion Institute*, **33**: 2153 –2160, 2011.

[38] H. Pitsch. Large-eddy simulation of turbulent combustion. *Annual Review of Fluid Mechanics*, **38**: 453–482, 2006.

[39] P. Moin. Advances in Large-eddy simulation methodology for complex flows. *International Journal of Heat and Fluid Flow*, **23**: 710–720, 2002.

[40] D. Veynante and L. Vervisch. Turbulent combustion modeling. *Progress in Energy and Combustion Science*, **28**: 193–266, 2002. ISSN: 0360-1285.

[41] H. Enwald, E. Peirano, and A.-E. Almstedt. Eulerian two-phase flow theory applied to fluidization. *International Journal of Multiphase Flow*, **22**: 21 –66, 1996.

[42] E. Loth. *Computational fluid dynamics of bubbles, drops and particles*. Cambridge University Press, 2009.

[43] M. G. Pai and S. Subramaniam. Modeling interphase turbulent kinetic energy transfer in Lagrangian-Eulerian spray computations. *Atomization and Sprays*, **16**: 807–826, 2006.

[44] P. C. Le Clercq and J. Bellan. Direct numerical simulation of a transitional temporal mixing layer laden with multicomponent-fuel evaporating drops using continuous thermodynamics. *Physics of Fluids*, **16**: 1884–1907, 2004.

[45] S. Subramaniam. Lagrangian-Eulerian methods for multiphase flows. *Progress in Energy and Combustion Science*, **39**: 215 –245, 2013.

[46] K. K. Kuo and R. Acharya. *Fundamentals of turbulent and multiphase combustion.*

[47] F. Jaegle and J.-M. Senoner and M. García and F. Bismes and R. Lecourt and B. Cuenot and T. Poinsot. Eulerian and Lagrangian spray simulations of an aeronautical multipoint injector. *Proceedings of the Combustion Institute*, **33**: 2099 –2107, 2011.

[48] R. Fox. *Computational models for turbulent reacting flows.* Cambridge University Press, UK, 2003.

[49] T. Poinsot and D. Veynante. *Theoretical and Numerical Combustion, Second Edition.* R.T. Edwards, Inc., 2005.

[50] K. Bray and J. Moss. A unified statistical model of the premixed turbulent flame. *Acta Astronautica*, **4**: 291 –319, 1977.

[51] P. A. Libby and K. Bray. Countergradient diffusion in premixed turbulent flames. *AIAA Journal*, **15**: 1186 –1193, 1981.

[52] K. Bray. Turbulent flows with premixed reactants. In: P.A. Libby & F.A. Williams, eds., *Turbulent Reacting Flows*, 115 –183, Springer-Verlag, New York, 1980.

[53] K. Bray, M. Champion, and P. Libby. The interaction between turbulence and chemistry in premixed turbulent flames. In: R. Borghi and S.N. Murthy, eds., *Turbulent Reacting Flows*, 541 –563, Lecture Notes in Engineering, Springer Verlag, 1989.

[54] N. Peters. *Turbulent Combustion.* Cambridge University Press, 2000.

[55] K. N. C. Bray, P. A. Libby, and J. B. Moss. Flamelet crossing frequencies and mean reaction rates in premixed turbulent combustion. *Combustion Science and Technology*, **41**: 143–172, 1984.

[56] K. N. C. Bray and P. A. Libby. Passage times and flamelet crossing frequencies in premixed turbulent combustion. *Combustion Science and Technology*, **47**: 253–274, 1986.

[57] M. Chrigui, A. Zghal, A. Sadiki, and J. Janicka. Spray evaporation and dispersion of n-heptane droplets within premixed flame. *Heat and Mass Transfer*, **46**: 869–880, 2010.

[58] M. Chrigui, J. Gounder, A. Sadiki, J. Janicka, and A. Masri. Acetone droplet behavior in reacting and non-reacting turbulent flow. *Flow, Turbulence and Combustion*, **90**: 419–447, 2013.

[59] A. Y. Klimenko and R. W. Bilger. Conditional moment closure for turbulent combustion. *Progress in Energy and Combustion Science*, **25**: 595–687, 1999.

[60] R. W. Bilger. Conditional moment closure for turbulent reacting flow. *Physics of Fluids A*, **5**: 1993.

[61] N. Smith, R. Bilger, and J.-Y. Chen. Modelling of nonpremixed hydrogen jet flames using a conditional moment closure method. *Proceedings of the Combustion Institute*, **24**: 263 –269, 1992.

[62] Kuznetsov, V. R. and Sabelnikov, V. A. *Turbulence and Combustion*. In: P.A. Libby (Ed.), English ed., Hemisphere, New York, 1990.

[63] E. E. O'Brien and T. Jiang. The conditional dissipation rate of an initially binary scalar in homogeneous turbulence. *Physics of Fluids A*, **3**: 3121 –3123, 1991.

[64] S. S. Girimaji. On the modeling of scalar diffusion in isotropic turbulence. *Physics of Fluids A*, **4**: 2529 –2537, 1992.

[65] C. B. Devaud, R. W. Bilger, and T. Liu. A new method of modeling the conditional scalar dissipation rate. *Physics of Fluids*, **16**: 2004 –2011, 2004.

[66] M. Mortensen and R. W. Bilger. Derivation of the conditional moment closure equations for spray combustion. *Combustion and Flame*, **156**: 62–72, 2009.

[67] P. Schroll, E. Mastorakos, and R. W. Bilger. Simulations of spark ignition of a swirling n-heptane spray flame with conditional moment closure. *AIAA paper 2010-614*, 2010.

[68] G. Borghesi, E. Mastorakos, C. B. Devaud, and R. W. Bilger. Modeling evaporation effects in conditional moment closure for spray autoignition. *Combustion Theory and Modelling*, **15**: 725–752, 2011.

[69] N. Frapolli, M. Bolla, K. Boulouchos, and Y. Wright. Simulations of in-cylinder processes in a diesel engine operated with post-injections using an extended CMC model. *SAE Technical Paper 2014-01-2571*, 2014.

[70] R. Cabra, J.-Y. Chen, R. Dibble, A. Karpetis, and R. Barlow. Lifted methaneâ€“air jet flames in a vitiated coflow. *Combustion and Flame*, **143**: Special Issue to Honor Professor Robert W. Bilger on the Occasion of His Seventieth Birthday, 491 –506, 2005.

[71] N. Peters. Laminar diffusion flamelet models in non-premixed turbulent combustion. *Progress in Energy and Combustion Science*, **10**: 319 –339, 1984.

[72] F. Williams. *Combustion Theory*. Westview Press, 1994.

[73] R. Borghi. In: *On the structure and morphology of turbulent premixed flames.* In: *Recent Advances in Aeronautical Science*. Ed. by C. Bruno and C. Casci. Pergamon, 1985.

[74] N. Peters. Length Scales in Laminar and Turbulent Flames in: Numerical Approaches to Combustion Modeling. *Progress in Astronautics and Aeronautics*, **135**: 155–182, 1991.

[75] H. Olguin and E. Gutheil. Influence of evaporation on spray flamelet structures. *Combustion and Flame*, **161**: 987–996, 2014.

[76] K. Luo, J. Fan, and K. Cen. New spray flamelet equations considering evaporation effects in the mixture fraction space. *Fuel*, **103**: 1154 –1157, 2013.

[77] M. Stöllinger, B. Naud, D. Roekaerts, N. Beishuizen, and S. Heinz. PDF modeling and simulations of pulverized coal combustion - Part 1: Theory and modeling. *Combustion and Flame*, **160**: 384 –395, 2013.

[78] H.-W. Ge, I. Düwel, H. Kronemayer, R. W. Dibble, E. Gutheil, C. Schulz, and J. Wolfrum. Laser-based experimental and Monte Carlo PDF numerical investigation of an ethanol/air spray flame. *Combustion Science and Technology*, **180**: 1529–1547, 2008.

[79] C. Hollmann and E. Gutheil. Modeling of turbulent spray diffusion flames including detailed chemistry. *Symposium (International) on Combustion*, **26**: 1731–1738, 1996.

[80] H. Versteeg and W. Malalasekera. *An Introduction to Computational Fluid Dynamics: The Finite Volume Method*. Prentice Hall, 2007.

[81] G. Continillo and W. A. Sirignano. Counterflow spray combustion modeling. *Combustion and Flame*, **81**: 325 –340, 1990.

[82] T. S. Lundgren. Model equation for nonhomogeneous turbulence. *Physics of Fluids*, **12**: 485–497, 1969.

[83] C. Dopazo and E. E. O'Brien. An approach to the autoignition of a turbulent mixture. *Acta Astronautica*, **1**: 1239 –1266, 1974.

[84] H.-W. Ge and E. Gutheil. Simulation of a turbulent spray flame using coupled PDF gas phase and spray flamelet modeling. *Combustion and Flame*, **153**: 173 –185, 2008.

[85] Y. Hu and E. Gutheil. Numerical Simulations of Turbulent Poly-disperse Acetone Spray Flows Using A Transported Joint Probability Density Function Method. *Atomization and Sprays*, **26**: 275–299, 2016.

[86] J. Xu and S. B. Pope. PDF calculations of turbulent nonpremixed flames with local extinction. *Combustion and Flame*, **123**: 281 –307, 2000.

[87] C. Heye, V. Raman, and A. R. Masri. Influence of spray/combustion interactions on auto-ignition of methanol spray flames. *Proceedings of the Combustion Institute*, **35**: 1639 –1648, 2015.

[88] G. Bulat, W. Jones, and A. Marquis. NO and CO formation in an industrial gas-turbine combustion chamber using LES with the Eulerian sub-grid PDF method. *Combustion and Flame*, **161**: 1804 –1825, 2014.

[89] E. H. Kung. *PDF-based modeling of autoignition and emissions for advanced direct-injection engines*. PhD thesis. The Pennsylvania State University, 2008.

[90] M. Stöllinger and S. Heinz. Evaluation of scalar mixing and time scale models in PDF simulations of a turbulent premixed flame. *Combustion and Flame*, **157**: 1671 –1685, 2010.

[91] R. Lindstedt and E. Vaos. Transported PDF modeling of high-Reynolds-number premixed turbulent flames. *Combustion and Flame*, **145**: 495 –511, 2006.

[92] R. D. Meester, B. Naud, U. Maas, and B. Merci. Transported scalar PDF calculations of a swirling bluff body flame ('SM1') with a reaction diffusion manifold. *Combustion and Flame*, **159**: 2415 –2429, 2012.

[93] R. R. Cao, H. Wang, and S. B. Pope. The effect of mixing models in PDF calculations of piloted jet flames. *Proceedings of the Combustion Institute*, **31**: 1543 –1550, 2007.

[94] P. P. Popov and S. B. Pope. Large eddy simulation/probability density function simulations of bluff body stabilized flames. *Combustion and Flame*, **161**: 3100 –3133, 2014.

[95] H.-W. Ge and E. Gutheil. PDF simulation of turbulent spray flows. *Atomization and sprays*, **16**: 531–542, 2006.

[96] S. Bhattacharjee and D. C. Haworth. Simulations of transient n-heptane and n-dodecane spray flames under engine-relevant conditions using a transported PDF method. *Combustion and Flame*, **160**: 2083 –2102, 2013.

[97] C. Heye, V. Raman, and A. R. Masri. LES/probability density function approach for the simulation of an ethanol spray flame. *Proceedings of the Combustion Institute*, **34**: 1633 –1641, 2013.

[98] G. Anand and P. Jenny. Stochastic modeling of evaporating sprays within a consistent hybrid joint PDF framework. *Journal of Computational Physics*, **228**: 2063–2081, 2009.

[99] M. L. Hack, J. Schmoker, and P. Jenny. A joint probability density function (PDF) model for turbulent premixed combustion. *Proceedings of the European Combustion Meeting*, 2009.

[100] D. C. Haworth. A probability density function/flamelet method for partially premixed turbulent combustion. *Center for Turbulence Research, Proceedings of the Summer Program*, 2000.

[101] A. R. Masri. `http://sydney.edu.au/engineering/aeromech/thermofluids/database.htm`.

[102] K. K. Kuo. *Principles of combustion*. John Wiley & Sons, Inc., 2005.

[103] S. B. Pope. A Monte Carlo Method for the PDF Equations of Turbulent Reactive Flow. *Combustion Science and Technology*, **25**: 159–174, 1981.

[104] S. S. Penner. *Chemistry problems in jet propulsion*. Pergamon Press, 1957.

[105] J. R. Kee, J. Warnatz, and J. A. Miller. A FORTRAN Computer Code Package for the Evaluation of Gas-Phase Viscosities, Conductivities, and Diffusion Coefficients. *Sandia National Laboratories Report, No. SAND83-8209*, 1988.

[106] S. Mathur, P. K. Tondon, and S. C. Saxena. Thermal conductivity of binary, ternary and quaternary mixtures of rare gases. *Molecular Physics*, **12**: 569–579, 1967.

[107] J. O. Hirschfelder, C. F. Curtiss, and B. R. B. *Molecular theory of gases and liquids*. John Wiley & Sons, Inc., 1954.

[108] R. J. Kee, G. Dixon-lewis, J. Warnatz, M. E. Coltrin, and J. A. Miller. *A Fortran computer code package for the evaluation of gas-phase, multicomponent transport properties*. Tech. rep. 1986.

[109] F. G. Schmitt. About Boussinesq's turbulent viscosity hypothesis: historical remarks and a direct evaluation of its validity. *Comptes Rendus Mécanique*, **335**: 617 –627, 2007.

[110] C. Hollmann. *Modellierung turbulenter Sprayflammen unter Verwendung detaillierter chemischer Reaktionsmechanismen*. PhD Thesis. Ruprecht-Karls-Universität Heidelberg, 1997.

[111] C. K. Law. *Combustion Physics*. Cambridge University Press, 2006.

[112] T. Lu and C. K. Law. Toward accommodating realistic fuel chemistry in large-scale computations. *Progress in Energy and Combustion Science*, **35**: 192 –215, 2009.

[113] T. Lu and C. K. Law. Linear time reduction of large kinetic mechanisms with directed relation graph: n-Heptane and iso-octane. *Combustion and Flame*, **144**: 24 –36, 2006.

[114] T. Lu and C. K. Law. On the applicability of directed relation graphs to the reduction of reaction mechanisms. *Combustion and Flame*, **146**: 472 –483, 2006.

[115] J. D. Ramshaw. Partial chemical equilibrium in fluid dynamics. *Physics of Fluids*, **23**: 1980.

[116] U. Maas and S. Pope. Simplifying chemical kinetics: Intrinsic low-dimensional manifolds in composition space. *Combustion and Flame*, **88**: 239 –264, 1992.

[117] J. Nafe and U. Maas. A general algorithm for improving ILDMs. *Combustion Theory and Modelling*, **6**: 697 –709, 2002.

[118] D. Goussis and S. Lam. A study of homogeneous methanol oxidation kinetics using CSP. *Twenty-Fourth Symposium (International) on Combustion*, **24**: 113 –120, 1992.

[119] S. H. Lam and D. A. Goussis. The CSP method for simplifying kinetics. *International Journal of Chemical Kinetics*, **26**: 461 –486, 1994.

[120] E. Knudsen and H. Pitsch. Capabilities and limitations of multi-regime flamelet combustion models. *Combustion and Flame*, **159**: 242 –264, 2012.

[121] E. Knudsen and H. Pitsch. A general flamelet transformation useful for distinguishing between premixed and non-premixed modes of combustion. *Combustion and Flame*, **156**: 678 –696, 2009.

[122] P.-D. Nguyen, L. Vervisch, V. Subramanian, and P. Domingo. Multidimensional flamelet-generated manifolds for partially premixed combustion. *Combustion and Flame*, **157**: 43 –61, 2010.

[123] P. Domingo, L. Vervisch, and D. Veynante. Large-eddy simulation of a lifted methane jet flame in a vitiated coflow. *Combustion and Flame*, **152**: 415 –432, 2008.

[124] M. Ihme and H. Pitsch. Prediction of extinction and reignition in nonpremixed turbulent flames using a flamelet/progress variable model: 1. A priori study and presumed {PDF} closure. *Combustion and Flame*, **155**: 70 –89, 2008.

[125] M. Ihme and H. Pitsch. Modeling of radiation and nitric oxide formation in turbulent nonpremixed flames using a flamelet/progress variable formulation. *Physics of Fluids*, **20**: 055110, 2008.

[126] M. Ihme and Y. C. See. Prediction of autoignition in a lifted methane/air flame using an unsteady flamelet/progress variable model. *Combustion and Flame*, **157**: 1850 –1862, 2010.

[127] J. van Oijen and L. de Goey. Modelling of premixed laminar flames using flamelet-generated manifolds. *Combustion Science and Technology*, **161**: 113–137, 2000.

[128] W. Ramaekers, J. van Oijen, and L. de Goey. A priori testing of flamelet generated manifolds for turbulent partially premixed methane/air flames. *Flow, Turbulence and Combustion*, **84**: 439–458, 2010.

[129] O. Gicquel, N. Darabiha, and D. Thévenin. Liminar premixed hydrogen/air counterflow flame simulations using flame prolongation of ILDM with differential diffusion. *Proceedings of the Combustion Institute*, **28**: 1901 –1908, 2000.

[130] B. Fiorina, O. Gicquel, L. Vervisch, S. Carpentier, and N. Darabiha. Approximating the chemical structure of partially premixed and diffusion counterflow flames using FPI flamelet tabulation. *Combustion and Flame*, **140**: 147 –160, 2005.

[131] P. Domingo, L. Vervisch, S. Payet, and R. Hauguel. DNS of a premixed turbulent V flame and LES of a ducted flame using a FSD-PDF subgrid scale closure with FPI-tabulated chemistry. *Combustion and Flame*, **143**: Special Issue to Honor Professor Robert W. Bilger on the Occasion of His Seventieth Birthday, 566 –586, 2005.

[132] P. Domingo, L. Vervisch, and J. Réveillon. DNS analysis of partially premixed combustion in spray and gaseous turbulent flame-bases stabilized in hot air. *Combustion and Flame*, **140**: 172 –195, 2005.

[133] C. Hollmann and E. Gutheil. Flamelet-modeling of turbulent spray diffusion flames based on a laminar spray flame library. *Combustion Science and Technology*, **135**: 175–192, 1998.

[134] S. Li. Spray stagnation flames. *Progress in Energy and Combustion Science*, **23**: 303 –347, 1997.

[135] E. Gutheil and W. Sirignano. Counterflow spray combustion modeling with detailed transport and detailed chemistry. *Combustion and Flame*, **113**: 92–105, 1998.

[136] Y. Hu, H. Olguin, and E. Gutheil. Combined Transported Joint Probability Density Function and Spray Flamelet Approach for the Simulation of Turbulent Dilute Ethanol Spray Flames. *13th Triennial International Conference on Liquid Atomization and Spray Systems*, Tainan, Taiwan, 23–27 August, 2015.

[137] C. D. Pierce and P. Moin. Progress-variable approach for large-eddy simulation of non-premixed turbulent combustion. *Journal of Fluid Mechanics*, **504**: 73–97, 2004.

[138] E. Knudsen, Shashank, and H. Pitsch. Modeling partially premixed combustion behavior in multiphase LES. *Combustion and Flame*, **162**: 159 –180, 2015.

[139] J. Janicka and W. Kollmann. A two-variables formalism for the treatment of chemical reactions in turbulent H2-Air diffusion flames. *Seventeenth Symposium (International) on Combustion*, **17**: 421 –430, 1979.

[140] M. Ihme, C. M. Cha, and H. Pitsch. Prediction of local extinction and re-ignition effects in non-premixed turbulent combustion using a flamelet/progress variable approach. *Proceedings of the Combustion Institute*, **30**: 793 –800, 2005.

[141] R. Miller and J. Bellan. On the validity of the assumed probability density function method for modeling binary mixing/reaction of evaporated vapor in gas/liquid-droplet turbulent shear flow. *Symposium (International) on Combustion*, **27**: Twenty-Seventh Sysposium (International) on Combustion Volume One, 1065 –1072, 1998.

[142] R. S. Miller and J. Bellan. Direct numerical simulation and subgrid analysis of a transitional droplet laden mixing layer. *Physics of Fluids*, **12**: 2000.

[143] N. S. A. Smith, C. C. M., P. H., and O. J. C. Simulation and modeling of the behavior of conditional scalar moments in turbulent spray combustion. *Center for Turbulence Research, Proceedings of the Summer Program*, 207–218, 2000.

[144] S. B. Pope. The Statistical Theory of Turbulent Flames. *Philosophical Transactions of the Royal Society of London A: Mathematical, Physical and Engineering Sciences*, **291**: 529–568, 1979.

[145] H.-W. Ge, Y. Hu, and E. Gutheil. Joint gas-phase velocity-scalar PDF modeling for turbulent evaporating spray flows. *Combustion Science and Technology*, **184**: 1664–1679, 2012.

[146] S. Heinz. *Statistical mechanics of turbulent flows*. Springer, Berlin, 2003.

[147] Y. Hu, H. Olguin, and E. Gutheil. Transported Joint PDF Simulation of Turbulent Spray Flames with a Novel Spray Flamelet/Progress Variable Approach. *Combustion and Flame*, 2015, submitted.

[148] C. Dopazo. Recent developments in PDF methods. In: P.A. Libby & F.A. Williams, eds., *Turbulent Reacting Flows*, 375 –474, New York: Academic Press, 1994.

[149] R. M. Humza, Y. Hu, and E. Gutheil. "Probability density function modeling of turbulent spray combustion". In: *Experiments and Numerical Simulations of Turbulent Combustion of Diluted Sprays*. Ed. by B. Merci and E. Gutheil. Vol. 19. ERCOFTAC. Springer International Publishing, 2014. 130–153. ISBN: 978-3-319-04677-8.

[150] J. Villermaux and J. C. Devillon. Représentation de la coalescence et de la redispersion des domaines de ségrégation dans un fluide par un modéle d'interaction phénoménologique. In: Proceedings of the 2nd international symposium on chemical reaction engineering, 1972.

[151] J. Janicka, W. Kolbe, and K. W. Closure of the transport equation for the probability density function of turbulent scalar fields. *Journal of Non-Equilibrium Thermodynamics*, **4**: 47–66, 1979.

[152] R. L. Curl. Dispersed phase mixing: I. Theory and effects of simple reactors. *Chemical engineering progress symposium series*, **9**: 175 –181, 1963.

[153] S. Subramaniam and S. B. Pope. A mixing model for turbulent reactive flows based on Euclidean minimum spanning trees. *Combustion and Flame*, **115**: 487 –514, 1998.

[154] S. Mitarai, J. J. Riley, and G. Kosály. Testing of mixing models for Monte Carlo probability density function simulations. *Physics of Fluids*, **17**: 047101, –, 2005.

[155] S. B. Pope. A model for turbulent mixing based on shadow-position conditioning. *Physics of Fluids*, **25**: 110803, –, 2013.

[156] H. Chen, S. Chen, and R. H. Kraichnan. Probability distribution of a stochastically advected scalar field. *Physical Review Letters*, **63**: 2657–2660, 1989.

[157] R. O. Fox. Improved Fokker-Planck model for the joint scalar, scalar gradient PDF. *Physics of Fluids*, **6**: 1994.

[158] L. Valiño and C. Dopazo. A binomial Langevin model for turbulent mixing. *Physics of Fluids A*, **3**: 1991.

[159] D. W. Meyer and P. Jenny. A mixing model for turbulent flows based on parameterized scalar profiles. *Physics of Fluids*, **18**: 035105, –, 2006.

[160] D. W. Meyer and P. Jenny. Micromixing models for turbulent flows. *Journal of Computational Physics*, **228**: 1275 –1293, 2009.

[161] H. Hu Y. Olguin and E. Gutheil. Transported Joint PDF Simulation of a Turbulent Ethanol Spray Flame Combined with a Spray Flamelet Model. *25th ICDERS*, Leeds, UK, 2–7 August, 2015.

[162] M. R. Maxey and J. J. Riley. Equation of motion for a small rigid sphere in a nonuniform flow. *Physics of Fluids*, **26**: 1983.

[163] I. Iliopoulos and T. J. Hanratty. A non-Gaussian stochastic model to describe passive tracer dispersion and its comparison to a direct numerical simulation. *Physics of Fluids*, **16**: 2004.

[164] V. Armenio and V. Fiorotto. The importance of the forces acting on particles in turbulent flows. *Physics of Fluids*, **13**: 2001.

[165] L. Schiller and A. Z. Naumann. Über die grundlegenden Berechnungen bei der Schwerkraftaufbereitung. *Ver. Deut. Ing.*, **77**: 318–320, 1933.

[166] S. Laín and M. Sommerfeld. Euler/Lagrange computations of pneumatic conveying in a horizontal channel with different wall roughness. *Powder Technology*, **184**: 76 –88, 2008.

[167] Y. Hu and E. Gutheil. Transported Joint PDF Modeling of Poly-disperse Turbulent Acetone Spray Flows. *26th European Conference on Liquid Atomization and Spray Systems*, Bremen, Germany, 8–10 September, 2014.

[168] C. K. Law. Recent advances in droplet vaporization and combustion. *Progress in Energy and Combustion Science*, **8**: 171 –201, 1982.

[169] G. M. Faeth. Evaporation and combustion of sprays. *Progress in Energy and Combustion Science*, **9**: 1 –76, 1983.

[170] W. A. Sirignano. *Fluid dynamics and transport of droplets and sprays*. Cambridge University Press, 1999.

[171] S. S. Sazhin. Advanced models of fuel droplet heating and evaporation. *Progress in Energy and Combustion Science*, **32**: 162 –214, 2006.

[172] S. S. Sazhin, T. Kristyadi, W. A. Abdelghaffar, and M. R. Heikal. Models for fuel droplet heating and evaporation: Comparative analysis. *Fuel*, **85**: 1613 – 1630, 2006.

[173] S. K. Aggarwal, A. Tong, and W. A. Sirignano. A comparison of vaporization models in spray calculations. *AIAA Journal*, **22**: 1448 –1457, 1984.

[174] B. Abramzon and W. A. Sirignano. Droplet vaporization model for spray combustion calculations. *International Journal of Heat and Mass Transfer*, **32**: 1605 –1618, 1989.

[175] R. Miller, K. Harstad, and J. Bellan. Evaluation of equilibrium and non-equilibrium evaporation models for many-droplet gas-liquid flow simulations. *International Journal of Multiphase Flow*, **24**: 1998.

[176] G. L. Hubbard, V. E. Denny, and A. F. Mills. Droplet evaporation: Effects of transients and variable properties. *International Journal of Heat and Mass Transfer*, **18**: 1003 –1008, 1975.

[177] J. Bellan and M. Summerfield. Theoretical examination of assumptions commonly used for the gas phase surrounding a burning droplet. *Combustion and Flame*, **33**: 107 –122, 1978.

[178] W. E. Ranz and W. R. Marshall. Evaporation from drops: Part I. *Chemical Engineering Progress*, **48**: 141–146, 1952.

[179] W. E. Ranz and W. R. Marshall. Evaporation from drops: Part II. *Chemical Engineering Progress*, **48**: 173–180, 1952.

[180] P. Durand, M. Gorokhovski, and R. Borghi. An application of the probability density function model to diesel engine combustion. *Combustion Science and Technology*, **144**: 47–78, 1999.

[181] S. V. Patankar. *Numerical Heat Transfer and Fluid Flow*. Hemisphere, New York, 1980.

[182] S. V. Patankar and D. B. Spalding. A calculation procedure for heat, mass and momentum transfer in three-dimensional parabolic flows. *International Journal of Heat Mass Transfer*, **15**: 1787–1972, 1972.

[183] S. K. Srivatsa. *CORA2: A computer code for axi-symmetrical combustion chambers*. (May 1977), CHAM Ltd.

[184] J. J. D. Anderson. *Computational Fluid Dynamics : The Basics with Applications*. McGraw-Hill, Inc., 1995.

[185] F. H. Harlow and J. E. Welch. Numerical calculation of time – dependent viscous incompressible flow of fluid with free surface. *Physics of Fluids*, **8**: 2182–2189, 1965.

[186] L. H. Thomas. *Elliptic problems in linear differential equations over a network*. Watson Sci. Comput. Lab Report, Columbia University, New York, 1949.

[187] P. Jenny, S. Pope, M. Muradoglu, and D. Caughey. A hybrid algorithm for the joint PDF equation of turbulent reactive flows. *Journal of Computational Physics*, **166**: 218 –252, 2001.

[188] H. W. Ge. *Probability density function modeling of turbulent non-reactive and reactive spray flows*. PhD thesis. Ruprecht-Karls-Universität, 2008.

[189] M. Schäfer. *Numerik im Maschinenbau*. ISBN 3-540-65391-0, Springer Verlag Berlin, 1999.

[190] S. De and S. H. Kim. Large eddy simulation of dilute reacting sprays: Droplet evaporation and scalar mixing. *Combustion and Flame*, **160**: 2048 –2066, 2013.

[191] F. Mayinger and O. Feldmann. *Optical Measurements: Techniques and Applications*. Springer Berlin Heidelberg, 2001.

[192] M. Sommerfeld and H.-H. Qiu. Experimental studies of spray evaporation in turbulent flow. *International Journal of Heat and Fluid Flow*, **19**: 10 –22, 1998.

[193] R. J. Sornek, R. Dobashi, and T. Hirano. Effect of turbulence on vaporization, mixing, and combustion of liquid-fuel sprays. *Combustion and Flame*, **120**: 479 –491, 2000.

[194] A. J. Yule and P. R. Ereaut and A. Ungut. Droplet sizes and velocities in vaporizing sprays. *Combustion and Flame*, **54**: 15 –22, 1983.

[195] X.-Q. Chen and J. C. Pereira. Prediction of evaporating spray in anisotropically turbulent gas flow. *Numerical Heat Transfer, Part A: Applications*, **27**: 143–162, 1995.

[196] S. De, K. Lakshmisha, and R. W. Bilger. Modeling of nonreacting and reacting turbulent spray jets using a fully stochastic separated flow approach. *Combustion and Flame*, **158**: 1992 –2008, 2011.

[197] Y. Hu and E. Gutheil. Joint gas velocity-mixture fraction probability density function modeling of turbulent methanol spray flows. *Proceedings of 25th European Conference on Liquid Atomization and Spray Systems*, Chania, Greece, 1–4 September, 2013.

[198] V. G. McDonell and G. S. Samuelsen. An experimental data base for the computational fluid dynamics of reacting and nonreacting methanol sprays. *Journal of Fluids Engineering*, **117**: 145 –153, 1995.

[199] C. Chevalier. *Entwicklung eines detallierten Reaktionmechanismus zur Modellierung der Verbrennungsprozesse von Kohlenwasserstoffen bei Hoch- und -Niedertemperaturbedingungen*. PhD thesis. Universität Stuttgart.

[200] E. Gutheil. Structure and extinction of laminar ethanol-air spray flames. *Combustion Theory and Modelling*, **5**: 131–145, 2001.

[201] H. Olguin. *Theoretical and Numerical Analysis of Laminar Spray Flames for Use in Turbulent Spray Combustion Modeling*. PhD Thesis. Heidelberg University, 2015.

[202] M. S. Raju. On the importance of chemistry/turbulence interactions in spray computations. *Numerical Heat Transfer, Part B: Fundamentals*, **41**: 409–432, 2002.

[203] X.-Q. Chen and J. C. Pereira. Prediction of evaporating spray in anisotropically turbulent gas flow. *Numerical Heat Transfer, Part A: Applications*, **27**: 143–162, 1995.

[204] M. Juddoo, A. R. Masri, and S. B. Pope. Turbulent piloted partially-premixed flames with varying levels of O2/N2: stability limits and PDF calculations. *Combustion Theory and Modelling*, **15**: 773–793, 2011.

Eidesstattliche Versicherung gemäß § 8 der Promotionsordnung der Naturwissenschaftlich-Mathematischen Gesamtfakultät der Universität Heidelberg

1. Bei der eingereichten Dissertation zu dem Thema

_____

_____

_____

handelt es sich um meine eigenständig erbrachte Leistung.

2. Ich habe nur die angegebenen Quellen und Hilfsmittel benutzt und mich keiner unzulässigen Hilfe Dritter bedient. Insbesondere habe ich wörtlich oder sinngemäß aus anderen Werken übernommene Inhalte als solche kenntlich gemacht.

3. Die Arbeit oder Teile davon habe ich wie folgt/bislang nicht[1)] an einer Hochschule des In- oder Auslands als Bestandteil einer Prüfungs- oder Qualifikationsleistung vorgelegt.

Titel der Arbeit:_____

_____

Hochschule und Jahr:_____

Art der Prüfungs- oder Qualifikationsleistung:_____

4. Die Richtigkeit der vorstehenden Erklärungen bestätige ich.

5. Die Bedeutung der eidesstattlichen Versicherung und die strafrechtlichen Folgen einer unrichtigen oder unvollständigen eidesstattlichen Versicherung sind mir bekannt.

Ich versichere an Eides statt, dass ich nach bestem Wissen die reine Wahrheit erklärt und nichts verschwiegen habe.

_____ _____

Ort und Datum Unterschrift

[1)] Nicht Zutreffendes streichen. Bei Bejahung sind anzugeben: der Titel der andernorts vorgelegten Arbeit, die Hochschule, das Jahr der Vorlage und die Art der Prüfungs- oder Qualifikationsleistung.